PHYSICAL REVIEW B VOLUME 36, NUMBER 4 1 AUGUST 1987

Self-consistent large-*N* expansion for normal-state properties of dilute magnetic alloys

N. E. Bickers,* D. L. Cox,† and J. W. Wilkins
Laboratory of Atomic and Solid State Physics, Cornell University, Ithaca, New York 14853-2501

(Received 30 September 1986)

Finite-temperature properties of the infinite-U Anderson model for rare-earth alloys are calculated within a unified approach. The impurity-electron density of states and magnetic moment spectrum provide a natural framework for describing both static and dynamic properties. The density of states and moment spectrum exhibit low-energy "Kondo resonances" with approximate single-parameter scaling, which persists for impurity valences in the range 1.0–0.7. The position of the resonance in the zero-temperature density of states, T_0, sets the scale for all low-temperature properties. Results are reported for the impurity valence, resistivity, thermopower, thermal conductivity, magnetic susceptibility, specific heat, photoemission and inverse-photoemission spectra, and neutron scattering linewidth. The effect of spin-orbit interactions is incorporated in the theory. The calculation is a diagrammatic approximation motivated by the simplifying concept of large angular momentum degeneracy (N). The approximate solution is thermodynamically consistent and satisfies all pertinent sum rules. Static properties (magnetic susceptibility and specific heat) are in good agreement with exact results of the Bethe *ansatz*. Experimental results on both dilute and concentrated Ce alloys are described quantitatively with use of a one-parameter (T_0) theory.

I. INTRODUCTION

The richly varied properties of electrons in metals reflect the presence of an enormous number of interacting degrees of freedom. Despite this complexity, only a small number of qualitatively different electronic ground states are realized in nature. Principal among these are the normal Fermi-liquid, magnetically ordered, and superconducting states. A key to the understanding of new materials is the experimental determination of the ground state and the development of a model which accounts for it. In this regard, magnetic alloys, i.e., metals containing a random or ordered array of magnetic ions, have presented a particularly subtle and challenging problem.

Ions which exhibit a well-defined magnetic moment in isolation might be expected to produce magnetic ground states when embedded in a metal. Specifically, the Curie law susceptibility [$\chi(T)=C/T$, with C a constant] of isolated paramagnetic ions might be expected to persist in the metallic state. In general, this is not the case. A large class of dilute transition metal and lanthanide alloys, including *Cu*Fe, *Cu*Mn, *La*Ce, and *Au*Yb exhibit Pauli law susceptibilities [$\chi(T)=\text{const}$] at low temperature, indicating a nonmagnetic Fermi liquid ground state.[1] [This identification does not depend on susceptibility measurements alone, but is confirmed by other static (specific heat) and dynamic properties.] The formation of such a ground state is commonly referred to as the Kondo effect, in honor of one of the first theorists to contribute to its understanding;[2] by extension, the Kondo effect refers to any anomalous property resulting from the nonmagnetic ground state. The understanding of this effect has occupied a large number of condensed matter theorists over a period of more than twenty years.

A source of exceptional current interest is the recent discovery of anomalous nonmagnetic ground states in concentrated systems as well.[3] A criterion due to Hill states that when the separation of neighboring lanthanide ions in a compound is larger than 3.25–3.50 Å, a magnetically ordered ground state results. In this limit, the 4*f* electrons responsible for magnetism remain localized. A number of concentrated alloys, including $CeAl_3$ and $CeCu_6$, satisfy the Hill criterion but nevertheless possess Fermi liquid ground states. Furthermore, a related series of compounds, including $CeCu_2Si_2$, exhibit superconducting rather than magnetic ground states. These compounds are jointly known as "heavy electron" metals. The effective electronic mass derived from the low-temperature specific heat and susceptibility in these systems is hundreds of times larger than the free-electron mass.

While a detailed understanding of such concentrated systems is not yet available, a quantitative picture of the properties of dilute magnetic alloys has begun to emerge in recent years. A number of theoretical techniques have contributed to this progress. The numerical renormalization group[4,5] and Bethe-*ansatz* diagonalization[6,7] methods have provided essentially exact solutions for all equilibrium properties. In this paper, we present results based on a third approach, the "self-consistent large-degeneracy expansion."[8,9] [The method's name refers to the level degeneracy of the electrons responsible for magnetism in isolated ions (the 4*f* electrons in the lanthanide series).] Equilibrium properties calculated within this approximation are in excellent agreement with results of the preceding "exact" methods. In addition, the large-degeneracy expansion provides results for dynamic properties which cannot be computed by the renormalization group or Bethe *ansatz*. In this sense, the large-degeneracy expansion provides a more unified quantitative description of magnetic alloy physics than any previous approach.

The remainder of the paper is organized as follows: in

Sec. II, we attempt to place the present work in context by briefly reviewing previous approaches to the Kondo effect and discussing the basis for the large-degeneracy expansion. In Sec. III, we present an overview of our results, stressing the simplifying features of the physics. Calculational details are discussed at length in Secs. IV and V. In Sec. VI, we compare our results for various properties with the available experiments. Finally, we discuss future directions for this work and summarize our findings in Sec. VII.

II. REVIEW

Interest in dilute magnetic alloys may be traced back to the earliest days of metals physics, when a low-temperature resistivity minimum was observed in noble metal samples containing small amounts of transition metal impurities[10] (see Fig. 1). Such a resistivity minimum cannot be understood in terms of conventional phonon and nonmagnetic impurity scattering. Experimental interest in transition-metal alloys increased in the late 1950s and early 1960s, but no successful theory was advanced to account for their anomalous behavior. In 1964, Kondo demonstrated that the source of the resistivity minimum was magnetic impurity scattering.[2] While the phonon contribution to the resistivity decreases with temperature, the magnetic contribution increases. In Kondo's perturbative calculation, the resistivity actually diverges logarithmically for $T \rightarrow 0$.

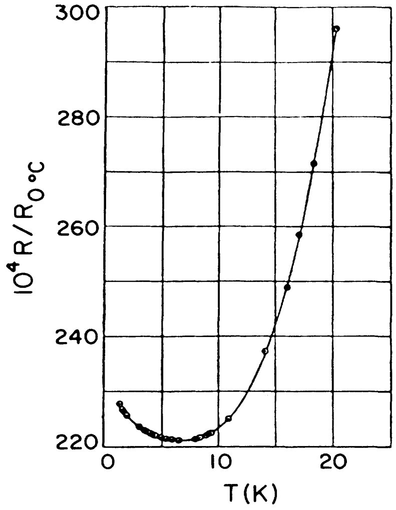

FIG. 1. Resistivity minimum in a noble metal (Au) with residual transition metal impurities, reproduced from the work of W. J. de Haas and G. J. van den Berg, Physica **3**, 440 (1936). The curve shows the resistance of a Au wire, normalized by the value at 0° C. This represents one of the earliest observations of anomalous low-temperature effects in a dilute magnetic alloy. A number of excellent review articles discuss experiments on magnetic alloys from the 1930s through recent years (Ref. 1).

Kondo investigated the so-called antiferromagnetic s-d exchange Hamiltonian,

$$H = \sum_{\mathbf{k},\sigma} \varepsilon_k n_{\mathbf{k}\sigma} - 2J\mathbf{S}\cdot\mathbf{s}(0) \ . \tag{2.1}$$

Here, J is a negative exchange constant, $\mathbf{S}$ is the impurity spin and $\mathbf{s}(0)$ is the conduction-electron spin density at the impurity. This Hamiltonian is now conventionally known as the "Kondo Hamiltonian."

An alternate model for magnetic alloys was developed in 1961 by Anderson.[11] The simplest version of the Anderson Hamiltonian may be written

$$\begin{aligned} H_A &= H_{\text{band}} + H_{\text{imp}} + H_{\text{mix}} \ , \\ H_{\text{band}} &= \sum_{\mathbf{k},\sigma} \varepsilon_k n_{\mathbf{k}\sigma} \ , \\ H_{\text{imp}} &= \varepsilon_d \sum_{\sigma} n_\sigma + U_{n_\uparrow n_\downarrow} \ , \\ H_{\text{mix}} &= V \sum_{\mathbf{k},\sigma} (c^\dagger_{\mathbf{k}\sigma} d_\sigma + \text{H.c.}) \ . \end{aligned} \tag{2.2}$$

The three components of the Hamiltonian describe conduction electrons, impurity electrons and a hybridization, or mixing interaction, between the two. Creation operators are denoted $c^\dagger_{\mathbf{k}\sigma}$ (conduction) and $d^\dagger_\sigma$ (impurity), with $n_{\mathbf{k}\sigma} = c^\dagger_{\mathbf{k}\sigma} c_{\mathbf{k}\sigma}$ and $n_\sigma = d^\dagger_\sigma d_\sigma$. The key features of the model are (a) strong Coulomb correlation between the localized electrons ($U > 0$) and (b) hybridization between localized and delocalized electrons (V). A measure of the strength of hybirdization is the "hybridization width" $\Gamma = \pi N(0) V^2$, with $N(0)$ the single-spin density of conduction states. Note that the only degeneracy in the impurity Hamiltonian is due to spin. More elaborate versions of the model incorporate an additional orbital index (appropriate for describing $3d$ and $4d$ transition metals) or a total angular momentum index (appropriate for systems with strong spin-orbit coupling, like the lanthanides). The Anderson model is more fundamental than the Kondo model, which may be derived from it by a canonical transformation[12] in the limit $\varepsilon_d \rightarrow -\infty$, $V \rightarrow \infty$, $U \rightarrow \infty$, $V^2/\varepsilon_d = J$.

The discovery of unexpected divergences in perturbation theory for the Kondo and Anderson models led to greatly increased theoretical interest in magnetic alloys.[13] During the 1960s, interest centered on the general scattering properties of magnetic impurities. Suhl's dispersion theory[14] provided the first resistivity calculation satisfying unitarity bounds. An essentially equivalent approach is the Green's function decoupling scheme developed by Nagaoka[15] and first solved by Hamann and Bloomfield;[16] this method yields excellent results at high temperature, but breaks down below a characteristic scale

$$T_K^0 = De^{-1/2N(0)|J|} \ , \tag{2.3}$$

with D and J the band half-width at half maximum and magnetic exchange constant, and $N(0)$ the single-spin density of states at the Fermi surface. (We hesitate to call T_K^0 the "Kondo temperature," since this phrase has special connotations in modern usage. See, e.g., Ref. 4.) For example, the low-temperature resistivity in Suhl-Nagaoka theory[16] takes the form

$$\rho(T) = \tfrac{1}{2}\rho(0) \left[1 - \frac{\ln(T/T_K^0)}{[\ln^2(T/T_K^0) + \pi^2 S(S+1)]^{1/2}} \right] , \tag{2.4}$$

with $\rho(0)$ the s-wave unitarity bound resistivity. The nonanalytic saturation for $T \to 0$ is an unphysical consequence of the approximation scheme. The specific heat C also has unphysical features[17] within the Suhl-Nagaoka scheme: C tends to zero for $T \to 0$ as $\ln^{-4}(T/T_K^0)$, and the high-temperature entropy is

$$S(T\to\infty)-S(0)=(2S+2)\ln(2S+2)+2S\ln(2S) -2(2S+1)\ln(2S+1)\ . \tag{2.5a}$$

This contradicts a general theorem of Mattis,[18] which (correctly) predicts

$$S(T\to\infty)-S(0)=\ln(2S+1)-\ln(2S)\ . \tag{2.5b}$$

Finally, results for the susceptibility within the Suhl-Nagaoka scheme are inconclusive: depending on the approximation adopted, the method yields complete, incomplete or overcomplete screening of a spin-$\frac{1}{2}$ impurity moment.[19]

Other early approaches to the Kondo Hamiltonian lead to different descriptions of the ground state. In particular, Yosida and his collaborators[20] developed a variational theory based on a singlet bound state of the conduction electrons and the impurity spin. A Gor'kov-type mean-field theory with many of the same features was employed by Takano and Ogawa.[21] (The theory of Takano and Ogawa is similar to more recent mean-field treatments of magnetic alloys and heavy-electron metals.) These methods correctly predicted a nonmagnetic ground state for the Kondo Hamiltonian, with a Pauli-type susceptibility at low temperature.

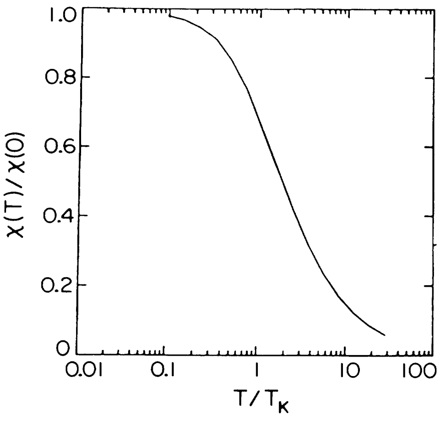

FIG. 2. Results of Wilson's numerical renormalization group for the Kondo model susceptibility. Note the temperature scale is logarithmic. At high temperatures, the susceptibility is Curie-like; as T decreases below a characteristic scale T_K, the nonmagnetic ground state of the model begins to strongly influence χ (and other properties). The susceptibility saturates to a finite value inversely proportional to T_K.

The nature of the ground state was not convincingly established until the early 1970s. Renormalization group approaches to the magnetic alloy problem were introduced by Anderson, Yuval, and Hamann[22] and by Wilson.[4] The scaling approach by the first authors showed that for an arbitrarily weak antiferromagnetic exchange coupling J, the system's ground state is a nonmagnetic singlet. Moreover, on arbitrary energy and temperature scales, the system may be described by an effective exchange constant J_{eff}. For $T \to 0$, J_{eff} diverges, and the system behaves as though the impurity were coupled rigidly to the conduction electrons from the start; at high temperatures, the effective exchange constant tends to its "bare" value J, and the system may be described by perturbation theory (with its characteristic $\ln T$ corrections). The renormalization group concepts introduced by Anderson, Yuval, and Hamann were fully developed by Wilson. Wilson's combined numerical and analytical approach led to the first quantitatively accurate calculation of a Kondo model property,[4] the magnetic susceptibility $\chi(T)$ (see Fig. 2). Wilson rigorously established that the temperature-dependent effective moment

$$\mu_{\text{eff}}^2(T)=3T\chi(T) \tag{2.6}$$

vanishes for $T \to 0$, and that the moment obeys a simple scaling relation

$$\mu_{\text{eff}}^2(T)=F(T/T_K)\ , \tag{2.7}$$

with F a universal function. The Kondo temperature T_K is defined using the high-temperature series expansion for μ_{eff}^2 in powers of $\ln^{-1}(T/T_K)$: T_K is chosen such that the coefficient of $\ln^{-2}(T/T_K)$ in this series is identically zero. For a flat band density of states, it may be shown that[23]

$$T_K=\frac{D}{2\pi}\exp(\tfrac{3}{4}+C)[2N(0)\,|\,J\,|\,]^{1/2}e^{-1/2N(0)\,|\,J\,|}\ , \tag{2.8}$$

with Euler's constant $C=0.577\,216$. Note the similarity to the temperature scale in Suhl-Nagaoka theory. The crossover from Curie law magnetism with perturbative corrections at high temperatures to Pauli magnetism at low temperatures is graphically illustrated (see Fig. 3) by plotting the effective moment. The vanishing, or "quenching," of this moment at low temperatures signals a nonmagnetic ground state. (The specific heat of the

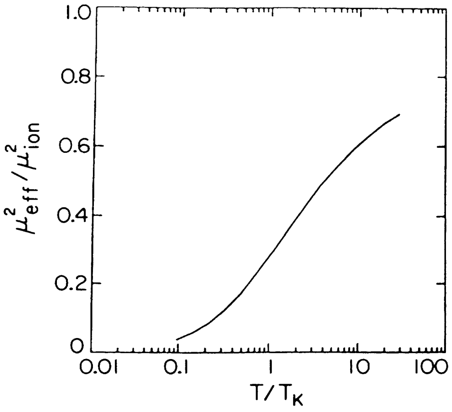

FIG. 3. Results of Wilson's renormalization group for the effective moment in the Kondo model. The effective magnetic moment $\mu_{\text{eff}}^2=3T\chi(T)$ is scaled by its ionic value $\mu_{\text{ion}}^2=\frac{3}{4}(g\mu_B)^2$. At high temperatures, μ_{eff}^2 approaches the free-ion value with logarithmic corrections; for $T \to 0$, the moment is "quenched away," finally vanishing in the nonmagnetic ground state.

Kondo model was later computed using Wilson's approach.[24] This calculation represents the only application of renormalization-group methods to a magnetic alloy property other than the susceptibility.)

Wilson's renormalization-group approach was later employed in the first quantitative study of the susceptibility of the Anderson model[5] [Eq. (2.2)]. This study established the existence of three distinct parameter regimes (Fig. 4) for systems with large Coulomb repulsion ($U \gg |\varepsilon_d|, \Gamma$): (a) the empty impurity regime $\varepsilon_d \gg \Gamma$; (b) the mixed valent regime ($|\varepsilon_d| \leq \Gamma$); and (c) the Kondo regime ($-\varepsilon_d \gg \Gamma$). In the Kondo regime, the Anderson model susceptibility maps smoothly onto the Kondo model susceptibility with an effective Kondo temperature T_K.

Renormalization-group methods provided the most powerful approach to the magnetic alloy problem before 1980. In this year, a new approach to magnetic impurity models was discovered independently by Andrei[25] and Wiegmann.[26] Using the Bethe-Yang *ansatz*, these authors succeeded in exactly diagonalizing the Kondo Hamiltonian (with a linear band dispersion). Solutions were subsequently found for variations of the Anderson model.[27–29] The finite-temperature thermodynamics of these models may be formulated in terms of the solutions to infinite hierarchies of integral equations. These equations have been solved numerically,[30–33] and the thermodynamics of the Kondo and Anderson models are now well established. For properties studied using both the renormalization group and Bethe *ansatz* (e.g., the finite-temperature susceptibility and specific heat of the Kondo model), the agreement between the two methods is excellent.

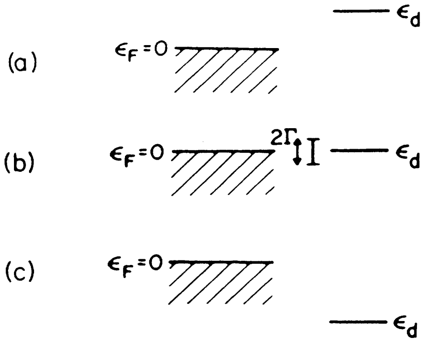

FIG. 4. Parameter regions for the Anderson model with strong local correlations ($U \gg |\epsilon_d|, \Gamma$). The shaded rectangle represents the Fermi sea of conduction electrons filled to energy $\epsilon_F = 0$. The adjacent line represents the impurity orbital. (a) Empty impurity regime. In this regime, the impurity orbital lies far above the Fermi level ($\epsilon_d \gg \Gamma$). The impurity valence is near zero, and the system's behavior is nonmagnetic at all temperatures. (b) Mixed valent regime. In this regime, the impurity orbital lies close to the Fermi level: many-particle states with empty and singly occupied impurity configurations are nearly degenerate. The impurity valence is intermediate between zero and one. The high-temperature effective moment reflects an admixture of impurity configurations, and the charge susceptibility is large (hence, the valence may be changed substantially by applying pressure or by alloying). (c) Kondo regime. In this regime, the impurity orbital lies far below the Fermi level. The impurity valence is close to unity. At high temperatures, the effective moment approaches that of a noninteracting ion; at low temperatures, the magnetic moment is quenched to zero, and the system's properties take on a universal form with scaling temperature T_K.

The principal weakness of the "exact" methods discussed above is their inability to treat dynamic properties, such as the resistivity, thermopower and dynamic susceptibility. (The resistivity at zero temperature may be computed within the Bethe *ansatz* by a phase shift analysis;[34] this approach cannot be generalized to finite temperatures.) In the absence of exact methods, a "high-order" approximation scheme is required. Simple perturbation theory and Green's-function decoupling methods fail at low temperatures, as discussed previously. An alternative approach, based on large magnetic degeneracy, has been suggested by Anderson[35] and Ramakrishnan.[36] Certain problems in quantum mechanics, quantum field theory and statistical mechanics which involve N degrees of freedom (colors, spin components, etc.) are known to simplify in the limit $N \rightarrow \infty$; in some cases, systematic expansions in $1/N$ have been derived.[37] In the magnetic impurity problem, the analogous degrees of freedom are the angular momentum channels of the impurity electron. For example, in the absence of spin-orbit and crystalline electric field (CEF) effects, the $4f^1$ configuration of Ce is fourteenfold degenerate; if spin-orbit coupling is taken into account, the ground configuration remains sixfold degenerate. In this case, the inverse degeneracy $1/N$ is an intuitively reasonable expansion parameter.

In this paper, we consider a particular large-degeneracy approximation for the orbitally degenerate Anderson model

$$\begin{aligned} H_A &= H_{\text{band}} + H_f + H_{\text{mix}} , \\ H_{\text{band}} &= \sum_{k,m} \varepsilon_k n_{km} , \\ H_f &= \varepsilon_f \sum_m n_m + U \sum_{(m>m')} n_m n_{m'} , \\ H_{\text{mix}} &= V \sum_{k,m} (c_{km}^\dagger f_m + \text{H.c.}) . \end{aligned} \tag{2.9}$$

It is assumed that conduction-impurity mixing takes place in a single angular momentum sector (lj); conduction states which couple to the impurity are labeled by wave vector $k = |\mathbf{k}|$ and magnetic quantum number $m_j \equiv m$. The band- and impurity-electron creation operators are $c_{km}^\dagger$ and $f_m^\dagger$ (with $n_{km} = c_{km}^\dagger c_{km}$ and $n_m = f_m^\dagger f_m$). This is the appropriate generalization of the Anderson Hamiltonian for systems with strong spin-orbit coupling. In particular, this is a reasonable model for Ce impurities in a metal. For Ce, $l = 3$, $j = \frac{5}{2}$, and the magnetic degeneracy $N = 6$.

Since the Coulomb energy is typically greater than 5 eV in Ce compounds, and the hybridization width $\Gamma = \pi N(0) V^2$ is on the order of 0.1 eV, it is natural to attempt to incorporate the localized correlation effects exactly and to treat the hybridization term perturbatively. For "soft" measurements (low-energy and temperature), the exact value of U should be unimportant. The analysis of H_A is simplified by assuming that $U \rightarrow \infty$; this assumption removes from the problem all states in which the f

occupancy is greater than unity. Within the system's reduced Hilbert space, the Hamiltonian may be rewritten using f-orbital projection operators:

$$\begin{aligned}
H_A^{U=\infty} &= H_{\text{band}} + H_f^{U=\infty} + H_{\text{mix}}^{U=\infty} \ , \\
H_f^{U=\infty} &= \varepsilon_f \sum_m \hat{N}_m \ , \\
H_{\text{mix}}^{U=\infty} &= V \sum_{km} (c_{km}^\dagger F_m + \text{H.c.}) \ ,
\end{aligned} \tag{2.10}$$

with

$$\begin{aligned}
\hat{N}_0 &= |0\rangle\langle 0| \ , \\
\hat{N}_m &= |m\rangle\langle m| \ ,
\end{aligned} \tag{2.11}$$

and

$$F_m = |0\rangle\langle m| \ .$$

Here $|m\rangle$ represents the $4f^1$ configuration with magnetic quantum number m, and $|0\rangle$ represents the $4f^0$ configuration.

The Hamiltonian (2.10) as written contains no factor of $1/N$ with which to organize an expansion. As in other large-N expansions in quantum field theory and statistical mechanics, it is necessary to rescale parameters at the outset. In the present case, the quantity NV^2 must be treated as a constant of $O(1)$, rather than $O(N)$. (Equivalently, the hybridization matrix element may be rescaled by $V \to \tilde{V}/\sqrt{N}$ before proceding.[38]) The approximation employed below is an infinite-order summation in $1/N$ perturbation theory. Specifically, this approximation sums all processes of $O(1)$ and $O(1/N)$, as well as a large class of processes of all higher orders; the lowest-order processes omitted are $O(1/N^2)$. This approximation may be shown to be thermodynamically self-consistent,[39] in the sense of Baym's analysis of the interacting electron gas,[40] and we shall hereafter refer to it as the "self-consistent large degeneracy expansion." The method is known by a number of other names, including the "noncrossing approximation" (NCA).[39] The source of this name is discussed in Sec. IV. The results of this approximation are discussed in the following section; the details of the calculation are postponed to Sec. IV.

III. OVERVIEW OF RESULTS

Before discussing the details of our calculations, we present an overview of the results. This section may be of greatest interest to the casual reader. In general, the behavior of both static and dynamic properties may be understood in terms of two temperature-dependent dynamical spectra of the electronic system. These spectra are $\rho_f(\omega)$, the many-body spectral density for adding (or removing) an f electron of energy ω, and $\sigma_f(\omega)$, the spectrum for f moment fluctuations of energy ω. For simplicity, these spectra are referred to as the f density of states and the f moment spectrum throughout the remainder of this paper. Both spectra are in principle experimentally measurable: ρ_f may be obtained from f photoemission and inverse photoemission, and σ_f from neutron scattering.

Formally, the two spectra are the Fourier transforms of time-dependent correlation functions:

$$\begin{aligned}
\rho_f(\omega) &= -\frac{1}{\pi}\text{Im}\int_{-\infty}^{\infty} dt\, e^{i(\omega+i0^+)t} G_f(t) \ , \\
\sigma_f(\omega) &= -\frac{1}{\pi}\text{Im}\int_{-\infty}^{\infty} dt\, e^{i(\omega+i0^+)t} M_f(t) \ ,
\end{aligned}$$

with

$$\begin{aligned}
G_f(t) &= -i\Theta(t)\langle \{F_m(t), F_m^\dagger(0)\}\rangle \ , \\
M_f(t) &= -i\Theta(t)\langle [\hat{M}(t), \hat{M}(0)]\rangle \ , \\
\hat{M} &\equiv g\mu_B \sum_m m\hat{N}_m \ .
\end{aligned} \tag{3.1}$$

The correlation function $G_f(t)$ is just the amplitude for propagating an f electron (or hole) for time t; the function $M_f(t)$ measures the self-correlation of the local moment over time t. The first correlation function has Fermi character, and the second Bose character. It is easy to show (see Appendix B) that the spectral densities for these correlation functions satisfy sum rules:

$$\begin{aligned}
&\int_{-\infty}^{\infty} d\omega\, f(\omega)\rho_f(\omega) = \langle \hat{N}_m \rangle = \frac{1}{N} n_f(T) \\
&\int_{-\infty}^{\infty} d\omega\, b(\omega)\sigma_f(\omega) = (g\mu_B)^2 \sum_m m^2 \langle \hat{N}_m \rangle = \frac{\mu_j^2}{3} n_f(T) \ ,
\end{aligned} \tag{3.2}$$

where f and b are the Fermi and Bose distribution functions

$$\begin{aligned}
f(\omega) &= \frac{1}{e^{\beta\omega}+1} \ , \\
b(\omega) &= \frac{1}{e^{\beta\omega}-1} \ ;
\end{aligned} \tag{3.3a}$$

$n_f(T) \le 1$ is the mean occupancy of the f orbital at temperature T; and

$$\mu_j^2 \equiv j(j+1)(g\mu_B)^2 \ . \tag{3.3b}$$

These sum rules specify the overall normalization for various processes: the total weight for removing an f electron with quantum number m from the system is just the m-orbital occupancy; the total weight for moment fluctuations of arbitrary energy is a sum of the moments $(mg\mu_B)^2$ for each orbital, weighted by the occupancy of that orbital.

Both the f density of states and moment spectrum may be computed within the self-consistent large-degeneracy expansion; the sum rules above are satisfied within this approximation (see Appendix B). Plots of ρ_f and σ_f for a typical choice of parameters in the Kondo regime are shown in Figs. 5 and 6. For both plots, the temperature of the system is far below the characteristic Kondo scale. The f density of states shows a two-peaked structure. The weight at negative energies corresponds to electron removal and the weight at positive energies to electron addition. The lower peak appears near the energy of the magnetic f^1 multiplet in the noninteracting system. The peak at positive energy T_0 is a purely many-body effect and has no interpretation based on the noninteracting system. This nonperturbative feature in the density of states is commonly called the Abrikosov-Suhl, or Kondo, resonance.[41] For brevity, we refer to it hereafter as the Kondo resonance. The two peaks shown are not the only features in the physical f density of states for a finite correlation energy U. Additional peaks must appear near ε_f+U, ε_f+2U, and so forth. These peaks measure the weight for adding an electron to the system when the f occupancy is already one or more, i.e., they measure the weight for exciting the system into an f^n configuration with $n \geq 2$. When U is assumed to be infinite, the weight in these processes is pushed out to infinite energy and removed from the calculation. The computed density of states then measures only the weight for removing an electron from the f^1 configuration (negative energies) and for adding an electron to the f^0 configuration (positive energies). For U extremely large, but finite, the ground state contains negligible admixtures of f^n, $n \geq 2$, and the only feature missing from the computed spectrum at zero temperature is the peak near ε_f+U for exciting the $f^1 \to f^2$ transition.

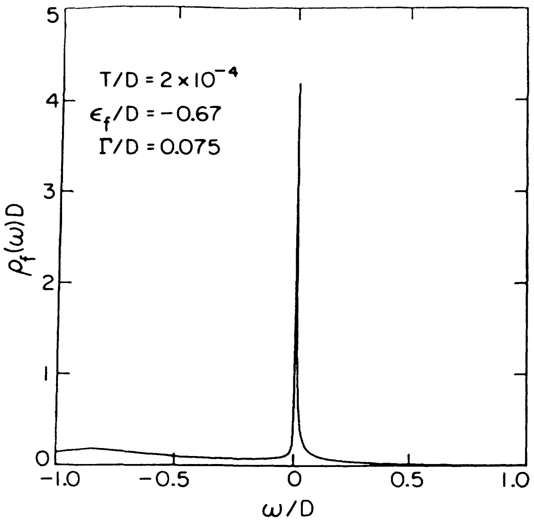

FIG. 5. f density of states ρ_f in the low-temperature limit. The conduction electron density of states has been assumed to have a Lorentzian profile with half-width D; in most Ce alloys, a reasonable value for D is 3 eV. In units of D, the values chosen for the f-orbital energy ϵ_f and hybridization width Γ are -0.67 and 0.075. The orbital degeneracy N is 6, the appropriate value for the spin-orbit ground state of the Ce ion (with negligible crystalline electric fields). The temperature is $(2\times10^{-4})D$. The density of states has a characteristic two-peaked structure: the lower peak measures the probability for exciting an $f^1 \to f^0$ transition within a single magnetic channel. The total weight for this process is 0.155, close to the value $1/N=\frac{1}{6}$ expected in the absence of hybridization. The lower peak is nearly Lorentzian, with half-width $\sim N\Gamma$ and height $\sim(1/\pi N)(N\Gamma)^{-1}$; it is centered at $\tilde{\epsilon}_f < \epsilon_f$. The upper peak, or Kondo resonance, is a unique feature of magnetic alloys, with no analog in nonmagnetic systems. It measures the probability for exciting an $f^0 \to f^1$ transition. The position of this peak for $T \to 0$, T_0, is *by definition* our low-temperature scale. The Kondo resonance has half-width of order $\pi T_0/N$ and height of order $(\pi\Gamma)^{-1}$; hence, its total weight is $\sim \pi T_0/N\Gamma$.

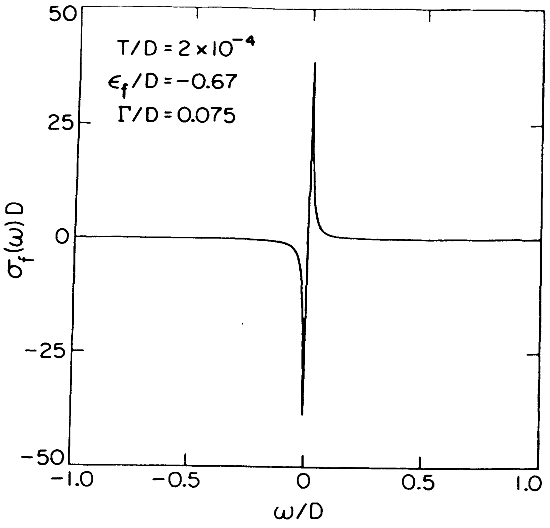

FIG. 6. f moment spectrum σ_f in the low-temperature limit. The parameters are the same as those in Fig. 5. The moment spectrum is odd in frequency. Its principal features are pronounced peaks at energies of $\sim \pm 1.4 T_0$, where T_0 is the low-energy scale deduced from the f density of states. The positive-energy portion of the moment spectrum may be measured directly by quasielastic neutron scattering (the positive portion corresponds to neutron energy loss, and the negative portion to neutron energy gain).

The Kondo resonance has a simple physical origin: at zero temperature, the f density of states for $\omega > 0$ may be formally decomposed as

$$\rho_f(\omega)=\sum_N |\langle N|F_m^\dagger|\psi_0\rangle|^2\delta(\omega+E_0-E_N),\quad \omega>0\,, \tag{3.4}$$

with $|\psi_0\rangle$ the exact ground state of an $\mathcal{N}$-particle system and $|N\rangle$ a complete set of energy eigenstates of an $(\mathcal{N}+1)$-particle system. The Kondo resonance indicates the presence of a narrow cluster of $(\mathcal{N}+1)$-particle states at energy T_0 above the ground state: since the ground state is a singlet with only a small admixture of f^0 weight, these are magnetic states which resemble the ground state of an $(\mathcal{N}+1)$-particle system in the absence of hybridization. By allowing the presence of the f^0 admixture, the system gains energy T_0 from hybridization.

Note that the Kondo resonance is superficially similar to resonances in one-body models. The resemblance of the two phenomena should not be stretched too far, however. In one-body problems, the weight for exciting states in an energy range $\Delta\varepsilon$ is just the product of a temperature-independent density of states and a thermal occupancy factor, i.e., the weight for particle addition at energy ε in range $\Delta\varepsilon$, w, is

$$w=\rho(\varepsilon)[1-f(\varepsilon)]\Delta\varepsilon\,, \tag{3.5}$$

with f the Fermi function. This relationship breaks down in interacting systems: a simple Landau picture based on weakly interacting quasiparticles[42] is possible only at low temperatures; further, even in this limit, the occupancy of a single quasiparticle level is dependent on the occupancy of all other levels. While it may be possible to model various properties of a Kondo system in terms of an effective one-body density of states, the resulting function in general corresponds neither to the spectrum of Landau quasiparticles nor to the temperature-dependent many-body spectrum discussed above. Further, the effective one-body density of states must in general vary depending on the property which is to be described. (This is clear since a single choice of $\rho_{\text{eff}}(\varepsilon)$ always yields a Sommerfeld ratio of 1.)

The f moment spectrum of the interacting system, $\sigma_f(\omega)$, also exhibits nonperturbative resonant structure at low energies. Note that the moment spectrum is an odd function of energy. Peaks appear in σ_f at $\omega \approx \pm 1.4 T_0$. The exact relationship between the zero-temperature peak positions in the moment spectrum and the density of states depends on the magnetic degeneracy.

By the fluctuation-dissipation theorem, the moment spectrum is simply related to the absorptive part of the dynamic magnetic susceptibility, i.e.,

$$\operatorname{Im}\chi(\omega + i0^+) = \pi \sigma_f(\omega) . \tag{3.6}$$

Hence, peaks in the moment spectrum occur in regions within which the system may readily exchange energy with a time-dependent magnetic field. The resonances at $\pm 1.4 T_0$ indicate the possibility for magnetic transitions between the singlet ground state and low-lying magnetic levels.

As noted previously, both ρ_f and σ_f are strongly temperature-dependent. This dependence is illustrated in Figs. 7 and 8. The resonances diminish in height and broaden with increasing temperature. Furthermore, the resonances are not, in general, well described by simple one-body models. Figure 9 compares the Kondo resonance in ρ_f with a Lorentzian fit. (A temperature-independent Lorentzian density of states follows from one-body hybridization models.[43]) The computed resonance lies well above the Lorentzian on the high-energy side. Figure 10 compares the computed quantity σ_f with a quasielastic "Lorentzian" spectrum; the computed curves are normalized so that each has peak position and height unity. As in Fig. 9, the Lorentzian fit is quite poor at low temperatures: this is natural since two closely spaced inelastic peaks appear in σ_f/ω, rather than one broad quasielastic peak. Only at high temperatures does the Lorentzian fit become adequate. In this regime, the inelastic peaks are smeared into a single feature. This result may have important consequences for the analysis of neutron scattering in dilute (and concentrated) Kondo systems.

To this point, results have been presented for a single choice of the Kondo scale. If it were necessary to recompute spectra (and other properties) for each new choice of this scale, the picture presented would be quite complicated. Fortunately, this is not the case. Instead the spectra obey approximate single-parameter scaling laws, which hold to high accuracy at low energies and temperatures.

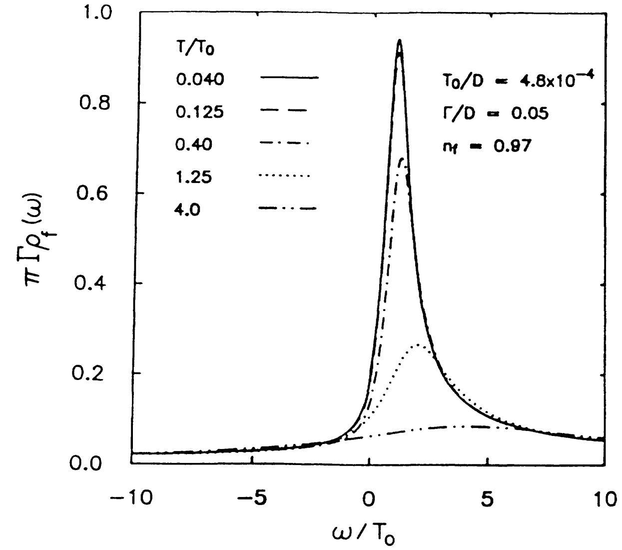

FIG. 7. Temperature dependence of the f density of states. The density of states is normalized by $\pi\Gamma$. [This normalization is convenient since the resonance height for $T \to 0$ approaches $(\pi\Gamma)^{-1}$.] The Kondo scale is in this case 2000 times smaller than the band half-width and 100 times smaller than the hybridization width; as in Fig. 5, $\epsilon_f/D = -0.67$. The resonance diminishes in height and broadens as the temperature is raised through T_0, but remains visible for $T/T_0 > 10$. Physically, the resonance melts away as low-lying many-particle states with magnetic character become thermally populated: the unique signature of $f^0 \to f^1$ transitions from the ground state is smeared out by the presence of "continuum-to-continuum" transitions.

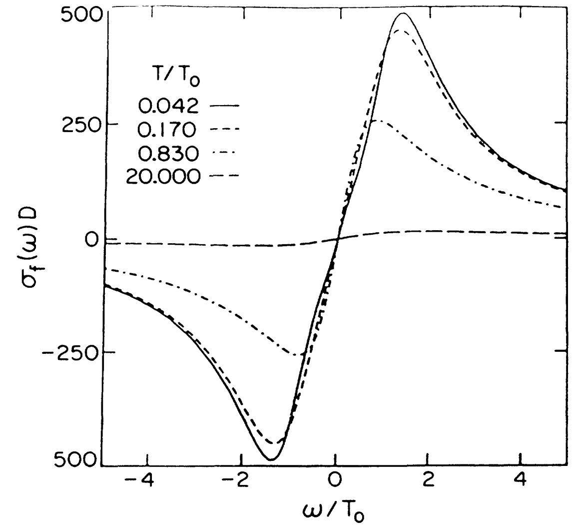

FIG. 8. Temperature dependence of the f moment spectrum. The moment spectrum also diminishes in height as the temperature is raised through T_0.

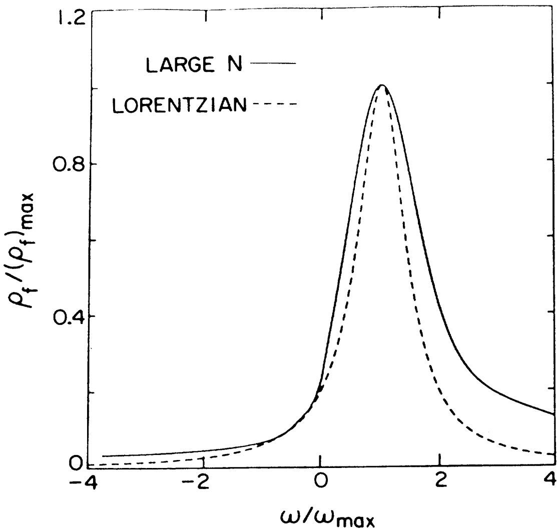

FIG. 9. Comparison of the f density of states with a Lorentzian fit. The spectrum illustrated corresponds to $T_0/D=4.8\times10^{-4}$, with $\Gamma/D=0.05$, $\epsilon_f/D=-0.67$, and $N=6$. Results are shown for the zero-temperature limit. The Lorentzian has been chosen to match the peak value and the value at $\omega=0$. The calculated density of states falls well above the Lorentzian fit for $\omega>T_0$.

Such scaling is to be expected in systems with a single scale for low-energy excitations. In Kondo systems, this scale is the splitting of the singlet ground state and the magnetic configuration. Specifically, the approximate scaling laws are

$$\begin{aligned}&\Gamma\rho_f(\omega;T)=\tilde\rho_f(\tilde\omega;\tilde T)\\&\sigma_f(\omega;T)/\chi(T=0)=\tilde\sigma_f(\tilde\omega;\tilde T)\ \text{ for } |\tilde\omega|,\tilde T\ll1\ ,\end{aligned}\tag{3.7a}$$

where

$$\begin{aligned}&\tilde\omega=\omega/T_0\ ,\\&\tilde T=T/T_0\ ,\end{aligned}\tag{3.7b}$$

with T_0 the position of the resonance in the f density of states at zero temperature. It is trivially possible to redefine the scaling temperature as a fixed multiple of T_0, if $\tilde\rho_f$ and $\tilde\sigma_f$ are also suitably redefined. Note that the scaling functions depend strongly on the f magnetic degeneracy N.

Scaling is not exact, since all properties depend weakly on the mean occupancy, or valence, of the f orbital. For cases in which the valence is near zero, the impurity is nonmagnetic in character and no scaling laws are expected; however, when the valence is near unity, the impurity is magnetic at high temperatures, undergoes a low-temperature Kondo effect and obeys approximate scaling. Numerically, scaling holds in the valence range 1.0–0.7. The extent to which ρ_f and σ_f obey scaling over this range is illustrated in Figs. 11 and 12. Parameter values are summarized in Table I. For both spectra, deviations from scaling are evident only at energies above the characteristic scale T_0.

Since the density of states and moment spectrum obey scaling laws, a wide variety of properties derived from them also assume universal forms in the valence range 1.0–0.7. We briefly survey properties calculated by the large-degeneracy expansion below and postpone detailed derivations and discussion to Secs. IV and V.

The impurity valence $n_f(T)$ is derived from the density of states ρ_f by a direct generalization of the relation for a noninteracting system, i.e.,

$$n_f(T)=N\int_{-\infty}^{\infty}d\varepsilon\, f(\varepsilon)\rho_f(\varepsilon)\ .\tag{3.8}$$

Results for the valence are plotted in Fig. 13. The parameter sets included are those in Table I. The valence is weakly temperature-dependent, provided the f^1 and f^0 configurations are widely separated in energy, i.e., $|\varepsilon_f|\gg N\Gamma$. In this case, the ground-state singlet contains predominantly f^1 contributions, with only a small admixture of f^0 weight: the zero-temperature valence is consequently close to unity. Furthermore, $n_f(T)$ rises with increasing temperature as low-lying excited states

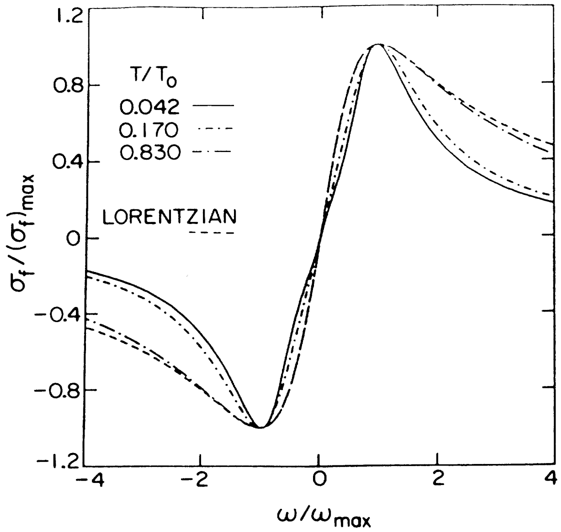

FIG. 10. Comparison of the f moment spectrum with a Lorentzian fit. The parameters are the same as those in Fig. 9. A line shape conventionally used in fitting quasielastic neutron spectra is

$$\frac{\sigma_f(\omega)}{\chi(T)}=\omega\frac{\Gamma_Q(T)/\pi}{\omega^2+\Gamma_Q^2(T)}\ ,$$

where Γ_Q is a temperature-dependent quasielastic linewidth. The shape of the calculated moment spectrum is compared with this standard form in the figure: for each temperature, the position $\omega_{\max}$ and height $(\sigma_f)_{\max}$ of the peak set the scales for the energy and spectral weight. For the standard line shape, $\omega_{\max}=\Gamma_Q$ and $(\sigma_f)_{\max}=\chi(T)/2\pi$. The standard line shape describes the spectrum poorly at low temperatures: this is not surprising since the true spectrum describes transitions between the ground state and a cluster of excited magnetic states at energy $\sim T_0$. At high temperatures, the quasielastic line shape is a good approximation: the linewidth reflects the lifetime broadening of a weakly interacting f moment.

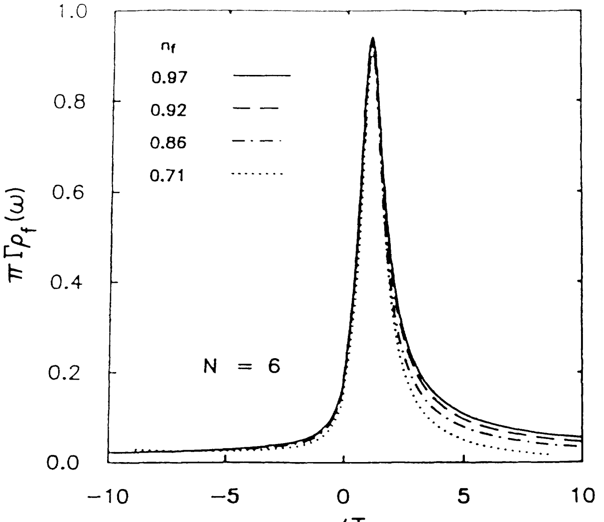

FIG. 11. Scaling of the f density of states for $T \rightarrow 0$. Parameter choices are summarized in Table I. The low-energy scale varies by a factor of more than two-hundred for the curves shown above. A dimensionless density of states is obtained by scaling with $\pi\Gamma$. The four curves exhibit significant deviations from scaling only for $\omega > 2T_0$.

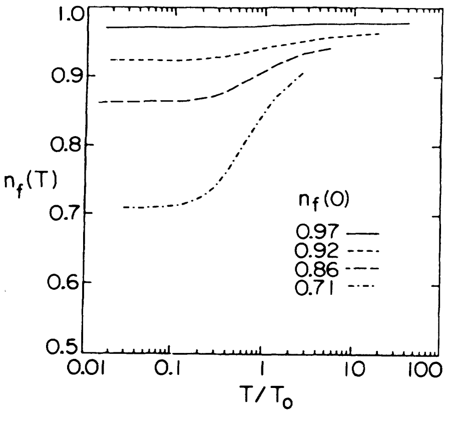

FIG. 13. Temperature variation of the f valence n_f. Parameters are summarized in Table I. The zero-temperature valence varies from 0.97 to 0.71.

with predominantly f^1 character become thermally populated. This population of excited states has characteristic energy T_0; hence, the temperature-dependent part of the valence is expected to obey an approximate scaling relation with reduced temperature T/T_0. Approximate scaling is expected to persist until thermal occupation of high-lying states with significant f^0 weights sets in. In the ultra-high-temperature limit, the valence must just approach $N/(N+1)$, the fraction of local configurations with f^1 character.

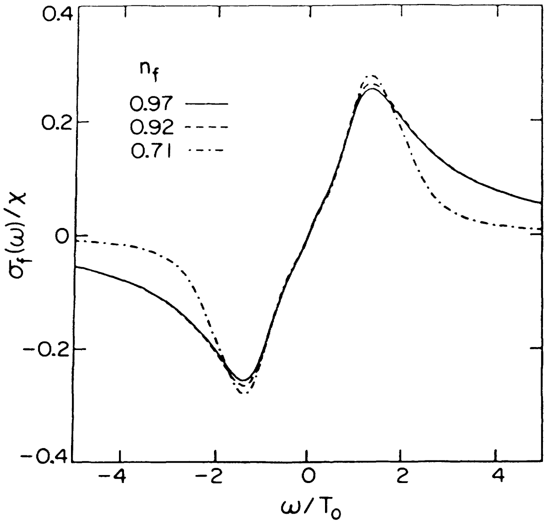

FIG. 12. Scaling of the f moment spectrum for $T \rightarrow 0$. Parameters are summarized in Table I. The spectrum is normalized by $\chi(T=0)$. For $\omega < 2T_0$, the moment spectrum shows no significant deviations from scaling.

The scaling properties of the low-temperature valence may be exhibited explicitly by subtracting off the value of n_f for temperatures *high* in comparison with T_0, but *low* in comparison with $|\varepsilon_f|$, the scale for high-energy f charge excitations. The low-temperature valence may be written

$$n_f(T) \equiv \tilde{n}_f - \Delta n_f(T) , \qquad (3.9)$$

with $\tilde{n}_f$ the intermediate-temperature limit. To estimate $\tilde{n}_f$, we assume that the total decrease in valence due to the Kondo effect is

$$\Delta n_f(0) = \left[1 + \frac{N\Gamma}{\pi T_0} \right]^{-1} . \qquad (3.10)$$

[Compare the lowest-order estimate for this quantity in Eq. (4.17c).] As indicated in Fig. 14, the quantity $\Delta n_f(T)/\Delta n_f(0)$ scales quite well with T/T_0, and becomes vanishingly small for temperatures of order $10T_0$.

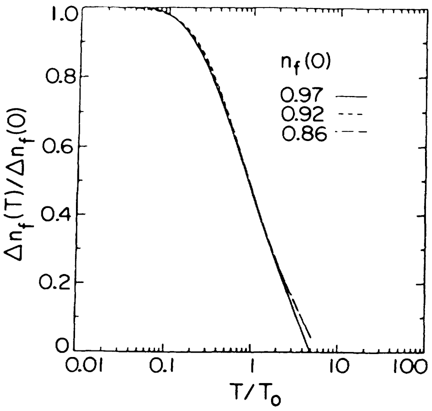

FIG. 14. Scaling of the temperature-dependent contribution to the low-temperature f valence, $\Delta n_f(T)/\Delta n_f(0)$.

TABLE I. Parameters for normal-state calculations. The parameters used in calculating normal-state properties for a model magnetic alloy are listed below. The magnetic ion has an f^1 ground state with degeneracy $N=6$ and an f^0 excited state: $E(f^1)-E(f^0)=\epsilon_f<0$. (This choice is appropriate for the spin-orbit ground state of the Ce ion.) Energies are measured from the Fermi level for the system with an f^0 configuration. The conduction band is centered on the Fermi level and has a Lorentzian profile with half-width D. (A half-width of 3 eV is reasonable for most Ce alloys.) The hybridization width for impurity-conduction electron mixing is Γ. An excited spin-orbit multiplet with degeneracy 8 is included in parameter sets 6 and 7; $\Delta_{\text{s.o.}}$ is the spin-orbit splitting. Parameter sets 8 and 9 do not represent Ce alloys: set 8 is a repetition of a study by Zhang and Lee (Ref. 44), and set 9 tests the effect of increasing degeneracy. The Kondo scale T_0 is defined to be the position of the Fermi surface resonance in the f density of states for $T\to 0$. For the cases studied, T_0 may be estimated within a factor of order unity by the expression

$$T_0 \sim D g^{1/6} e^{-1/6g}\left[\frac{D}{\Delta_{\text{s.o.}}+T_0}\right]^{8/6},\quad g=\frac{\Gamma}{\pi\,|\epsilon_f|}\ .$$

The enhancement factor in the first equation is only present for the spin-orbit parameter sets (6 and 7).

Parameter set	N	ϵ_f/D	Γ/D	$\Delta_{\text{s.o.}}/D$	T_0/D	$n_f(0)$
1	6	-0.67	0.05		4.8×10^{-4}	0.97
2	6	-0.67	0.06		1.6×10^{-3}	
3	6	-0.67	0.075		5.3×10^{-3}	0.92
4	6	-0.67	0.10		1.8×10^{-2}	0.87
5	6	-0.67	0.20		1.1×10^{-1}	0.71
6	$6+8$	-0.67	0.035	0.07	8.7×10^{-4}	0.96
7	$6+8$	-0.67	0.05	0.07	1.5×10^{-2}	0.86
8	6	-0.15	0.016		2.8×10^{-3}	0.85
9	18	-0.67	0.025		7.3×10^{-3}	

The f density of states is also directly related to transport properties in the impurity system. This is because conduction electrons scatter by hopping in and out of the f impurity orbitals. The probability for such a process (i.e., the scattering rate) is directly proportional to the weight for transitions between the f^0 and f^1 configurations. The latter quantity is just the f density of states. Formally, the scattering rate per unit impurity concentration C is

$$N(0)\tau^{-1}(\omega)/C=N\Gamma\rho_f(\omega)\ . \tag{3.11}$$

This rate is energy and temperature dependent; the Kondo effect leads to a strong scattering resonance near the Fermi surface. The resistivity ρ, thermopower S, and thermal conductivity κ may be expressed as averages of the conduction electron lifetime (see Sec. V C); since the scattering rate assumes an approximate scaling form at low energies and temperatures, these transport properties are also universal functions of the scaled temperature T/T_0 in limited temperature ranges. Results are plotted in Figs. 15–18 for the parameter sets of Table I. All transport properties exhibit scaling at temperatures $T\leq T_0$ in the valence range studied. Deviations from scaling are evident in the thermopower and thermal conductivity at higher temperatures. The source of these deviations may be simply understood: S and κ measure averages of the conduction electron lifetime weighted by a power of the electronic excitation energy. These properties are consequently more sensitive than the resistivity to nonuniversal

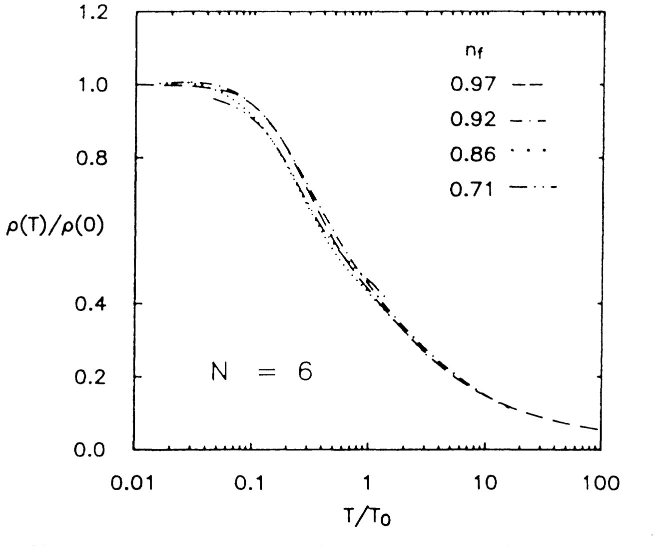

FIG. 15. Temperature variation of the scaled resistivity $\rho/\rho(0)$. Parameters are summarized in Table I. The resistivity is roughly logarithmic in temperature for $T\sim T_0$, but the logarithmic region extends for no more than a decade. For the lowest temperature studied ($T/T_0\sim0.05$), the resistivity shows a quadratic saturation, $\rho(T)/\rho(0)\sim 1-\alpha(T/T_0)^2$, with $\alpha\sim5$ for $N=6$; a quadratic saturation is expected on the basis of general Fermi-liquid arguments. (The self-consistent large-degeneracy expansion is inadequate for describing the extreme Fermi-liquid regime $T\to0$: see Appendix C.)

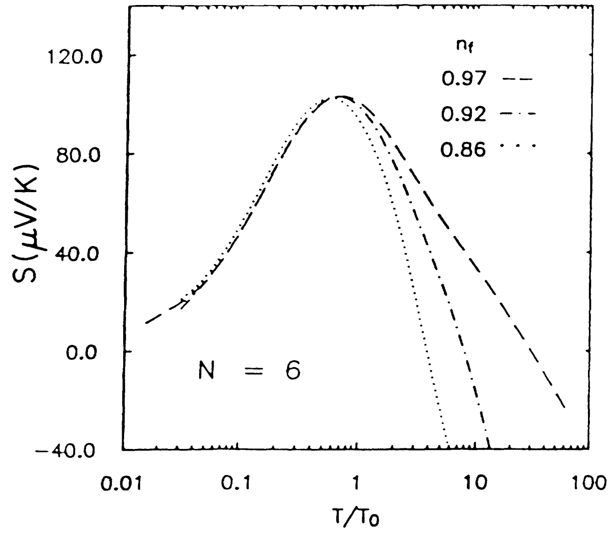

FIG. 16. Temperature variation of the thermopower S. For $N=6$, the thermopower shows a giant peak value of ~ 105 μV/K at $T/T_0=0.9$. In comparison, the thermopower in a typical metal is of order 1 μV/K. Significant deviations from scaling appear for $T/T_0 \sim 1$.

features of the f density of states far from zero energy, and deviations from scaling show up at relatively low temperatures.

The valence and transport properties are rigorously related to the f density of states. Two additional properties, the specific heat $C(T)$ and magnetic susceptibility $\chi(T)$ are simply related to the density of states in a noninteracting system. This relationship breaks down in the presence of interactions. Both $C(T)$ and $\chi(T)$ are thermodynamic properties which probe the full many-body density of states; this full density is not simply related to ρ_f. As stated previously, a Fermi liquid picture based on weakly interacting quasiparticles holds only for $T \rightarrow 0$; the quasiparticle density of states is also distinct from ρ_f.

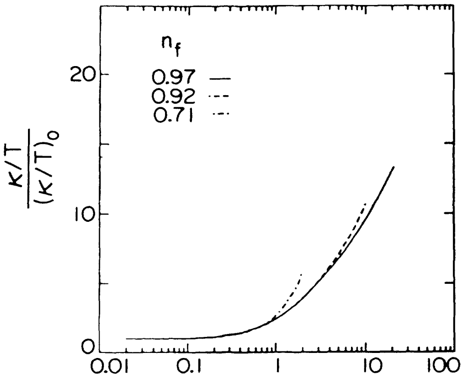

FIG. 17. Temperature variation of the linear coefficient of the thermal conductivity κ/T. At temperatures $T \ll T_0$, the thermal conductivity is linear in T, as expected in a Fermi liquid. Both the electrical and thermal conductivities are limited by the presence of the Kondo resonance, which strongly scatters conduction electrons near the Fermi surface; as the resonance diminishes with increasing temperature, the thermal conductivity coefficient κ/T increases rapidly. As in the case of the thermopower, deviations from scaling appear for $T \sim T_0$.

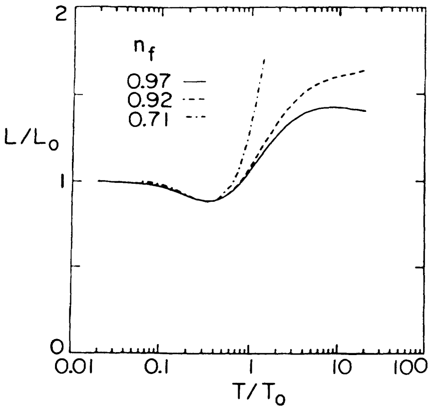

FIG. 18. Lorenz ratio, $L=\kappa\rho/T$, scaled by the Sommerfeld value $L_0=\pi^2/3$. The Lorenz ratio compares the values of the thermal conductivity coefficient and the electrical conductivity: the expected ratio in any system with Fermi excitations is $\pi^2/3$ at sufficiently low temperatures. In the present case, L/L_0 has a minimum at $T/T_0 \sim 0.4$ and rapidly increases for $T/T_0 > 1$. Deviations from scaling appear for $T/T_0 \sim 0.5$.

The static susceptibility instead follows directly from knowledge of the f moment spectrum:

$$\chi(T) = \mathrm{P} \int_{-\infty}^{\infty} d\varepsilon \frac{\sigma_f(\varepsilon)}{\varepsilon} , \tag{3.12}$$

where P denotes a principal value. When scaled by its value for $T \rightarrow 0$, the susceptibility has the form shown in Fig. 19. At high temperatures, χ exhibits Curie law behavior, i.e., it falls off as $1/T$. (This fact is obscured in the logarithmic plot.) The singlet ground state begins to strongly influence the susceptibility when the temperature reaches the characteristic scale T_0. Below this temperature, the susceptibility crosses over to a Pauli-type form. An effective temperature-dependent moment may be defined by

$$\mu_{\mathrm{eff}}^2(T) = 3T\chi(T) ; \tag{3.13}$$

as $T \rightarrow 0$, the effective moment is quenched away (see Fig. 20). Note that the susceptibility exhibits a maximum at finite temperature. This is a characteristic of systems with large magnetic degeneracy. No such maximum occurs for degeneracies $N=2$ and 3.[30]

The final property considered within the present treatment is the specific heat. The specific heat may not be expressed in terms of a single-particle density of states and is not directly related to ρ_f or σ_f. The specific heat may instead be computed directly as a thermodynamic derivative of the system's partition function. The result is plotted in Fig. 21 for the parameter sets of Table I. In the integral valent limit, the net entropy associated with this anomaly

$$S(T) = \int dT\, C(T)/T \tag{3.14}$$

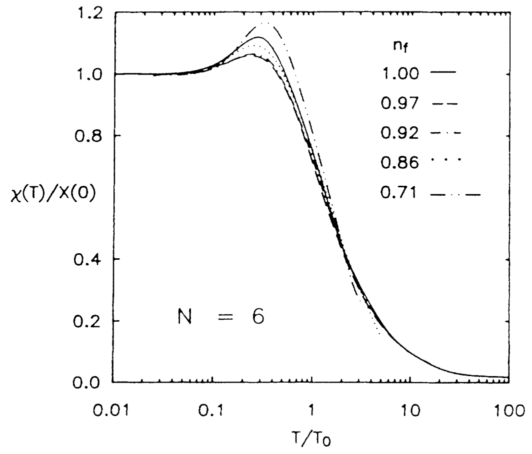

FIG. 19. Temperature variation of the magnetic susceptibility. Parameters are summarized in Table I. The curves for f valence 0.97–0.71 are results of the large-degeneracy expansion. The curve for integral valence is a Bethe-*ansatz* result, shown for comparison. A value of T_0 for the Bethe-*ansatz* curve was obtained by matching the high-temperature susceptibility for $n_f=0.97$. The same value of T_0 was used in the comparison of specific-heat results (Fig. 21). The susceptibility saturates for $T\rightarrow 0$ at a value inversely proportional to the low-energy scale T_0; in comparison, the susceptibility of a free moment diverges for $T\rightarrow 0$. The susceptibility exhibits a weak maximum at $T/T_0\sim 0.5$.

approaches $k_B\ln N$ (where $N=6$) within calculational accuracy. This is the entropy liberated when the f orbital degrees of freedom are "unfrozen," and magnetic states are highly populated. Note that in the ultra-high-temperature limit the entropy must saturate to $k_B\ln(N+1)$; the extra degree of freedom corresponds to high-lying states in the f^0 configuration.

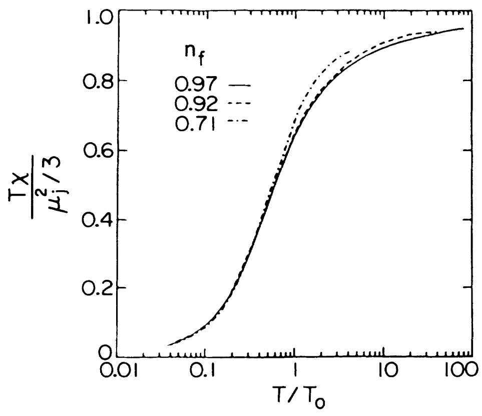

FIG. 20. Temperature variation of the effective moment $\mu_{\text{eff}}^2(T)=3T\chi(T)$, scaled by its ionic value $j(j+1)(g\mu_B)^2$. The scaled moment approaches one at high temperature, but is rapidly quenched toward zero as T decreases. This reflects the diminishing importance of low-lying magnetic states and the emergence of the nonmagnetic ground state at low temperatures. The curves for f valence 0.97 and 0.92 exhibit approximate scaling over more then three decades.

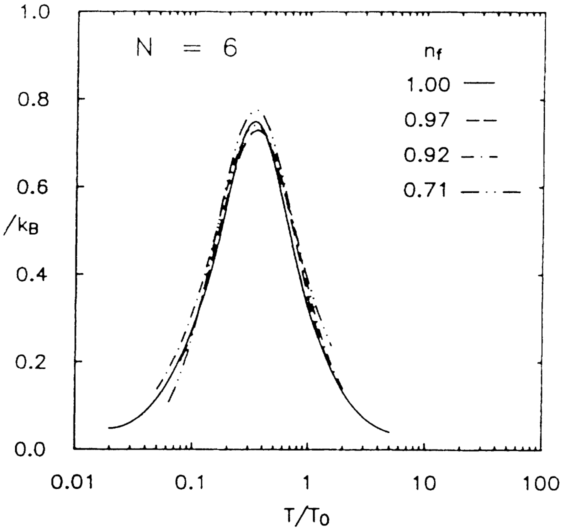

FIG. 21. Temperature variation of the impurity specific heat C. The specific heat for the parameter sets of Table I is compared with the Bethe-*ansatz* result for $n_f=1$; the value of T_0 for the Bethe-*ansatz* curve is the same as that used in Fig. 19. The results of the large-degeneracy expansion are in good agreement with the Bethe-*ansatz* result. The entropy associated with this specific heat anomaly ($\sim\ln 6$) counts the impurity degrees of freedom "frozen out" in the nonmagnetic ground state.

The dependence of the properties discussed above on ρ_f and σ_f is summarized in Table II. The spectra provide a unifying framework, since each is, in principle, directly measurable, and essentially all other properties are derived from them. The method for calculating these spectra and the partition function is presented in the next section.

IV. MODEL AND CALCULATIONAL SCHEME

The degenerate Anderson Hamiltonian introduced in Sec. II has the form

$$H_A=H_{\text{band}}+H_f+H_{\text{mix}}\ ,$$

where

$$\begin{aligned} H_{\text{band}}&=\sum_{k,m}\varepsilon_k n_{km}\ ,\\ H_f&=\varepsilon_f\sum_m \hat{N}_m\ ,\\ H_{\text{mix}}&=V\sum_{k,m}(c_{km}^\dagger F_m+\text{H.c.})\ , \end{aligned} \tag{4.1a}$$

where

$$\begin{aligned} \hat{N}_m&=|m\rangle\langle m|\ ,\\ F_m&=|0\rangle\langle m|\ . \end{aligned} \tag{4.1b}$$

(The zero of energy is set by the noninteracting Fermi sea and the empty f orbital.) A perturbation expansion for this Hamiltonian may be developed using a general tech-

TABLE II. Dependence of properties on the dynamic spectra ρ_f and σ_f. The f density of states and moment spectrum provide a unifying framework for understanding static and dynamic properties of the Anderson model. The dependence of various properties on these spectra is summarized below.

(1) f density of states $\rho_f(\epsilon)$

f valence

$$n_f=\int_{-\infty}^{\infty} d\epsilon\, f(\epsilon)\rho_f(\epsilon)$$

Conduction-electron scattering rate per unit concentration

$$N(0)\tau^{-1}(\epsilon)/C=N\Gamma\rho_f(\epsilon)$$

Transport properties

$$L_n(T)=\frac{2[N(0)]^2k_F^2}{3m^2C}\int_{-\infty}^{\infty} d\epsilon \left[-\frac{\partial f}{\partial\epsilon}\right]\epsilon^n[N(0)\tau^{-1}(\epsilon)/C]^{-1}$$

resistivity $\rho=\frac{1}{e^2L_0}$

thermopower $S=-\frac{1}{eT}\frac{L_1}{L_0}\quad(e=|e|)$

thermal conductivity $\kappa=\frac{1}{T}\left[L_2-\frac{L_1^2}{L_0}\right]$

(2) f moment spectrum $\sigma_f(\epsilon)$

Dynamic susceptibility

$$\text{Im}\chi(\epsilon+i0^+)=\pi\sigma_f(\epsilon)$$

Static susceptibility

$$\chi=P\int_{-\infty}^{\infty} d\epsilon\frac{\sigma_f(\epsilon)}{\epsilon}$$

nique for treating systems with strong local correlations.[45] The presence of the projection operators F_m precludes the combination of particle and hole diagrams using the Feynman propagator; traditional Feynman techniques may be applied using the "pseudo-Hamiltonian," or "auxiliary boson," approach.[46,47,38] The pseudo-Hamiltonian approach is complicated by the need for a projection scheme to remove contributions to operator averages from unphysical states. The present approach is considerably more direct, involves no unphysical states, and has a simpler set of diagrammatic rules.

Before introducing the rules for diagrammatic perturbation theory, we summarize our conventions for conduction state normalization: plane-wave conduction states of spin σ are created by operator $c_{\mathbf{k}\sigma}^{\dagger}$, with

$$\{c_{\mathbf{k}\sigma},c_{\mathbf{k}'\sigma'}^{\dagger}\}=(2\pi)^3\delta(\mathbf{k}-\mathbf{k}')\delta_{\sigma\sigma'}$$

and

$$\sum_{\mathbf{k},\sigma}\to\sum_{\sigma}\int\frac{\mathcal{V}}{(2\pi)^3}d\mathbf{k}\to\sum_{\sigma}N(0)\int d\varepsilon\ . \tag{4.2}$$

Here, $\mathcal{V}$ is the system volume and $N(0)$ the single-spin density of states per unit energy. Spherical-wave states with angular momentum $(l,j,m_j=m)$ are created by operator $c_{km}^{\dagger}$ (l and j suppressed), with

$$\{c_{km},c_{km'}^{\dagger}\}=\frac{(2\pi)^3}{4\pi k^2}\delta(k-k')\delta_{mm'}$$

and (4.3)

$$\sum_{k,m}\to\sum_{m}\int\frac{4\pi k^2}{(2\pi)^3}dk\to\sum_{m}N(0)\int d\varepsilon\ .$$

Plane- and spherical-wave states are related[48] by

$$c_{km}^{\dagger}=\sqrt{4\pi}\sum_{\sigma}\langle\sigma\,|\,m\rangle\int\frac{d\hat{\mathbf{k}}}{4\pi}Y_{l,m-\sigma}(\mathbf{k})c_{\mathbf{k}\sigma}^{\dagger}\ ,$$
$$\langle\sigma\,|\,m\rangle=\langle l\,\tfrac{1}{2}\,m-\sigma\,\sigma\,|\,j\,m\rangle\ . \tag{4.4}$$

We discuss first the evaluation of the Anderson partition function. The partition function may be written as

$$Z=\text{Tr}_f\text{Tr}_{\text{band}}\,e^{-\beta H}\ , \tag{4.5}$$

where the traces are over the set of noninteracting band states and noninteracting f orbital states. Introducing a contour integral representation gives

$$Z=\int_{\Gamma}\frac{dz}{2\pi i}e^{-\beta z}\text{Tr}_f\text{Tr}_{\text{band}}\frac{1}{z-H}\ , \tag{4.6a}$$

where the contour Γ encircles all singularities of the integrand in a counterclockwise fashion; the operator $(z-H)^{-1}$ may be decomposed formally as

$$(z-H)^{-1}=\sum_{\Phi}\frac{|\Phi\rangle\langle\Phi|}{z-E_{\Phi}}\ , \tag{4.6b}$$

where the states Φ are eigenstates of the full Anderson Hamiltonian. Thus, writing out the traces in Eq. (4.6) explicitly gives

$$Z=\int_{-\infty}^{\infty}d\varepsilon\, e^{-\beta\varepsilon}\sum_{\Phi,N^{\text{band}}}\left[|\langle 0;N^{\text{band}}|\Phi\rangle|^2+\sum_{m}|\langle m;N^{\text{band}}|\Phi\rangle|^2\right]\delta(\varepsilon-E_{\Phi})\ . \tag{4.7}$$

This is a physically appealing decomposition of Z: the sum over states, weighted by the delta function, is just the temperature-independent density of many-particle levels with energy ε. This expression is not convenient for perturbation theory, however. It is useful to separate out the Boltzmann weight of the conduction states by shifting the variables of integration z and ε by energy E_N^{band} in each element of the sum. Thus,

$$Z=\int_{-\infty}^{\infty}d\varepsilon\, e^{-\beta\varepsilon}\sum_{\Phi N^{\text{band}}}e^{-\beta E_N^{\text{band}}}\left[|\langle 0;N^{\text{band}}|\Phi\rangle|^2+\sum_{m}|\langle m;N^{\text{band}}|\Phi\rangle|^2\right]\delta(\varepsilon+E_N^{\text{band}}-E_{\Phi})\ . \tag{4.8}$$

The sum over states may no longer be interpreted as a physical density of many-particle levels; however, a great deal is gained by this shift of variables. Dividing Eq. (4.6) by Z_{band}, the partition function of the noninteracting conduction band, gives

$$Z_f \equiv Z/Z_{\text{band}} = \int_\Gamma \frac{dz}{2\pi i} e^{-\beta z} \mathrm{Tr}_f \sum_{N^{\text{band}}} \frac{e^{-\beta E_N^{\text{band}}}}{Z_{\text{band}}} \left\langle N^{\text{band}} \left| \frac{1}{z + E_N^{\text{band}} - H} \right| N^{\text{band}} \right\rangle . \tag{4.9}$$

The sum over conduction states is now written as a thermal average; the result of the sum is an operator acting within the space of f-orbital states. Remarkably, this f operator may be written in the form

$$\sum_{N^{\text{band}}} \frac{e^{-\beta E_N^{\text{band}}}}{Z_{\text{band}}} \left\langle N^{\text{band}} \left| \frac{1}{z + E_N^{\text{band}} - H} \right| N^{\text{band}} \right\rangle = G_0(z) \,|\, 0 \rangle\langle 0 \,|\, + \sum_m G_m(z) \,|\, m \rangle\langle m \,| \ , \tag{4.10}$$

with

$$G_0(z) \equiv \frac{1}{z - \Sigma_0(z)} \ ,$$

$$G_m(z) \equiv \frac{1}{z - \varepsilon_f - \Sigma_m(z)} \ ;$$

the functions Σ_0 and Σ_m may be interpreted as "self-energies" for the empty and occupied states; we shall frequently refer to G_0 and G_m as empty- and occupied-state propagators. The introduction of these propagators is useful since Σ_0 and Σ_m have simple diagrammatic representations (see Fig. 22).

The equation analogous to (4.9) which follows from separating out conduction degrees of freedom in this way is

$$Z_f = \int_{-\infty}^{\infty} d\varepsilon \, e^{-\beta\varepsilon} \left[\rho_0(\varepsilon) + \sum_m \rho_m(\varepsilon) \right] ,$$

with

$$\begin{aligned} \rho_0(\varepsilon) &= -\frac{1}{\pi} \mathrm{Im} G_0(\varepsilon + i0^+) \ , \\ \rho_m(\varepsilon) &= -\frac{1}{\pi} \mathrm{Im} G_m(\varepsilon + i0^+) \ . \end{aligned} \tag{4.11}$$

The functions ρ_0 and ρ_m may be interpreted as effective densities of states, or distribution functions, for the empty and occupied f-orbital configurations. In the presence of hybridization, ρ_0 and ρ_m are temperature-dependent; on the other hand, in the absence of hybridization, it may be checked that

$$\begin{aligned} \rho_0(\varepsilon) &= \delta(\varepsilon) \ , \\ \rho_m(\varepsilon) &= \delta(\varepsilon - \varepsilon_f) \ , \end{aligned} \tag{4.12}$$

giving

$$Z_f = 1 + N e^{-\beta\varepsilon_f} \ .$$

It is important to note that these quantities are *not* spectral densities for dynamic correlation functions, and hence are not physically measurable. Nevertheless, they allow an intuitive picture of Anderson model thermodynamics based on effective f configurations with conduction electron degrees of freedom "averaged out." Rules for evaluating the self-energies Σ_0 and Σ_m are summarized in Table III. As an example, consider the contribution to the empty-state self-energy in Fig. 23. Applying the rules in Table III gives

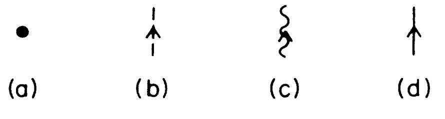

FIG. 22. Components of diagrammatic perturbation theory for the infinite-U Anderson model. (a) Vertex. Each hybridization event is represented by a solid dot, with an accompanying factor of V. (b) Occupied f-orbital line. The N singly occupied f-orbital states are represented by dashed lines. (c) Empty f-orbital line. The empty orbital is represented by a wavy line. (d) Conduction electron line. Conduction electrons are represented by solid lines.

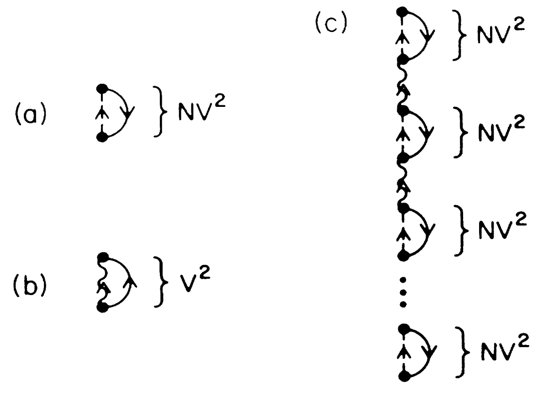

FIG. 23. Contributions to the f configuration self-energies. (a) Lowest-order contribution to the empty-state self-energy. The f and conduction electron lines may have N different magnetic labels, so the diagram is $O(NV^2) = O(1)$. (b) Lowest-order contribution to the occupied-state self-energy. The conduction electron is restricted to a single magnetic channel by angular momentum conservation; hence, this diagram is $O(V^2) = O(1/N)$. (c) n-fold repetition of the diagram in (a). A factor of N accompanies each of the occupied-state–conduction-electron loops.

TABLE III. Diagrammatic rules for evaluating configurational self-energies in the infinite-U Anderson model. We list below rules for evaluating the empty- and occupied-state self-energies in the infinite-U Anderson model.

To compute a general contribution to the empty-state (occupied-state) self-energy at $O(V^{2n})$, $n \geq 1$:

(a) Set down $2n$ vertices in a vertical line. Beginning at the bottom with a dashed (wavy) line, connect the vertices with alternate dashed and wavy lines (all ascending). (A total of $2n-1$ lines now appear.)

(b) Always working to the right of the vertical line, connect the vertices with full lines in all possible ways which maintain the direction of the dashed lines at each vertex. Disregard diagrams which may be disconnected by cutting a single local configuration line—they do not contribute to the irreducible self-energy.

(c) Assign quantum numbers km (m) to solid lines (dashed lines), conserving angular momentum at each vertex.

(d) Assign to ascending conduction lines a factor $1-f_{km}$ and to descending conduction lines a factor f_{km}, with f the Fermi function. Draw a perpendicular to each local configuration line, and assign to it an energy denominator $(z-E_\alpha)^{-1}$, where E_α is found by adding the energies of ascending lines intersected by the perpendicular and subtracting the energies of descending lines intersected.

(e) Multiply the product of energy denominators and Fermi factors by $V^{2n}(-)^c$, where c is the number of conduction line crossings. Sum on all internal variables.

$$\Sigma_0^{(1)}(z)=NV^2\sum_k \frac{f_k}{z+\varepsilon_k-\varepsilon_f} =NV^2 \ln\left|\frac{\varepsilon_f-z}{D}\right| , \tag{4.13}$$

for a flat density of conduction states with halfwidth D.

The simplest perturbation theory based on the technique outlined above treats the hybridization V as a small parameter. Infinite order summations in the hybridization are necessary to develop a reasonable picture of the system's behavior. Instead of perturbing in V, it is useful to develop an expansion based on a second parameter of the model, the magnetic degeneracy N. Such expansions have previously been employed for a number of problems in statistical mechanics and field theory.[37] Even low-order approximations in the small parameter $1/N$ contain the dominant features of the Kondo effect. The expansion may be motivated by considering the corrections to the propagators G_0 and G_m at lowest order in the hybridization V (Fig. 23). Note that N distinct loops may be inserted in the empty-state propagator at $O(V^2)$: this simply reflects the magnetic degeneracy of the f^1 configuration. In contrast, only a single empty-state–conduction-electron loop may be inserted in the occupied-state propagator at $O(V^2)$: by angular momentum conservation, the band electron propagates in the same spherical wave channel as the f electron. If the process in Fig. 23(a) is repeated n times, the resulting diagram [Fig. 23(c)] contains a prefactor $(NV^2)^n$; in order to have a well-defined limit, the factor NV^2 (or alternatively $N\Gamma$) must be treated as $O(1)$. The process in Fig. 23(b) is then $O(1/N)$. Arbitrary diagrams in the propagator expansions may be classified in powers of $1/N$ by simply counting vertices and electron loops.

Hence, a systematic expansion of propagators (and correlation functions) in $1/N$ may be attempted. Such an expansion is not uniform in frequency, however, and does not lead to smooth correlation functions. In order to remedy this shortcoming, it is necessary to perform an infinite-order summation in $1/N$.

The simplest infinite-order summation is based on a self-consistent approximation for the empty- and occupied-state propagators, shown diagrammatically in Fig. 24. This approximation resembles the lowest order treatment of Fig. 23: the difference is that in this case the internal f lines are not bare, but are dressed to infinite order. More formally, the approximation requires solving the following coupled integral equations[8] for the self-energies Σ_0 and Σ_m introduced in (4.10):

$$\begin{aligned}\Sigma_0(\omega+i0^+)&=NV^2\sum_k f_k G_m(\omega+\varepsilon_k+i0^+) ,\\ \Sigma_m(\omega+i0^+)&=V^2\sum_k(1-f_k)G_0(\omega-\varepsilon_k+i0^+) .\end{aligned} \tag{4.14}$$

These equations result immediately from the diagrammatic rules in Table III.


(a) (b)

FIG. 24. Self-consistent f configuration self-energies. The double-dashed and double-wavy lines represent dressed propagators containing infinite repetitions of the lowest-order self-energy in Fig. 23. (a) Empty-state self-energy. (b) Occupied-state self-energy.

This approximation for the impurity propogators is commonly referred to as the noncrossing approximation, or NCA.[29] The basis for the name is the fact that all diagrams included may be drawn with noncrossing conduction electron lines. We shall refer to the approximation throughout this paper as the "self-consistent large-degeneracy expansion." The lowest-order diagrams omitted within this approximation appear in Fig. 25. Thus, error in the empty-state propagator is formally $O(1/N^2)$, and error in the occupied-state propagator is $O(1/N^3)$. The error in the partition function Z_f is $O(1/N^2)$ from both the empty and occupied states: the latter error arises since N identical occupied-state contributions appear in Z_f. Details on the numerical solution of Eqs. (1.14) are summarized in Appendix A. (See also the discussion in Refs. 49 and 50.)

The temperature dependence of the distribution functions $\rho_0(\varepsilon)$ and $\rho_m(\varepsilon)$ for a typical parameter set is illustrated in Figs. 26–28. A Lorentzian density of conduction states with halfwidth D was employed in all numerical calculations; a smoothly varying density of states is convenient, since band edge effects need not be considered.

Although these distribution functions are not directly measurable, their prominent features are reflected in the physical spectral densities, such as the f density of states and the f moment spectrum. For this reason, it is of interest to examine the self-energies Σ_0 and Σ_m more closely (see Fig. 29). An expression for Σ_0 may be derived analytically at $O(1)$ for a flat density of states. (A Lorentzian density of states has been employed in numerical studies, but analytical calculations are simplest for a flat profile. Similar results are obtained for any profile with characteristic energy D.) For a flat density of states, the empty-state self-energy at zero temperature has the form

$$\Sigma_0(\omega+i0^+)=\frac{N\Gamma}{\pi}\int_{-D}^{0}d\varepsilon\, G_m(\omega+\varepsilon+i0^+)\;; \qquad (4.15a)$$

replacing G_m with its value in the absence of interactions

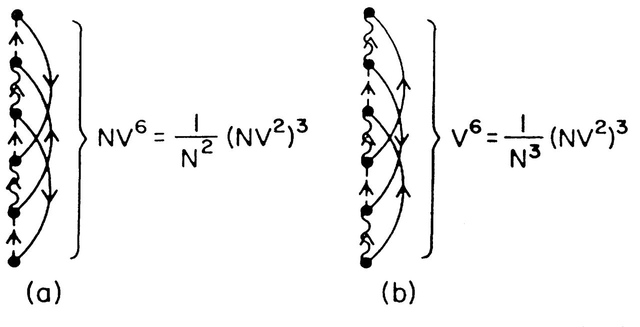

FIG. 25. Lowest-order self-energy diagrams omitted in the self-consistent large-degeneracy expansion. (a) Empty-state self-energy. This diagram contains a single sum on magnetic quantum numbers and six vertices; it is $O(NV^6)=O(1/N^2)$. Note that three conduction line crossings appear. (b) Occupied-state self-energy. This diagram also contains six vertices, but in this case there is no sum on magnetic quantum numbers; it is $O(V^6)=O(1/N^3)$. Again three conduction line crossings appear.

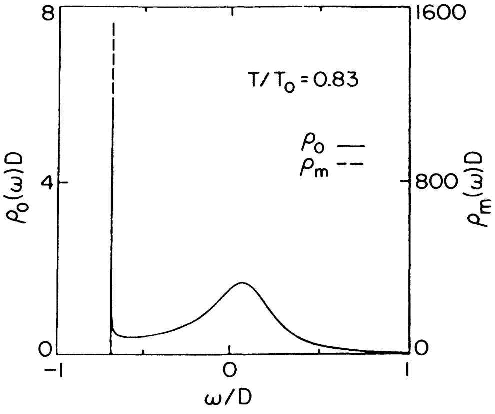

FIG. 26. Gross features of the f distribution functions ρ_0 and ρ_m for $T<T_0$. A Lorentzian conduction band profile with halfwidth D has been assumed. The f-orbital energy $\epsilon_f/D=-0.67$, and the hybridization width $\Gamma/D=0.05$. In the absence of hybridization, ρ_0 is a delta function at energy 0; in the presence of hybridization, this delta function is smeared into a broad resonance, and a small feature develops below the f-orbital energy at $\sim -0.69D$ (shown in detail in Fig. 27). This resonance becomes increasingly sharp with decreasing temperature; it indicates the presence of a small f^0 component $(\sim\pi T_0/N\Gamma)$ in low-lying many-particle eigenstates. The occupied-state distribution function ρ_m is a sharp resonance (shown in detail in Fig. 28), which lies above the low-energy feature in ρ_0 by approximately T_0.

gives

$$\Sigma_0^{(1)}(\omega+i0^+)=\frac{N\Gamma}{\pi}\ln\left|\frac{\varepsilon_f-\omega-i0^+}{D}\right| . \qquad (4.15b)$$

Resonances are expected in $\rho_0^{(1)}\omega$ at points where

$$\omega-\mathrm{Re}\Sigma_0^{(1)}(\omega)=0 \;. \qquad (4.16)$$

For parameters in the Kondo regime, this equation has three solutions: a solution $\omega^{(3)}$ near zero energy is the remnant of the pole in the noninteracting system [cf. Eq.

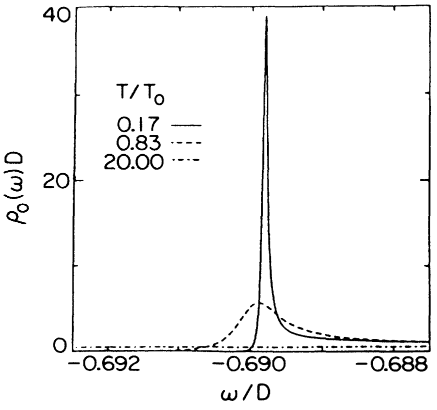

FIG. 27. Temperature dependence of the empty-state distribution function ρ_0 in the vicinity of the ground-state energy. Parameter choices are the same as those in Fig. 26.

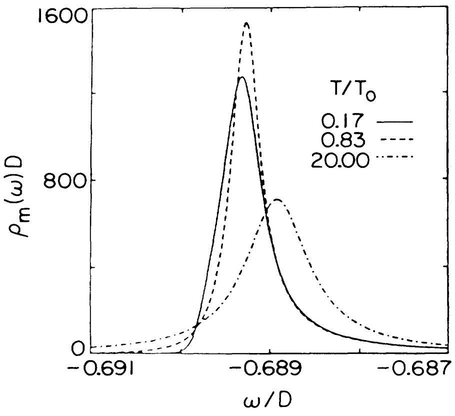

FIG. 28. Temperature dependence of the occupied-state distribution function ρ_m. Parameter choices are the same as those in Fig. 26. In the absence of hybridization, ρ_m is a delta function at energy ϵ_f; hybridization shifts the resonance to lower energies and broadens it. As the temperature increases, the resonance first narrows, then broadens. The resonance in ρ_m is much broader than the corresponding feature in ρ_0. At the crudest level, the empty-state feature may be replaced by a delta function in approximate calculations.

(4.12)]; in addition, solutions appear just above and just below ε_f, the energy of the noninteracting f multiplet. The solution above ε_f, $\omega^{(2)}$, has no important effect, since it lies in a region where $\mathrm{Im}\Sigma_0$ is large. The final solution at

$$\omega^{(1)} \equiv \varepsilon_f - T_0^{(1)} \tag{4.17a}$$

is completely undamped at zero temperature. For a flat density of states,

$$T_0^{(1)} = T_A$$

with

$$\varepsilon_f - T_A = \frac{N\Gamma}{\pi} \ln \left[\frac{T_A}{D} \right] ,$$

i.e.,

$$T_A \approx D \exp \left[\frac{\pi \varepsilon_f}{N\Gamma} \right] . \tag{4.17b}$$

For a more general density of states (such as the Lorentzian), $T_0^{(1)}$ assumes the same form up to exponential order. The residue of the pole at $\omega^{(1)}$ is

$$\left[1 - \frac{\partial \Sigma_0^{(1)}}{\partial \omega} \right]^{-1} = \left[1 + \frac{N\Gamma}{\pi T_A} \right]^{-1} \tag{4.17c}$$

for the flat density of states. In the Kondo regime $(-\varepsilon_f >> N\Gamma)$, this residue is extremely small.

This new pole, which has no analog in the absence of interactions, is a direct manifestation of the Kondo effect. A new many-particle state, containing an admixture of the f^0 configuration, lies below the position of the noninteracting f^1 configuration and Fermi sea by the small energy $T_0^{(1)}$. This small energy is the scale for the Kondo effect. Recall that the energy zero is set by the noninteracting f^0 configuration and Fermi sea. It follows that at $O(1)$ the ground-state energy is $\varepsilon_f - T_0^{(1)}$.

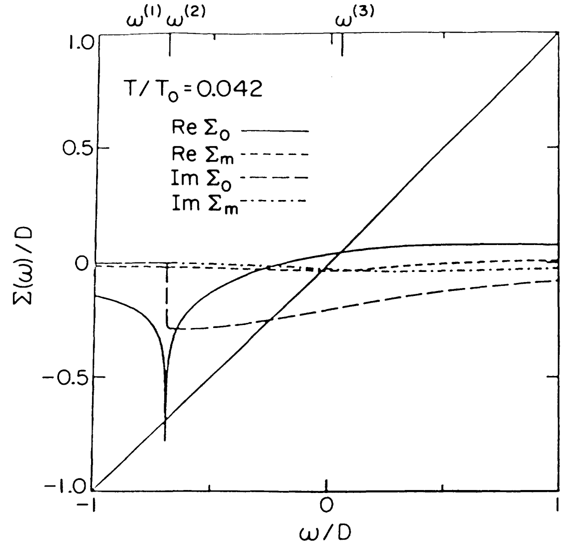

FIG. 29. Empty- and occupied-state self-energies within the self-consistent large-degeneracy expansion. The conduction band is assumed to have a Lorentzian profile with half-width D. Results are shown for parameter set 1 in Table I in the low-temperature limit $(T << T_0)$. The real and imaginary parts of the empty-state self-energy are large; the real part exhibits a sharp singularity near ϵ_f. The equation

$$\omega = \mathrm{Re}\Sigma_0(\omega)$$

has solutions at $\omega^{(1)}$, $\omega^{(2)}$, and $\omega^{(3)}$. In contrast, the occupied-state self-energy has no prominent features.

The finite width of the upper feature in the empty-state distribution function is essentially a single-particle effect. It may be understood on the basis of a golden rule calculation: at zero temperature, the empty-state propagator is just

$$G_0(z) = \left\langle 0;\Omega \left| \frac{1}{z-H} \right| 0;\Omega \right\rangle , \tag{4.18a}$$

with $|\Omega\rangle$ the unperturbed Fermi sea. Thus,

$$G_0(z) = \left\langle 0;\Omega \left| \frac{1}{z-H_0} \right| 0;\Omega \right\rangle + \left\langle 0;\Omega \left| \frac{1}{z-H_0} T \frac{1}{z-H_0} \right| 0;\Omega \right\rangle , \tag{4.18b}$$

with

$$T = H_{\mathrm{mix}} \sum_{n=0}^{\infty} \left[\frac{1}{z-H_0} H_{\mathrm{mix}} \right]^n . \tag{4.18c}$$

By elementary quantum mechanics, the state $|0;\Omega\rangle$ decays in time at the rate

$$\tau^{-1} = -2\,\mathrm{Im}\langle 0;\Omega \mid T \mid 0;\Omega\rangle$$
$$= 2\pi \sum_{N} |\langle N \mid T \mid 0;\Omega\rangle|^2 \delta(E_N) \qquad (4.19)$$

by the optical theorem. Thus, in lowest-order perturbation theory, the halfwidth, of the state $|0;\Omega\rangle$ is just

$$\pi \sum_{k,m} |\langle m;\varepsilon_k \mid H_{\mathrm{mix}} \mid 0;\Omega\rangle|^2 \delta(\varepsilon_f - \varepsilon_k) = \pi N(0) N V^2$$

where (4.20)

$$|m;\varepsilon_k\rangle = F_m^{\dagger} c_{km} \,|0;\Omega\rangle \ .$$

The occupied-state distribution function remains a delta function at $O(1)$. If the self-energy is computed to $O(1/N)$ by inserting the $O(1)$ empty-state propagator in Eq. (4.14), the primary effect is a spectral broadening. This broadening may again be understood by a golden rule calculation: in this case, the state $|m;\Omega\rangle$ (which has one more particle than the state $|0;\Omega\rangle$) may decay at lowest order into

$$|0;E_k\rangle = F_m c_{km}^{\dagger} \,|m;\Omega\rangle \ . \qquad (4.21)$$

By energy conservation, $|m;\Omega\rangle$ cannot decay into the ground state (with the same particle number); it may, however, decay into a continuum state satisfying energy conservation. In an $O(1)$ treatment, continuum states near ε_f contain f^0 admixtures with relative weight $\approx \pi T_0^{(1)}/N\Gamma$. The density of continuum states remains $N(0)$, but in this case the square of the coupling matrix element in the golden rule is

$$|\langle 0;E_k \mid H_{\mathrm{mix}} \mid m;\Omega\rangle|^2 = (\pi T_0^{(1)}/N\Gamma) V^2 \ . \qquad (4.22)$$

Thus, the level width becomes $\approx \pi N(0)(\pi T_0^{(1)}/N\Gamma)V^2 = \pi T_0^{(1)}/N$.

In this simplified picture, the many-particle ground state contains only a small admixture ($\sim \pi T_0^{(1)}/N\Gamma$) of the state $|\Omega\rangle$. The remainder of the ground state is made up of f electron-conduction hole contributions $F_m^{\dagger} c_{km}\,|\Omega\rangle$. The weight of states of this type within a single angular momentum channel is $O(1/N)$; however, the net contribution from all channels is $O(1)$. For this reason, such admixtures must be considered in an $O(1)$ calculation of properties which are not restricted to a single angular momentum channel.

V. CALCULATION OF PHYSICAL PROPERTIES

A. *f* density of states

The f density of states assumes the following form:

$$\rho_f(\omega) = -\frac{1}{\pi}\mathrm{Im}G_f(\omega + i0^+) \ ,$$
$$G_f(\omega + i0^+) = \int_{-\infty}^{\infty} dt\, e^{i(\omega + i0^+)t} \times [-i\Theta(t)\langle\{F_m(t), F_m^{\dagger}(0)\}\rangle] \ , \qquad (5.1)$$
$$F_m \equiv |0\rangle\langle m| \ .$$

The retarded propagator may be evaluated by analytic continuation from the corresponding imaginary-time propagator:

$$G_f(i\omega_n) = \int_0^{\beta} d\tau\, e^{i\omega_n \tau}[-\langle \mathcal{T}_{\tau} F_m(\tau) F_m^{\dagger}(0)\rangle] \ . \qquad (5.2)$$

Rules for computing general contributions to G_f are presented in Table IV. The diagram representing $G_f(i\omega_n)$ in the noninteracting system is shown in Fig. 30(a). This diagram may be trivially dressed to $O(1/N)$ by replacing the bare empty-state and occupied-state propagators with self-consistently dressed propagators [Fig. 30(b)]. The contributions omitted in this procedure are $O(1/N^2)$. The first nontrivial vertex correction which cannot be obtained by simply dressing G_0 and G_m to higher order is shown in Fig. 30(c). Since contributions of $O(1/N^2)$ are omitted in computing G_0 and G_m, it is consistent to neglect the additional vertex corrections in G_f.

Thus, within the self-consistent large-degeneracy expansion,

$$G_f(i\omega_n) = \frac{1}{Z_f}\int_{\Gamma} \frac{dz}{2\pi i} e^{-\beta z} G_0(z) G_m(z + i\omega_n) \ , \qquad (5.3)$$

where Γ encircles all singularities of the integrand in a counterclockwise fashion. Introducing spectral representations,

$$G_f(i\omega_n) = \frac{1}{Z_f}\int_{-\infty}^{\infty} d\varepsilon\, e^{-\beta\varepsilon}[\rho_0(\varepsilon) G_m(\varepsilon + i\omega_n) - G_0(\varepsilon - i\omega_n)\rho_m(\varepsilon)] \ . \qquad (5.4)$$

Thus,

$$\rho_f(\omega) = \frac{1}{Z_f}(1 + e^{-\beta\omega})\int_{-\infty}^{\infty} d\varepsilon\, e^{-\beta\varepsilon}\rho_0(\varepsilon)\rho_m(\varepsilon + \omega) \ . \qquad (5.5)$$

This physical density of states is a convolution of the f^0 and f^1 distribution functions. This might have been expected, since ρ_f measures the weight for transitions between these two configurations. In principle, a similar density of states may be derived directly from the Anderson Hamiltonian with a large finite Coulomb interaction; the present approach circumvents the need for perturbation theory with a large U term.

At low temperatures, the f density of states has two dominant features, a broad resonance near the position of the f level in the noninteracting system and a narrow *Kondo resonance* at the small positive energy T_0. (The energy T_0 differs from the energy scale $T_0^{(1)}$ in the lowest order treatment by a factor of order unity.) Physically, the width of the lower resonance arises from the finite lifetime of an empty f state; it may be understood using a golden rule calculation. When an f electron is removed from the system, the local level is rapidly filled by a conduction electron. Due to the orbital's magnetic degeneracy, the empty state "decays" in N channels. Assuming a constant density of conduction states, the filling rate $\tau^{-1} = 2\pi N N(0) V^2$, and the energy half-width is $N\Gamma$. In terms of the f^0 and f^1 distribution functions, the broad resonance in ρ_f results from convoluting the feature in ρ_0 near zero energy with the sharp resonance in ρ_m. The width of the convolution is almost entirely due to the f^0

TABLE IV. Diagrammatic rules for evaluating $G_f(i\omega_n)$. We list below rules for evaluating the normal-state f Green's function $G_f(i\omega_n)$.

To compute a general contribution to $G_f(i\omega_n)$ of $O(V^{2n})$, $n \geq 0$:

(a) Set down $2n+2$ vertices (solid dots) in a vertical line. Beginning at the bottom with a dashed line, connect the vertices with alternating dashed and wavy lines (all ascending), finally leaving the top vertex on a wavy line. (A total of $2n+2$ lines now appear.)

(b) Counting from the bottom, convert the first vertex to an open circle (to represent the operator $F_m^\dagger$; convert an even-numbered vertex to an open circle (to represent the operator F_m).

(c) Always working to the right of the vertical line, connect the remaining $2n$ vertices with full lines in all possible ways which maintain the direction of the dashed line at each vertex.

(d) Working on the left side of the diagram, connect the open circles with a dash-dotted "external line," carrying energy $i\omega_n$ from top to bottom.

(e) Assign quantum numbers km (m) to solid lines (dashed lines), conserving angular momentum at each vertex.

(f) Assign to ascending band lines a factor $1-f_{km}$ and to descending band lines a factor f_{km}, with f the Fermi function.

(g) Draw a perpendicular to each local configuration line, and assign to it an energy denominator $(z-E_\alpha)^{-1}$, where E_α is found by adding the energies of ascending lines intersected by the perpendicular and subtracting the energies of descending lines intersected.

(h) Multiply the product of energy denominators and Fermi factors by $V^{2n}(-)^c$. Here c is the number of line crossings on the right side of the diagram. Sum on conduction momenta and internal angular momenta.

(i) Compute the contour integral

$$\frac{1}{Z_f}\int_\Gamma \frac{dz}{2\pi i} e^{-\beta z} R(z)\,,$$

where R is the result of the preceding operations, Z_f is the system partition function, and Γ encircles all singularities of R in a counterclockwise fashion.

distribution.

The narrow resonance at energy T_0 results from the presence of an f^0 admixture in the interacting ground state. In terms of the f^0 and f^1 distribution functions, the resonance is the convolution of the sharp feature in ρ_0 at $\tilde{\varepsilon}_f - T_0$ and the resonance in ρ_m at $\tilde{\varepsilon}_f$. Physically, the small weight of the resonance reflects the fact that the f^0 admixture is small; the integrated weight of the resonance is $\approx \pi T_0/N\Gamma$, the weight of the feature in ρ_0. As the temperature increases, the Kondo resonance is smeared out. Physically, this is because at finite temperatures the many-particle eigenstates of the system are thermally populated; the density of states measures a weighted average of the one-particle excitations from a continuum of states. The zero-temperature Kondo resonance measures the weight for exciting the system from the ground state into a low-lying state with large f^1 weight. When the temperature becomes of order T_0, the weight for exciting continuum-to-continuum transitions becomes comparable, and the unique ground state signature disappears. The eigenstates of the system are, of course, temperature-independent; the system's behavior changes with increasing temperature as the weight of the ground state in thermal averages diminishes.

The temperature dependence of the Kondo resonance has been discussed briefly in Sec. III. The resonance is clearly visible even when the temperature becomes of order $10T_0$. This high-temperature remnant of Kondo behavior is reflected in the logarithmic corrections which appear in low-order perturbative studies of Anderson model properties. The resonance effectively reaches its zero-temperature limit at temperatures of order $0.1T_0$. The scaling properties of the resonance have also been discussed in Sec. III. The existence of approximate scaling may be derived analytically from the equations determining the f^0 and f^1 propagators. Physically, scaling is expected so long as the nonperturbative low-energy scale T_0 is smaller than all other relevant parameters of the system, such as the hybridization width, the f-orbital energy, and the band width.

With knowledge of the f density of states, it is possible to reconstruct the full f Green's function

$$G_f(\omega+i0^+)=\frac{1}{\omega-\varepsilon_f-\Sigma_f(\omega+i0^+)} \tag{5.6}$$

and to extract a "physical" self-energy (to be distinguished from the configurational self-energies Σ_0 and Σ_m). Since the exact self-energy obeys a number of Fermi liquid relations in the zero-temperature limit, this allows an additional test of the approximate solution. The reconstruction is based on the equations

$$\mathrm{Re}G_f(\omega)=\mathrm{P}\int_{-\infty}^{\infty}d\varepsilon\frac{\rho_f(\varepsilon)}{\omega-\varepsilon}\ , \tag{5.7}$$

where P denotes a principal value, and

$$\begin{aligned}\mathrm{Im}\Sigma_f(\omega+i0^+)&=-\frac{\pi\rho_f(\omega)}{\mathrm{Re}^2G_f(\omega)+\pi^2\rho_f^2(\omega)}\ ,\\ \mathrm{Re}\Sigma_f(\omega)&=-\frac{\mathrm{Re}G_f(\omega)}{\mathrm{Re}^2G_f(\omega)+\pi^2\rho_f^2(\omega)}+(\omega-\varepsilon_f)\ .\end{aligned} \tag{5.8}$$

Results for the real and imaginary parts of the f self-energy are shown in Fig. 31. Note that near $\omega=0$, the real part of the self-energy is extremely steep, and the imaginary part is small.

The exact self-energy satisfies the low-frequency relations in Table V.[51,52] The first two relations are satisfied remarkably well (see Fig. 31) in view of the large range of $\mathrm{Im}\Sigma_f$. The fifth relation explains the effect of a rapidly varying self-energy at low frequencies: Z^{-1} is a quasiparticle renormalization constant which becomes enormous as $T_0\to 0$. The fifth relation has been used to compute the specific-heat coefficient γ directly from the f density of states (see Sec. V C).

The fact that the Fermi liquid relations for the f self-energy are satisfied only approximately reflects a general shortcoming of the self-consistent approach in the extreme low-temperature ($T \ll T_0$) limit. Analytical calculations[53,50] have demonstrated that at $T=0$, the f density of states exhibits a small nonanalytic cusp at the Fermi surface, i.e., at $\omega=0$ (see Appendix C for a detailed discussion). Due to the nonanalyticity, the self-consistent ap-

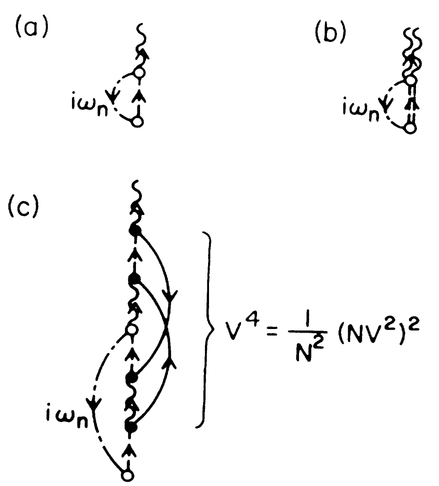

FIG. 30. Diagrammatic representation of the f electron Green's function $G_f(i\omega_n)$. As in Sec. IV, wavy lines represent the empty f orbital and dashed lines the occupied orbitals. A dash-dotted line, or "external line," carries frequency $i\omega_n$ between the points where an f electron is destroyed and created. (a) f Green's function in the absence of interactions. (b) f Green's function within the self-consistent large-degeneracy expansion. The bare configuration lines in (a) are replaced by lines dressed with the self-energies in Fig. 24. (c) An $O(1/N^2)$ diagram omitted in the self-consistent treatment. This diagram *cannot* be obtained by dressing the empty- and occupied-state lines in (b) with additional self-energy corrections, such as those in Fig. 25.

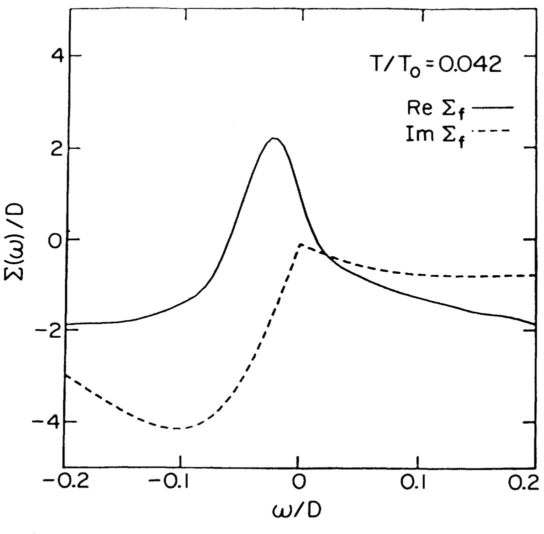

FIG. 31. Low-temperature f electron self-energy $\Sigma_f(\omega+i0^+)$ near zero frequency. The parameters are the first set in Table I. The real part of the self-energy is extremely steep near $\omega=0$. The effective density of states measured by the low-temperature specific heat is not $\rho_f(0)$, but $Z^{-1}\rho_f(0)$, where

$$Z^{-1}=\left[1-\frac{\partial}{\partial\omega}\mathrm{Re}\Sigma_f\right]\Bigg|_{\omega=0}\ .$$

The imaginary part of the self-energy has a sharp peak near $\omega=0$ with $\mathrm{Im}\Sigma_f(i0^+)/D=-0.037$. This is in excellent agreement with the exact value, -0.05. (Coulomb interactions do not alter the value of $\mathrm{Im}\Sigma_f$ at the Fermi surface, even in the limit $U\to\infty$.) The peak in $\mathrm{Im}\Sigma_f$ occurs at $\omega/D=4\times10^{-5}\ll T_0/D$. Another exact result for systems with Coulomb interactions (see Table V) is that, at zero temperature, the imaginary part of the self-energy has its smallest magnitude at the Fermi surface; in view of the large variation in $\mathrm{Im}\Sigma_f$, the position of the peak is in excellent agreement with this result.

TABLE V. Fermi-liquid relations for the degenerate orbital Anderson model. A number of simple relations connect properties of the Anderson model evaluated at zero temperature and energy. These relations may be established by perturbation theory to all orders in the Coulomb energy U. Analogous relations are obeyed in any system with Coulomb interactions. In relation 5, γ is the impurity specific-heat coefficient.

(1) $\mathrm{Im}\Sigma_f(i0^+)\Big|_{T=0}=-\Gamma$

(2) $\frac{\partial}{\partial\omega}\mathrm{Im}\Sigma_f(\omega+i0^+)\Big|_{\omega=T=0}=0$

(3) $\rho_f(0)\Big|_{T=0}=\frac{1}{\pi\Gamma}\sin^2\left[\frac{\pi n_f}{N}\right]\Bigg|_{T=0}$ (Friedel-Langreth)

(4) $\frac{\mu_J^2}{3}\frac{\mathrm{Im}\chi(\omega)}{\omega}\Bigg|_{\omega=T=0}=\frac{\pi}{N}\chi^2\Big|_{T=0}$ (Korringa-Shiba)

(5) $\gamma=\frac{\pi^2}{3}NZ^{-1}\rho_f(0),\quad Z=\left[1-\frac{\partial}{\partial\omega}\mathrm{Re}\Sigma_f(\omega)\right]^{-1}\Bigg|_{\omega=T=0}$

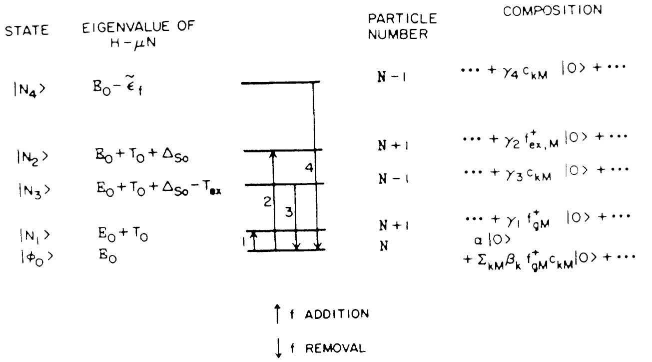

FIG. 32. Schematic level scheme for one f-electron excitations in a system with spin-orbit splitting. Eigenenergies of $H-\mu N$ are indicated on the left; particle number and the principal composition of each many-particle state are indicated on the right. E_0 is the ground-state energy and $|\phi_0\rangle$ the ground-state wave function. The ground state is separated by energy T_0 from a cluster of low-lying $(\mathcal{N}+1)$-particle states $|N_1\rangle$ with predominantly ground-multiplet f^1 character. A cluster of $(\mathcal{N}+1)$-particle states $|N_2\rangle$ with predominantly excited-multiplet f^1 character lies higher by energy $\Delta_{\text{s.o.}}$. Just below $|N_2\rangle$ lie the $(\mathcal{N}-1)$-particle states $|N_3\rangle$: these states resemble the $(\mathcal{N}-1)$-particle ground state, but with ground-multiplet electrons replaced by excited-multiplet electrons. The splitting T_{ex} reflects the energy gain from hybridization when an f^0 component is mixed into states with predominantly excited-multiplet f^1 character. Finally, the $(\mathcal{N}-1)$-particle states $|N_4\rangle$ lie above the ground state by energy $-\tilde{\epsilon}_f \sim -\epsilon_f$; these states have predominantly f^0 character.

proximation violates various Fermi liquid relations, such as those above. This shortcoming is not severe in the Kondo regime: anomalous behavior is limited to temperatures and energies of order

$$T,\omega \sim \frac{T_0}{N+1}\left[\frac{\pi T_0}{\Gamma}\right]^{(N+1)/(N-1)} . \tag{5.9}$$

This anomaly scale is small in comparison with the physically relevant scale for low-temperature properties, T_0. Results reported in this paper are limited to temperatures larger than or of order the anomaly scale: the cusp anomaly known to occur in the f density of states at zero temperature has not been observed in numerical studies down to the lowest temperatures for which convergent results are obtained. Instead, the onset of the zero-temperature anomaly is indicated indirectly by the violation of the Fermi liquid relations (see also the discussion at the end of Sec. V F).

B. *f* density of states for generalizations of the model

The preceding discussion assumes the simplest version of the degenerate Anderson model and ignores the possibility of fine structure in the f orbital due to spin-orbit and crystalline electric field (CEF) interactions. Both effects must in general be included in a physically correct picture of the f density of states. So long as the infinite-U approximation is retained, both effects may be included in a conceptually straightforward way: the impurity Hamiltonian H_f may be generalized to the form

$$H_f = \sum_{\alpha,m} \varepsilon_{f\alpha} \hat{\mathbf{N}}_{\alpha m} , \tag{5.10}$$

where now α labels distinct spin-orbit or CEF multiplets and m indexes degenerate partners within a multiplet. In an even more general context, $\varepsilon_{f\alpha}$ may be replaced by $\varepsilon_{f\alpha m}$; this generalization is necessary in the presence of a finite magnetic field. The only new feature in the treatment of these generalized Hamiltonians by the self-consistent large-degeneracy expansion is the introduction of two or more f^1 multiplets, rather than a single multiplet with degeneracy N. The coupled integral equations are the same as before, except that now a separate propagator and self-energy must be associated with each distinct sublevel.

We briefly consider the features expected in the simplest generalized model with two distinct sublevels. This model is appropriate, for example, for treating the two spin-orbit multiplets in Ce under the assumption CEF splitting is negligible. A typical spectrum is shown for this case in Figs. 32 and 33. We denote the sublevel degeneracies N_g and N_{ex}, where $\varepsilon_{fg} < \varepsilon_{f,\text{ex}}$. For the Ce model, $N_g = 6$ and $N_{\text{ex}} = 8$. The spectra ρ_{fg} and $\rho_{f,\text{ex}}$ have the following qualitative features: (1) The ground multiplet exhibits a resonance near the corresponding single particle energy ε_{fg}. This resonance reflects the large weight of the ground multiplet in the many-body ground state; the excited multiplet is essentially absent from the ground state, and negligible weight appears in its density of states at negative energies. Since an empty f level may be filled in $N = N_g + N_{\text{ex}}$ different ways, the resonance in ρ_{fg} has width $N\Gamma$. (2) Kondo resonances are expected at positive energy in each spectrum, due to admixture of f^0 weight in the interacting ground state. As in the case of a single multiplet, these resonances reflect the weight for exciting transitions between the ground state and states near ε_{fg} and $\varepsilon_{f,\text{ex}}$ with large f^1 admixtures. (3) Finally, just as f^0 weight appears in the singlet ground state below ε_{fg}, a significant f^0 admixture appears in states just below the excited multiplet. The removal of a ground-multiplet electron from the ground state may leave the system in one of these states near $\varepsilon_{f,\text{ex}}$; thus, an additional negative-energy resonance appears in ρ_{fg}.

The temperature dependence of the low-energy features is illustrated in Fig. 34. Note that the lowest peak is markedly less temperature-sensitive than the remaining two. Further, for a fixed hybridization strength, the total spectral weight at low energies is significantly increased by the presence of the upper multiplet. This observation may have important implications for the interpretation of experimental photoemission and inverse photoemission data:[54] (a) experiments typically observe low-energy weight larger than $\pi T_0 / N_g \Gamma$. (T_0 may be determined by fitting other properties, such as the magnetic susceptibility.) (b) In addition, the low-energy weight is typically far less temperature-sensitive than expected on the basis of a ngle-multiplet Kondo resonance (cf. Fig. 7). The pres-nce of additional temperature-insensitive weight in ρ_f

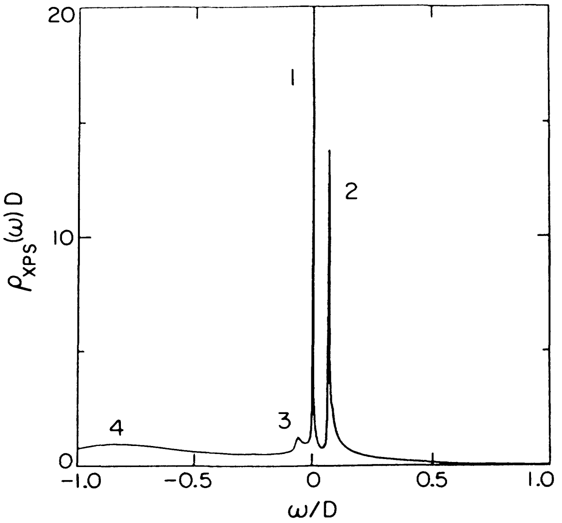

FIG. 33. $T \rightarrow 0$ f density of states $\rho_{\rm XPS}$ for a system with spin-orbit splitting. Results are shown for an f-electron system with two spin-orbit multiplets split by an energy $\Delta_{\rm s.o.}/D = 0.07$. The ground multiplet, at energy $\epsilon_{fg}/D = -0.67$, has degeneracy 6, and the excited multiplet degeneracy 8. By definition,

$$\rho_{\rm XPS} = 6\rho_{fg} + 8\rho_{f,\rm ex} \ .$$

The hybridization width is $\Gamma/D = 0.035$ for both multiplets. For $D = 3$ eV, this is a reasonable model for a Ce alloy with negligible crystalline electric field effects. The density of states for a single magnetic channel of the ground multiplet, ρ_{fg}, exhibits a broad (half-width $\sim 14\Gamma$) resonance near ϵ_{fg} and two narrow resonances near the Fermi level. These resonances are labeled by the number for the appropriate transition in Fig. 32. The parameters T_0 and $T_{\rm ex}$ may be estimated analytically using the poor-man's scaling technique. The estimates for T_0 and $T_{\rm ex}$ obtained from second-order scaling theory for a flat-band density of states are

$$T_0 \simeq D \exp\left[\frac{\pi\epsilon_{fg}}{6\Gamma}\right]\left[\frac{D}{\Delta_{\rm s.o.} + T_0}\right]^{8/6} ,$$

$$T_{\rm ex} \simeq D \exp\left[\frac{\pi\epsilon_{f,\rm ex}}{8\Gamma}\right]\left[\frac{D}{\Delta_{\rm s.o.} - T_{\rm ex}}\right]^{6/8} \ (T_{\rm ex} \ll \Delta_{\rm s.o.}) \ .$$

The single-channel density of states for the excited multiplet, $\rho_{f,\rm ex}$, exhibits only a single prominent resonance at positive energy. The resonance is labeled by the corresponding number from Fig. 32. The widths of resonances 1–4 may be estimated as $\pi T_0/6$, $\pi T_{\rm ex}/8$, $\pi T_0/6$, and 14Γ.

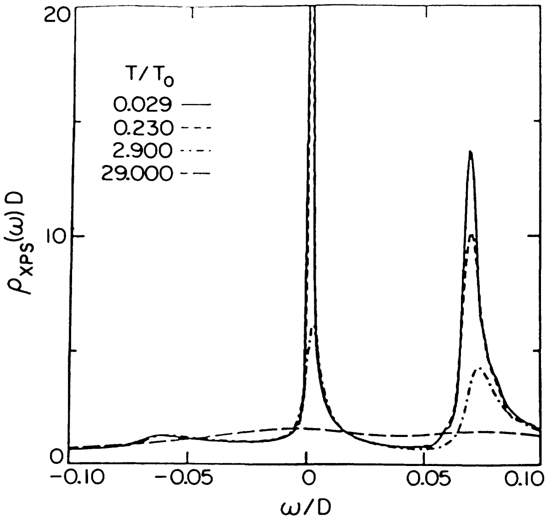

FIG. 34. Temperature dependence of the f density of states with spin-orbit splitting. The parameters are the same as those employed in Fig. 33. The positive-energy resonances are depleted as the temperature increases through the low-energy scale T_0. The negative-energy resonance is not so strongly temperature dependent: it is depleted with characteristic temperature $\Delta_{\rm s.o.} \gg T_0$. This difference in behavior has a simple explanation: the lower resonance measures the weight for transition 3 in Fig. 32. The $\mathcal{N}$-particle states just above the ground state have predominantly ground-multiplet character, just as the ground state does; hence, the thermal occupation of these states at temperatures of order T_0 does not significantly alter the probability for $f^1 \rightarrow f^0$ transitions with energies larger than T_0 (such as transition 3). The situation is completely different for $f^0 \rightarrow f^1$ transitions, since low-lying excited states have negligible f^0 admixture, while the ground state has an admixture of $O(\pi T_0/N\Gamma)$.

from spin-orbit and CEF structure may help resolve both discrepancies between experiment and the simplest version of the theory. It is straightforward to calculate the static and dynamic properties of systems with spin-orbit splitting. Results for parameter sets 6 and 7 in Table I have been reported elsewhere.[55]

C. Impurity valence

The exact f-orbital occupancy, or valence, is given by

$$n_f(T) = \sum_m \langle \hat{N}_m \rangle = \sum_m \langle F_m^\dagger F_m \rangle = N G_f(\tau = 0^-) \ . \qquad (5.11)$$

General approximations need not yield consistent results for the thermodynamic derivative $\langle \hat{N}_m \rangle$ and the equal-time limit of the dynamic correlation function G_f. The self-consistent large-degeneracy expansion does yield consistent results for these two quantities (see Appendix B). Thus,

$$\begin{aligned} n_f(T) &= N\frac{1}{\beta}\sum_n e^{i\omega_n 0^+} G_f(i\omega_n) \\ &= N\int_{-\infty}^{\infty} d\varepsilon\, f(\varepsilon)\rho_f(\varepsilon) \ . \end{aligned} \qquad (5.12)$$

The valence is related to the f density of states exactly as in a one-body system.

The number of holes $n_h(T)$ in the f orbital is simply

$$n_h = \sum_m n_{hm} \equiv N - n_f \ . \qquad (5.13)$$

The number of holes cannot be obtained as $\sum_m \langle F_m F_m^\dagger \rangle$, since

$$\begin{aligned}\sum_m \langle F_m F_m^\dagger \rangle &= N\int_{-\infty}^{\infty} d\varepsilon[1-f(\varepsilon)]\rho_f(\varepsilon)\\ &= N\frac{1}{Z_f}\int_{-\infty}^{\infty} d\varepsilon\, e^{-\beta\varepsilon}\rho_0(\varepsilon) = N(1-n_f)\,.\end{aligned} \tag{5.14}$$

This expression does not account for the f weight concentrated at energies of order U: this weight is removed from the calculated density of states by the initial assumption $U \rightarrow \infty$. To obtain the correct answer, it must be noted before imposing the infinite-U limit that $n_{hm}(T) = 1 - n_{fm}(T)$; this follows formally from the anticommutation relations of the physical f electrons. The result (5.13) for $n_h(T)$ is then immediate.

D. Specific heat

In general, the impurity specific heat is not simply related to the f density of states (see the discussion in Sec. III). However, in the zero-temperature limit, $C=\gamma T$ may be computed using a Fermi liquid relation for the degenerate Anderson model:[52]

$$\begin{aligned}\gamma &= \frac{\pi^2}{3}N\rho_f(0)Z^{-1}\\ Z^{-1} &= 1-\frac{\partial}{\partial\omega}\mathrm{Re}\Sigma_f(\omega)\Big|_{\omega=0}\end{aligned} \tag{5.15}$$

(cf. the discussion in Sec. V A). Values for γ obtained in this way are collected in Table VII, where they are compared with the low-temperature susceptibility (see the discussion in Sec. V G). At finite temperatures, the impurity specific heat may be computed directly from the partition function. Recall that

$$Z = Z_{\mathrm{band}} Z_f\,, \tag{5.16}$$

where Z and Z_{band} are the partition functions for the interacting system and the noninteracting conduction band. Thus, the impurity specific heat

$$\begin{aligned}C_{\mathrm{imp}}(T) &= C(T) - C_{\mathrm{band}}(T)\\ &= -T\frac{\partial^2}{\partial T^2}[F(T)-F_{\mathrm{band}}(T)]\\ &= T\frac{\partial^2}{\partial T^2}T\ln Z_f(T)\,.\end{aligned} \tag{5.17}$$

Here, C (C_{band}) and F (F_{band}) are the specific heat and free energy of the interacting system (noninteracting conduction band). An equivalent form more convenient for numerical work is

$$C_{\mathrm{imp}}(T) = \left[\frac{\partial^2}{\partial(\ln\beta)^2}-\frac{\partial}{\partial\ln\beta}\right]\ln Z_f(T)\,, \tag{5.18}$$

with $\beta = 1/T$.

The scaling behavior of the specific heat was illustrated in Sec. III. As an equilibrium property, the specific heat may be computed by the Bethe *ansatz*.[30,31] The Bethe *ansatz* requires a linear band dispersion. Nevertheless, since low-temperature properties assume a universal form, Bethe *ansatz* results may be compared directly with the results of the large-degeneracy expansion for a Lorentzian band. The extent of agreement is a measure of the accuracy of the large-degeneracy expansion.

Large-degeneracy results for systems with zero-temperature valence $n_f = 0.97$ are compared in Figs. 35 and 36 with Bethe-*ansatz* results[30] for systems with $n_f = 1$. (The Bethe-*ansatz* curves actually describe the Coqblin-Schrieffer model: this model is related by a rigorous mapping to the infinite-U Anderson model in the limit $\varepsilon_f \rightarrow -\infty$, $V^2/\varepsilon_f = \mathrm{const}$. The Bethe-*ansatz* results for the Coqblin-Schrieffer model[30] and for the Anderson model[31] with zero-temperature valence 0.97 are essentially indistinguishable over the temperature range in Figs. 35 and 36.) In order to compare the results, the low-temperature scales in the two approaches must be related; the ratio of these scales may in principle be computed analytically by studying *high*-temperature expansions for the two models. The ratio of high-temperature scales found by this method must be the same as the ratio of low-temperature scales, by a universality argument. To date, this analytic matching procedure has been carried out only in systems with a flat band density of states. Since we have employed a Lorentzian density of states in the present numerical study, we treat the ratio of Kondo scales as a fitting parameter in the comparison. This procedure is satisfactory, since results for a second property, the magnetic susceptibility, may be compared assuming the same scale ratio (see Sec. V G).

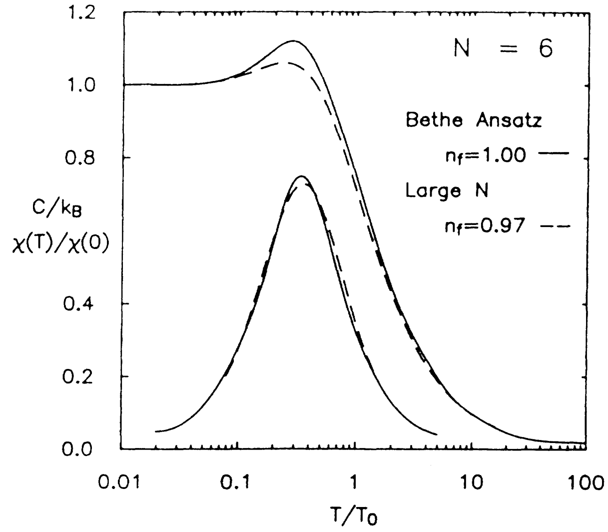

FIG. 35. Comparison of large-degeneracy expansion and Bethe-*ansatz* results for $N=6$: specific heat and susceptibility. The large-degeneracy results correspond to the first parameter set in Table I. The Bethe-*ansatz* results for the Coqblin-Schrieffer model (Ref. 30) (the integral-valent limit of the infinite-U Anderson model) are shown for comparison. Since the conduction band densities of states and the momentum-cutoff schemes differ in these two approaches, the low-temperature scales are not trivially related. The Bethe-*ansatz* temperature scale has been adjusted to match the two susceptibility curves at high temperature; the excellent agreement of the specific heat and low-temperature susceptibility in the two approaches confirms the validity of the large-degeneracy approximation scheme.

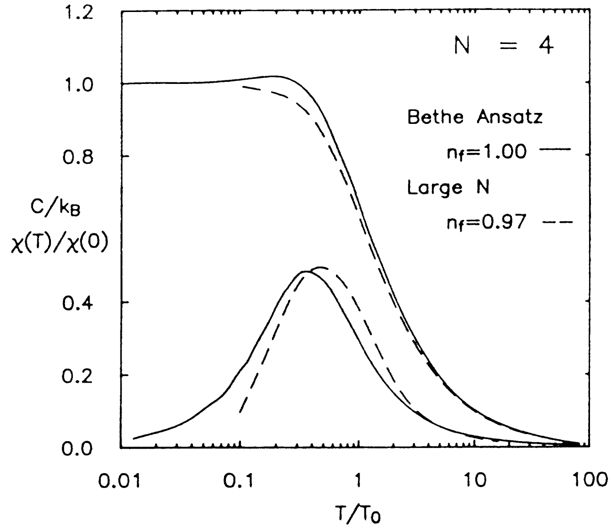

FIG. 36. Comparison of large-degeneracy expansion and Bethe-*ansatz* results for $N=4$: specific heat and susceptibility. The large-degeneracy expansion is not sufficiently accurate to produce a finite-temperature peak in the susceptibility; the smallest degeneracy for which such a peak appears in Bethe-*ansatz* results is 4.

The comparison is simplest on a logarithmic temperature plot: in this case, the scale ratio may be varied by sliding the curves along the temperature axis without distortion. The agreement between the large-degeneracy and Bethe-*ansatz* results is excellent. This substantiates the approximation at finite temperatures, directly for equilibrium properties and indirectly for dynamic properties as well.

E. Transport properties

In the linear response regime, the resistivity ρ, thermopower S, and thermal conductivity κ are simply related to the f density of states: this is because conduction electrons scatter by hopping in and out of impurity orbitals. As shown in Appendix D, all three properties may be expressed in terms of standard transport integrals:

$$\rho=\frac{1}{e^2L_0}\ ,$$

$$S=-\frac{1}{eT}\frac{L_1}{L_0}\ , \tag{5.19}$$

$$\kappa=\frac{1}{T}\left[L_2-\frac{L_1^2}{L_0}\right] .$$

where

$$L_n(T)=\frac{2}{3m^2}\int d\mathbf{k}\frac{\mathcal{V}}{(2\pi)^3}\left[-\frac{\partial f}{\partial \varepsilon_k}\right]\mathbf{k}^2(\varepsilon_k-\mu)^n\tau(\varepsilon_k)$$
$$\simeq\frac{2[N(0)]^2k_F^2}{3m^2C}\int_{-\infty}^{\infty}d\varepsilon\left[-\frac{\partial f}{\partial\varepsilon}\right]$$
$$\times\varepsilon^n[N(0)\tau^{-1}(\varepsilon)/C]^{-1}\ ; \tag{5.20}$$

here C, is the dimensionless impurity concentration (the number of impurities per unit cell), and the scattering rate per unit impurity concentration is

$$N(0)\tau^{-1}(\varepsilon)/C=N\Gamma\rho_f(\varepsilon)\ . \tag{5.21}$$

Since the scattering rate $\tau^{-1}(\varepsilon)$ assumes an approximate scaling form, all three transport properties have universal characteristics at low temperatures: the appropriate scaling functions are $\rho/\rho(0)$, S and $\kappa/\kappa(0)$. Note that the resistivity and thermal conductivity must be divided by their zero-temperature values to eliminate material-dependent parameters.

As shown in Fig. 15, the resistivity displays scaling over a temperature range of several decades for valences larger than 0.7. The thermopower, thermal conductivity and Lorentz ratio $\kappa\rho/T$ exhibit deviations from scaling at relatively low temperatures, since they measure higher energy moments of the conduction electron lifetime than the resistivity. Recall that only the Kondo resonance in the scattering rate has a universal form; scattering at high energies is dependent on the details of the band density of states, the position of the f orbital and the strength of the f-conduction electron coupling.

The sign change in the thermopower at high temperatures is due to a competition between the broad scattering resonance near ε_f and the Kondo resonance: the dominant contribution to transport properties at temperature T is made by electrons and holes in an energy range of order T at the Fermi surface. If, in this range, energy is transported predominantly by holes (i.e., electrons are scattered more strongly), the thermopower is positive; if energy is transported predominantly by electrons (i.e., holes are scattered more strongly), the thermopower is negative. (The sign difference arises since electrons and holes are positive energy excitations which carry opposite charges.) At low temperatures, the thermopower is positive (electrons are scattered strongly by the Kondo resonance). As T increases, hole scattering becomes more important; eventually, the same amount of energy is transported by electrons and holes, and the thermopower vanishes. At higher temperatures, energy is transported predominantly by electrons, and the thermopower is negative (as in a free-electron metal). As discussed in Sec. III, the peak thermopower in Kondo systems is one to two orders of magnitude larger than the thermopower in conventional metals.[56] This is due to the enormous disparity in electron and hole lifetimes at low temperatures. Since the Kondo contribution to $S(T)$ is so large, its calculation is not subject to the notorious difficulties which plague most theories of the thermopower.

TABLE VI. Diagrammatic rules for evaluating $M_f(i\nu_m)$. We list below rules for evaluating the moment-moment correlation function $M_f(i\nu_m)$.

To compute a general contribution to $M_f(i\nu_m)$ of $O(V^{2n})$ $n \geq 0$:

(a) Set down $2n+1$ vertices (solid dots) in a vertical line. Beginning at the bottom with a dashed line, connect the vertices with alternating dashed and wavy lines (all ascending), finally leaving the top vertex on a dashed line. (A total of $2n+1$ lines now appear.)

(b) Convert the bottom vertex to an open circle (to represent the operator $m'F_{m'}^{\dagger}F_{m'}$). Break one of the dashed lines by inserting a second open circle (to represent the operator $mF_m^{\dagger}F_m$).

(c) Always working to the right of the vertical line, connect the remaining $2n$ vertices with full lines in all possible ways which maintain the direction of the dashed line at each vertex.

(d) Working on the left of the diagram, connect the open circles with a dash-dotted "external line," carrying energy $i\nu_m$ from top to bottom.

(e) Assign quantum numbers km (m) to solid lines (dashed lines), conserving angular momentum at each vertex.

(f) Assign to ascending band lines a factor $1-f_{km}$ and to descending band lines a factor f_{km}, with f the Fermi function.

(g) Draw a perpendicular to each local configuration line, and assign to it an energy denominator $(z-E_\alpha)^{-1}$, where E_α is found by adding the energies of ascending lines intersected by the perpendicular and subtracting the energies of descending lines intersected.

(h) Multiply the product of energy denominators and Fermi factors by $V^{2n}(-)^c(g\mu_B)^2mm'$, where m and m' are the angular momentum attached to the open circles, and c is the number of conduction line crossings. Sum on conduction momenta and angular momenta (including m and m').

(i) Compute the contour integral

$$\frac{1}{Z_f}\int_\Gamma \frac{dz}{2\pi i}e^{-\beta z}R(z) ,$$

where R is the result of the preceding operations, Z_f is the system partion function, and Γ encircles all singularities of R in a counterclockwise fashion.

F. f moment spectrum

The moment spectrum σ_f plays the same central role in magnetic phenomena that the f density of states ρ_f plays in transport properties. The moment spectrum is defined as the spectral density of the f moment correlation function

$$M_f(t) = -i\Theta(t)\langle[\hat{M}(t),\hat{M}(0)]\rangle ,$$
$$\sigma_f(\omega) = -\frac{1}{\pi}\mathrm{Im}M_f(\omega+i0^+) , \qquad (5.22)$$

where $\hat{M}=g\mu_B\sum_m m\hat{N}_m$. The moment spectrum may be evaluated by computing the Matsubara correlation function

$$M_f(i\nu_m)=\int_0^\beta d\tau\, e^{i\nu_m\tau}[-\langle T_\tau\hat{M}(\tau)\hat{M}(0)\rangle] , \qquad (5.23)$$

then performing the analytic continuation to real frequencies. General rules for evaluating $M_f(i\nu_m)$ appear in Table VI. The lowest order contribution [see Fig. 37(a)] is simply

$$\frac{1}{Z_f^0}\sum_m m^2\int\frac{dz}{2\pi i}e^{-\beta z}\frac{1}{z+i\nu_m-\epsilon_f}\,\frac{1}{z-\epsilon_f}$$
$$=-\frac{Ne^{-\beta\epsilon_f}}{Z_f^0}\frac{\mu_j^2}{3T}\delta_{m0} , \qquad (5.24)$$

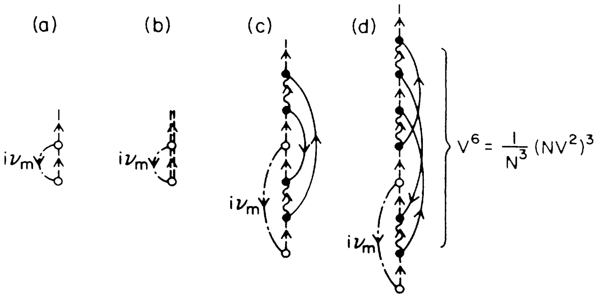

FIG. 37. Diagrammatic representation of the f moment correlation function. As before, wavy lines represent the empty impurity orbital, dashed lines the occupied orbital, and solid lines the conduction electrons. Open circles represent the f-moment operator. A dash-dotted "external line" carries frequency $i\nu_m$ between the open circles. (a) Correlation function in the absence of hybridization. (b) Correlation function in the self-consistent large-degeneracy expansion. The double dashed lines incorporate the self-energy in Fig. 24. (c) Vertex correction with noncrossing conduction lines. This contribution vanishes when the sum over magnetic quantum numbers m and m' associated with the two moment operators is performed. (d) Vertex correction with crossing conduction lines. This diagram, which cannot be obtained by dressing the empty- and occupied-state lines with self-energy insertions, remains after the sum on magnetic quantum numbers. Relative to the contribution in (b), it is $O(1/N^2)$.

with

$$\mu_j^2 \equiv j(j+1)(g\mu_B)^2 \; ,$$
$$Z_f^0 = 1 + Ne^{-\beta\varepsilon_f} \; .$$

The occupied state lines in Fig. 37(a) may be dressed to give

$$\begin{aligned} M_f(i\nu_m) &\simeq \frac{N\mu_j^2}{3}\frac{1}{Z_f}\int \frac{dz}{2\pi i} e^{-\beta z} G_m(z+i\nu_m)G_m(z) \\ &= \frac{N\mu_j^2}{3}\frac{1}{Z_f}\int_{-\infty}^{\infty} d\varepsilon\, e^{-\beta\varepsilon}\rho_m(\varepsilon) \\ &\quad \times [G_m(\varepsilon+i\nu_m)+G_m(\varepsilon-i\nu_m)] \; . \end{aligned} \tag{5.25}$$

Additional diagrammatic contributions, such as those in Figs. 37(c) and 37(d), involve vertex corrections. Diagrams which may be broken into disconnected parts by cutting two empty-state lines [such as Fig. 37(c)] drop out when sums over the quantum numbers m and m' are performed. The remaining diagrams are smaller than the leading contributions by $O(1/N^3)$. Thus, the expression in Eq. (5.25) is the complete result for $M_f(i\nu_m)$ within the self-consistent expansion. The f moment spectrum becomes

$$\begin{aligned} \sigma_f(\omega) &= \frac{N\mu_j^2}{3}\frac{1}{Z_f}\int_{-\infty}^{\infty} d\varepsilon\, e^{-\beta\varepsilon}\rho_m(\varepsilon) \\ &\quad \times [\rho_m(\varepsilon+\omega)-\rho_m(\varepsilon-\omega)] \; . \end{aligned} \tag{5.26}$$

Note that this spectrum is odd in ω. The dominant features in the zero-temperature moment spectrum are resonances at energy $\sim \pm T_0$. These resonances indicate that the system has high probability for gaining or losing energy T_0 in interactions with an external magnetic probe (such as a neutron). In other words, a set of many-particle eigenstates with an intrinsic magnetic moment is centered at energy T_0 above the ground state; these are the same states containing a large f^1 admixture which contribute to the Kondo resonance in the f density of states. For this reason, the energy scale for transport and magnetic phenomena is the same. The actual spectrum measured in neutron scattering is $(1-e^{-\beta\omega})^{-1}\sigma_f(\omega)$. The temperature-dependent factor reflects the fact that at low temperatures only the positive-energy moment spectrum (corresponding to neutron energy loss) is measurable.

The inadequacy of the self-consistent large-degeneracy expansion at zero temperature[53,50] (cf. the discussion for the f density of states in Sec. V A) is reflected in the f moment spectrum as well (see Appendix C). The breakdown of the approach at low temperature and energy is most clearly exhibited by plotting $\sigma_f(\omega)/\omega$. At zero temperature, this quantity obeys a Fermi liquid relation first proved by Shiba:[57]

$$\lim_{\omega\to 0}\frac{\mu_j^2}{3}\frac{\sigma_f(\omega)}{\omega\chi^2} = \frac{1}{N} \; ,$$
$$\mu_j^2 = j(j+1)(g\mu_B)^2 \; . \tag{5.27}$$

As shown by Müller-Hartmann[53] and Kuramoto and Kojima,[50] $\sigma_f(\omega)/\omega$ actually diverges as $|\omega|^{-2(N+1)}$ within the large-degeneracy expansion. This nonanalytic low-energy behavior is illustrated in Fig. 38. At higher temperatures, the low-energy cusp rapidly disappears and the expansion becomes reliable.

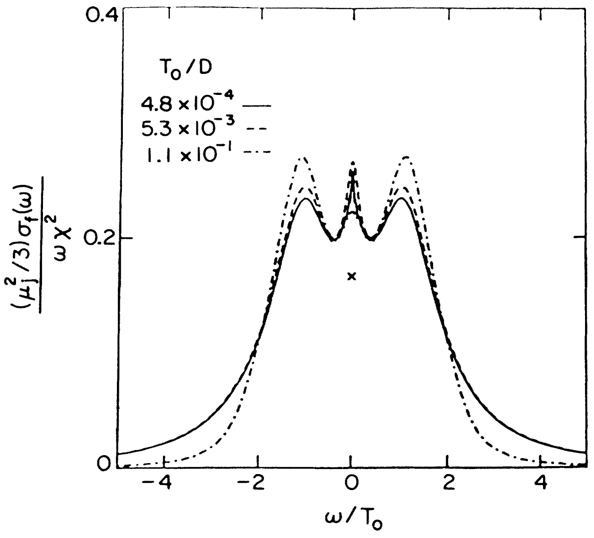

FIG. 38. Behavior of $\sigma_f(\omega)/\omega$ in the low-temperature limit. For $T\to 0$, the calculated f moment spectrum exhibits a spurious low-energy cusp associated with the incipient breakdown of the self-consistent large-degeneracy expansion. Results for parameter sets 1, 3, and 5 in Table I are shown above. The exact behavior at zero temperature and energy (indicated by ×) follows from a Fermi-liquid relation:

$$\lim_{\omega\to 0}\frac{\mu_j^2}{3}\frac{\sigma_f(\omega)}{\omega\chi^2} = \frac{1}{N} \; .$$

G. Magnetic susceptibility

The moment spectrum discussed in Sec. V F is closely related to the absorptive part of the magnetic susceptibility. In the linear response regime, the system's total susceptibility is

$$\chi(\omega) = \int_{-\infty}^{\infty} dt\, e^{i(\omega+i0^+)t}\mathcal{M}(t) \; , \tag{5.28}$$

with

$$\mathcal{M}(t) = +i\Theta(t)\langle[\hat{\mathcal{M}}(t),\hat{\mathcal{M}}(0)]\rangle$$

and

$$\hat{\mathcal{M}} = g_c\mu_B\sum_{\mathbf{k},\sigma}\sigma c_{\mathbf{k}\sigma}^{\dagger}c_{\mathbf{k}\sigma} + g\mu_B\sum_m m\hat{N}_m \; . \tag{5.29}$$

In general (see Appendix E), $\mathcal{M}(t)$ separates into terms measuring the self-correlation of the conduction-band magnetization, the self-correlation of the f magnetization, and the mutual correlation of f and band components. In the dilute impurity limit, the first term produces the Pauli susceptibility of the band electrons (slightly modified since electrons near the Fermi surface have a finite lifetime in the presence of impurities). The second term is the most interesting: its contribution to $\chi(T)$ reflects the quenching of the effective impurity moment, showing a crossover from Curie behavior at high temperatures to Pauli behavior at low temperatures. The remaining term in $\mathcal{M}(t)$ contains band-f polarization effects. This term is nonzero in general; however, it may be argued that its contribution to the susceptibility is small in large bandwidth systems (see Appendix E). We discuss only the dominant contribution to $\chi(T)$ below. Ignoring polarization effects, the impurity susceptibility is

$$\begin{aligned}\chi(\omega+i0^+)&=-M_f(\omega+i0^+)\\&=\mathrm{P}\int_{-\infty}^{\infty} d\varepsilon\frac{\sigma_f(\varepsilon)}{\varepsilon-\omega}+i\pi\sigma_f(\omega)\,,\end{aligned}\tag{5.30}$$

where P denotes a principal value. In particular, the static susceptibility is just

$$\begin{aligned}\chi(\omega=0)&=\mathrm{P}\int_{-\infty}^{\infty} d\varepsilon\frac{\sigma_f(\varepsilon)}{\varepsilon}\\&=-\frac{N\mu_j^2}{3}\frac{1}{Z_f}\int_{-\infty}^{\infty} d\varepsilon\, e^{-\beta\varepsilon}2\,\mathrm{Re}G_m(\varepsilon)\rho_m(\varepsilon)\,.\end{aligned}\tag{5.31}$$

The static susceptibility may also be obtained directly from the partition function Z_f as a thermodynamic derivative. It may be checked that the same result is obtained by both approaches. Since the moment spectrum obeys approximate scaling at low temperatures and frequencies, the static susceptibility also assumes a universal form (see Figs. 19 and 20). The susceptibility calculated within this approach is in good agreement with the exact result obtained by the Bethe *ansatz*[30] (see Figs. 35 and 36).

Values for the susceptibility in the zero-temperature limit are presented in Table VII. Note that the susceptibility and specific heat coefficient are of the same order of magnitude. For a Fermi gas, the Sommerfeld ratio[56]

$$R\equiv\frac{\pi^2/3}{\mu_j^2/3}\frac{\chi}{\gamma}\tag{5.32}$$

is unity; deviations from unity measure the strength of magnetic interactions in a Fermi liquid. From the table, the Sommerfeld ratio for the systems in the integral valent limit ($n_f\sim1$) is approximately $\frac{6}{5}$, i.e., $N/(N-1)$ for $N=6$. By comparison, the exact value, which follows from a Fermi liquid relation,[52] is

$$R=\frac{N}{N-1}\left[1-\frac{1}{N}\frac{\pi^2}{3}\frac{\chi_c}{\gamma}\right];\tag{5.33}$$

the charge susceptibility χ_c vanishes in the integral valent limit and increases slowly with decreasing valence. The results from the self-consistent approach are in good agreement with this exact relation.

TABLE VII. Results for normal-state properties in the Fermi-liquid regime ($T\rightarrow0$). The zero-temperature valence, magnetic susceptibility and specific heat coefficient for the parameter sets of Table I are listed below. All properties are computed by extrapolation from finite temperature ($0.02T_0$–$0.05T_0$) to avoid the difficulties known to occur in the self-consistent approach at zero temperature. The specific-heat coefficient is computed using the fifth Fermi-liquid relation in Table V. The susceptibility and specific heat coefficient are scaled by the single-channel density of states per unit cell at the Fermi surface for *conduction* electrons:

$$\tilde{\chi}=\frac{\chi}{\mu_j^2/3}\frac{1}{(\pi D)^{-1}},\quad \tilde{\gamma}=\frac{\gamma}{\pi^2/3}\frac{1}{(\pi D)^{-1}}\,.$$

Values of order unity would be expected in nonmagnetic alloys. In this case, $\tilde{\chi}$ and $\tilde{\gamma}$ are inversely proportional to T_0: the exact proportionality constant depends on the choice of a Lorentzian band, since $|\epsilon_f|\sim D$. By a Fermi-liquid relation, the exact Sommerfeld ratio is

$$\frac{\tilde{\chi}}{\tilde{\gamma}}=R=\frac{N}{N-1}\left[1-\frac{1}{N}\frac{\pi^2}{3}\frac{\chi_c}{\gamma}\right],$$

with χ_c the charge susceptibility (which vanishes in the Kondo limit $|\epsilon_f|\gg N\Gamma$). The results below are in good agreement with this exact relation for $N=6$ ($R\sim1.2$).

Parameter set	T_0/D	n_f	$\tilde{\chi}$	$\tilde{\gamma}$	R
1	4.8×10^{-4}	0.97	5970	4980	1.20
3	5.3×10^{-3}	0.92	537	452	1.19
4	1.8×10^{-2}	0.87	161	135	1.20
5	1.1×10^{-1}	0.71	24	20	1.18
6	8.7×10^{-4}	0.97	3220	2730	1.18
7	1.5×10^{-2}	0.86	181	162	1.12
8	2.9×10^{-3}	0.85	958	799	1.20

VI. COMPARISON WITH EXPERIMENT

In this section, we compare the results of the self-consistent large-degeneracy expansion with experiments on Ce compounds. While the experimental results hold strictly only in the dilute limit, it is of interest to compare with experimental measurements in concentrated systems as well. As shown below, a single-impurity theory offers a surprisingly good description of properties which depend weakly on wave function coherence in a periodic lattice. These properties include the photoemission spectrum, the static and dynamic susceptibility and the specific heat.

The dilute Ce alloy most thoroughly studied by experimentalists[58–60] is $(La,\mathrm{Ce})\mathrm{B}_6$. Impurity interaction effects in this system are believed to be largely absent for Ce concentrations less than about 2%. This alloy exhibits Kondo anomalies in the 1-K range. A small Kondo scale is important for reliable comparisons with theory: in the 1-K range, phonon contributions to the specific heat and transport properties are small, and magnetic impurity effects may be separated out by performing background subtractions. (Deviations from Matthiessen's rule are known to be important when phonon and magnetic contributions to transport properties are comparable.[61]) Another convenient feature of $(La,\mathrm{Ce})\mathrm{B}_6$ is the absence of a superconducting transition down to the millikelvin range; this allows normal-state measurements over several decades of temperature. Measured properties include the static susceptibility,[59] specific heat,[60] resistivity,[58] and thermopower.[60]

Large cubic crystal fields in the LaB_6 matrix lower the ground-state degeneracy from six to four. The existence of a quartet-doublet level scheme with splitting ~ 600 K has been confirmed by inelastic neutron and Raman scattering.[62] In addition, evidence exists for a fine-scale (~ 30 K) splitting of the quartet ground state, presumably by a dynamic crystal-field-phonon interaction. (A symmetry-lowering process must be postulated, since cubic crystal fields break a sextet into a doublet and quartet, rather than three doublets.) So long as the hybridization width Γ is larger than the quartet splitting, the ground state degeneracy remains effectively four.

Assuming $N=4$, we have computed $\chi(T)$, $C(T)$, $\rho(T)$, and $S(T)$ within the self-consistent large-degeneracy expansion. The parameters chosen (see Table VIII) provide results in the scaling regime. Experiment and theory for all four properties may be compared by fitting a single parameter, the Kondo scale T_0; this provides a relatively stringent test of the theory. The results of the fit for $T_0=1$ K are shown in Figs. 39–42. The experimental curves show only the magnetic contribution to each property. The approximations made in arriving at this contribution are the following.

(1) For the susceptibility, specific heat, and resistivity, a simple background subtraction based on pure LaB_6 has been applied. The subtraction is most problematic for the resistivity, since Matthiessen's rule[56] (additivity of scattering rates) is assumed. Even in this case, the subtraction is reasonably justified since the phonon and nonmagnetic impurity contributions to $\rho(T)$ are much smaller than the magnetic contribution.

TABLE VIII. Parameters for comparison with $(La,\mathrm{Ce})\mathrm{B}_6$. A Lorentzian conduction band of half-width D with center at the Fermi level was assumed. The degeneracy $N=4$ is appropriate for a Ce ion with a Γ_8 crystal-field ground state. The parameters lie within the scaling regime: all static properties may be expressed as universal functions of the reduced temperature T/T_0. The susceptibility and specific-heat coefficient are scaled by the single-channel density of states per unit cell at the Fermi surface for *conduction* electrons, $(\pi D)^{-1}$:

$$\tilde{\chi}=\frac{\chi}{\mu_j^2/3}\,\frac{1}{(\pi D)^{-1}},\quad \tilde{\gamma}=\frac{\gamma}{\pi^2/3}\,\frac{1}{(\pi D)^{-1}}\ .$$

Note that the Sommerfeld ratio is in this case $\sim N/(N-1)=\frac{4}{3}$. The value of T_0 assumed for $(La,\mathrm{Ce})\mathrm{B}_6$ is 1 K.

Parameter	Value
N	4
ε/D	-0.67
Γ/D	0.075
T_0/D	3.5×10^{-4}
n_f	0.96
$\tilde{\chi}$	7710
$\tilde{\gamma}$	5830
$\tilde{\chi}/\tilde{\gamma}$	1.32

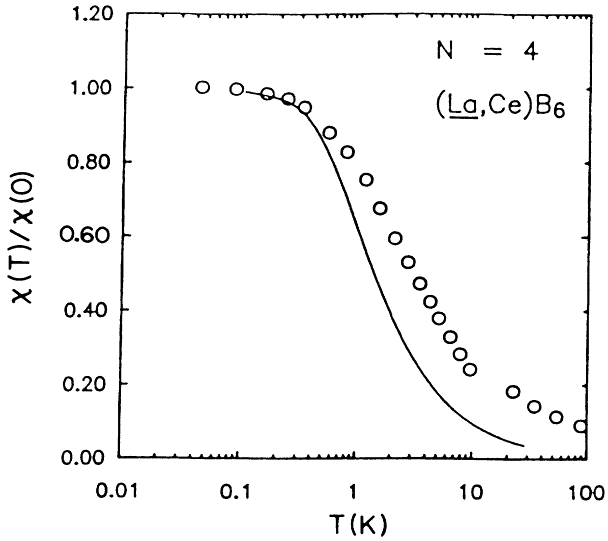

FIG. 39. Comparison of theory and experiment for $(La,\mathrm{Ce})\mathrm{B}_6$: magnetic susceptibility. In Figs. 39–42, the experimentally determined contribution to each property is denoted by open circles. The solid lines are the results of the self-consistent large-degeneracy expansion: the same value of the theoretical low-energy scale, $T_0=1$ K, has been assumed for each property. A Γ_8 quartet ground state is assumed. The magnetic susceptibility shows the largest discrepancy between theory and experiment. The disagreement may be of experimental origin: in the study cited (Ref. 59), a doublet ionic ground state was deduced from the high-temperature moment. Subsequent high-temperature susceptibility measurements, as well as neutron studies, have confirmed that the ground state is a quartet.

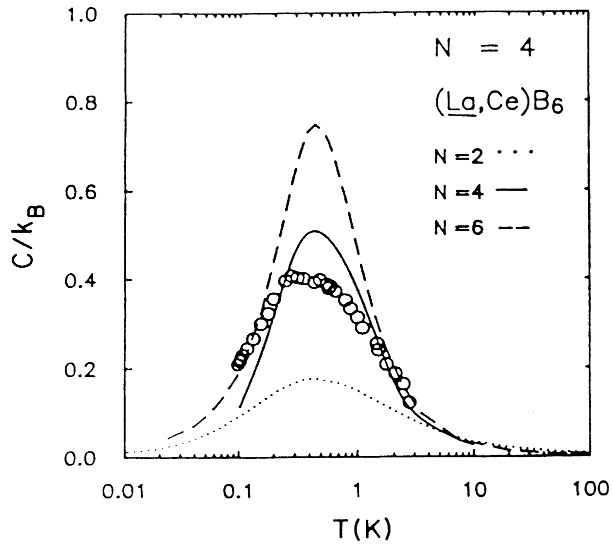

FIG. 40. Comparison of theory and experiment for $(La,\mathrm{Ce})\mathrm{B}_6$: specific heat. The experimental specific heat is compared with the large-degeneracy result for $N=4$ and Bethe-*ansatz* results for $N=2$ and 6. The experimental peak is slightly broader and lower than the $N=4$ theory curve; however, it clearly cannot be described by the curves for $N=2$ or 6.

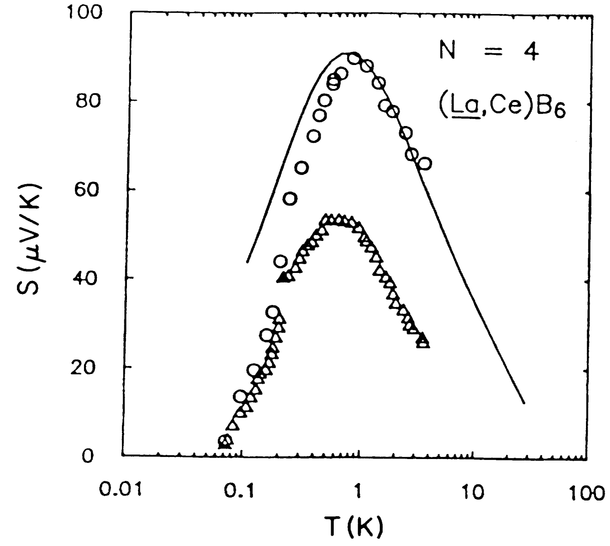

FIG. 42. Comparison of theory and experiment for $(La,\mathrm{Ce})\mathrm{B}_6$: thermopower. The raw experimental thermopower for a sample with 0.25% Ce impurities is denoted by triangles. The magnetic thermopower deduced from the Nordheim-Gorter rule is denoted by open circles. The peak magnetic thermopower in theory and experiment is of order 90 μV/K.

(2) The Nordheim-Gorter rule[63] is assumed in extracting the magnetic impurity thermopower. This rule states that the contribution of each scattering mechanism to the thermopower is weighted by that mechanism's contribution to the thermal resistivity, i.e.,

$$S(T)=\frac{\sum_i S_i(T)\kappa_i^{-1}(T)}{\sum_i \kappa_i^{-1}(T)}, \tag{6.1}$$

where S_i and κ_i are the thermopower and thermal conductivity due to mechanism i. In cases where the $\kappa_i(T)$ are not well determined experimentally (such as the present case), the thermal resistivity is conveniently replaced by the electrical resistivity, i.e.,

$$S(T)\simeq\frac{\sum_i S_i(T)\rho_i(T)}{\sum_i \rho_i(T)}. \tag{6.2}$$

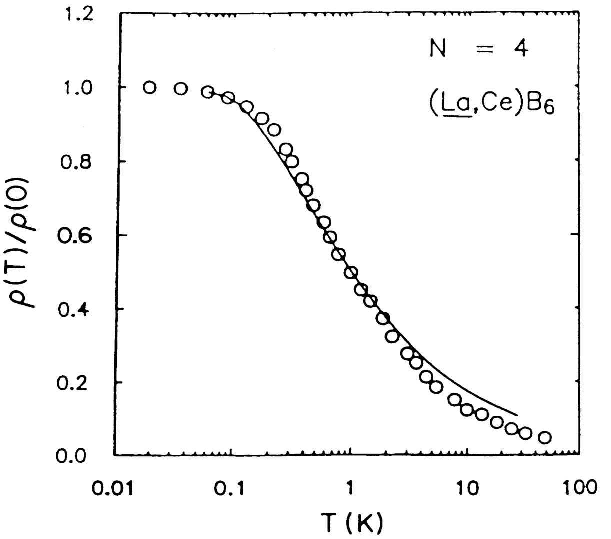

FIG. 41. Comparison of theory and experiment for $(La,\mathrm{Ce})\mathrm{B}_6$: electrical resistivity. The experimental resistivity is reasonably well described by theory over a temperature range of nearly four decades.

The Nordheim-Gorter rule is valid provided the scattering mechanisms for particle (and energy) transport act independently (or at least that interference terms be small). The magnetic thermopower in this case takes the form

$$S_{\mathrm{mag}}(T)=[S(T)\rho(T)-S_{nm}(T)\rho_{nm}(T)]/\rho_{\mathrm{mag}}(T), \tag{6.3}$$

where S and ρ (S_{nm} and ρ_{nm}) are experimentally determined for the Ce impurity system (the "pure" system, containing only nonmagnetic impurities), and $\rho_{\mathrm{mag}}=\rho-\rho_{nm}$. The correction is small at low temperatures (where the resistivity is almost entirely magnetic) and increases with temperature (as ρ_{mag} decreases). While the peak value we have determined for the magnetic thermopower depends on the validity of the Nordheim-Gorter rule, the quality of the overall fit would not be significantly altered if the subtraction could be performed more rigorously.

The agreement between theory and experiment is reasonable for all four properties. The relatively poor susceptibility fit may be at least partially due to experimental error: high-temperature data from the same experiment[59] led to an erroneous identification of the Ce ground state as a doublet, rather than a quartet. More recent measurements of the high-temperature susceptibility[64] have confirmed the existence of a quartet ground state. Additional measurements in the 1-K range might improve the fit in Fig. 39.

The experimental specific heat falls below the theoretical curve: the experimental entropy at the highest temperature measured is only 0.7 ln4. It has been suggested that this discrepancy is due to the fine-scale quartet splitting mentioned previously.[65] The specific heat can certainly not be described by assuming a sextet or doublet ground state.

The experimental resistivity[58] is described particularly well by theory: the fit extends over more than three decades in temperature. Subject to the caveat on the use of the Nordheim-Gorter rule, the thermopower is also described well by theory. The thermopower in this system is the largest measured in a dilute Ce alloy; for a sample containing 0.5% Ce, the peak value before the Nordheim-Gorter correction is 66 μV/K. In comparison, typical metallic thermopowers are of order 1 μV/K.

The present calculations, which rigorously pertain to dilute Ce alloys, provide a surprisingly good description of the density of states and spin spectrum in concentrated systems as well. These properties are essentially local in character and are relatively insensitive to f-electron coherence. Note that the simple relationship between the f density of states and the conduction electron scattering rate breaks down in concentrated systems; for this reason, transport properties may radically differ in dilute and concentrated systems even though similar $4f$ densities of states are present.

Due to signal-to-noise limitations, f photoemission experiments are not feasible in the dilute limit and must be conducted in concentrated systems. Detailed comparisons with experiment have been made by Gunnarsson and Schönhammer[66] within a zero-temperature large-degeneracy expansion. We would like to emphasize aspects of the finite-temperature theory relevant to such comparisons. Most photoemission and inverse photoemission experiments are performed at room temperature. Recall that in the simplest picture of Ce alloys, the weight of the Kondo resonance is of order $1-n_f$, where n_f is the f valence. The weight becomes vanishingly small when the Kondo scale T_0 is itself small; furthermore, the weight at low energies decreases as the Kondo resonance broadens with increasing temperature. In contrast, the low-energy weight observed in photoemission experiments is typically quite large, even at room temperature. Gunnarsson and Schönhammer have considered several effects which alter the simplest theoretical picture. These include (a) conduction-band structure; if the conduction density of states is sharply peaked below the Fermi level, additional low-energy weight may appear in the f density of states as well (cf. the behavior of bonding antibonding levels in one-body models); (b) f^2 admixture in the ground state (i.e., finite-U effects); and (c) spin-orbit multiplet structure. We have considered the last effect as well. The presence of spin-orbit structure may partially account for the large temperature-insensitive weight observed in high-resolution studies[54] of γ- and α-Ce (see Fig. 43). The spectra may be qualitatively understood as follows: in the low-temperature α phase, the $4f$-band hybridization is relatively strong. Since the spin-orbit splitting and the excited-multiplet Kondo scale are of the same order of magnitude, the characteristic triple peak at low energies (see Fig. 33) is altered: the feature just below the Fermi surface (transition 3 in Fig. 32) and the central Kondo resonance are smeared into a single peak with width $\sim\Delta_{\text{s.o.}}$. At higher temperatures, the α-γ phase transition occurs and the Ce lattice expands by approximately 15% in volume. If it is assumed the principal result of this expansion is a reduction in f-band hybridization, the second density of states in Fig. 43 results. The peaks at low energy are now well resolved, even at temperatures $T > T_0$, T_{ex}. The spin-orbit feature at $-(\Delta_{\text{s.o.}}+T_0-T_{\text{ex}})$ is almost as sharp at 300 K as at zero temperature: this peak measures $f^1 \rightarrow f^0$ transitions between the ground state (and low-lying states with similar $j=\frac{5}{2}$ admixtures) and high-lying states with excitation energy $\sim\Delta_{\text{s.o.}}$; smearing due to thermal occupancy effects is negligible for temperatures $\ll\Delta_{\text{s.o.}}$. It is plausible that the experimental peak observed in γ-Ce (but not in α-Ce) is a spin-orbit feature of this type.

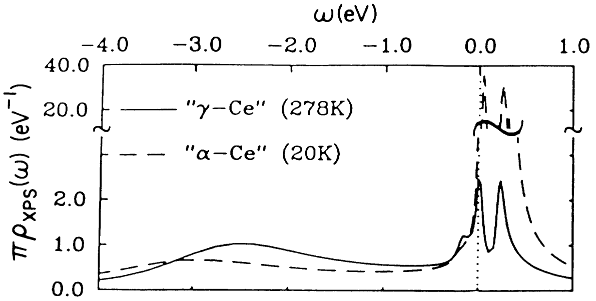

FIG. 43. Model spectra for α- and γ-Ce. The spectra shown for α- and γ-Ce correspond to parameter sets 7 and 6 of Table I, with $D=3$ eV. The values of the Kondo scale T_0 are 520 and 30 K. The four resonances described in Figs. 32 and 33 are well resolved in the γ-Ce spectrum, even at 278 K ($T/T_0 \sim 9$). The increased hybridization width in α-Ce shifts the bottom resonance (transition 4 in Fig. 32) to lower energy; since T_{ex} and $\Delta_{\text{s.o.}}$ are of the same order of magnitude, the resonances for transitions 1 and 3 are smeared into a single feature with width $\sim\Delta_{\text{s.o.}}=0.21$ eV. The resonance for transition 2 at $T_0+\Delta_{\text{s.o.}}$ remains well resolved.

A detailed comparison of theory and experiment for the dynamic susceptibility Imχ is possible in at least one instance. The spectrum of CePd$_3$ at 5 and 280 K has been measured by Galera *et al.*[67] The spectrum is compared with a quasielastic Lorentzian line shape and with large-N results in Fig. 44. The experimental spectrum shows large deviations from quasielastic behavior and is better described by the theoretical line shape for $T \rightarrow 0$. This is expected since the experimental temperature is much smaller than the characteristic scale estimated from the specific heat[67] (~ 750 K).

More generally, the large-degeneracy expansion provides a qualitative description of trends in neutron scatter-

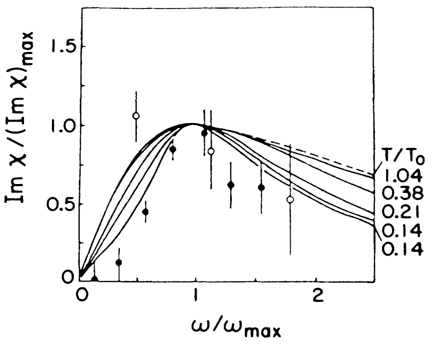

FIG. 44. Comparison of theory and experiment (Ref. 67) for the dynamic magnetic susceptibility $\mathrm{Im}\chi(\omega)$. The frequency and susceptibility scales are set by the peak value of the spectrum at each temperature, $(\mathrm{Im}\chi)_{\max}$ at $\omega_{\max}$. The solid circles are experimental points for CePd_3 at 5 K, and the open circles experimental points at 280 K. Values of $(\mathrm{Im}\chi)_{\max}$ and $(\mathrm{Im}\chi)_{\max}$ for the 280-K data were deduced by (a) extracting a value of T_0 from the 5-K data, (b) computing T/T_0 for $T=280$ K, and (c) reading off the required information from the theoretical spectrum (cf. Fig. 8) for that value of T/T_0. The solid lines are results of the large-degeneracy expansion in the scaling regime; the dashed line corresponds to the standard quasielastic line shape,

$$\mathrm{Im}\chi(\omega)/\chi(T)=\frac{\omega\Gamma_Q(T)}{\omega^2+\Gamma_Q^2(T)} .$$

The experimental spectrum shows clear deviations from quasielastic behavior at 5 K and is reasonably described by the large-degeneracy results for $T\rightarrow 0$.

ing linewidths. Linewidth measurements are typically reported for temperatures in the range 4–300 K.[68] Systems in which the linewidth increases with temperature over this range (often roughly as $T^{1/2}$) are said to exhibit "Kondo lattice" behavior; the characteristic scale (from specific heat measurements) is typically of order 10–20 K.[68] On the other hand, systems with a large temperature-independent linewidth over the same range are said to exhibit "mixed-valent" behavior; the characteristic scale is in this case on the order of hundreds of degrees. As shown in Fig. 45, the present theory allows "Kondo lattice" and "mixed-valent" behavior by a single system in different temperature regimes. For temperatures below the Kondo scale, the linewidth is temperature independent; for temperatures above the Kondo scale, the line-width increases with T. Within a sufficiently small temperature range, only one type of behavior may be observable. The large-degeneracy expansion provides a consistent interpretation for both "Kondo lattice" and "mixed-valent" linewidths. Recent NMR measurements[69] on ten different materials are in good agreement with the results described here over two to three decades of temperature. (Note that NMR samples an effective linewidth corresponding to the quantity $\chi\lim_{\omega\rightarrow 0}\omega/\mathrm{Im}\chi$.)

The present calculations have been limited to the scaling, or Kondo, regime. The detailed behavior of the neutron linewidth in the strongly mixed-valent regime has not been studied. It is possible that some systems with "mixed-valent" linewidths would be better described by parameters in this regime. Nevertheless, many concentrated systems with both "Kondo lattice" and "mixed-valent" linewidths show evidence for single-parameter scaling: this suggests the applicability of Kondo regime studies.

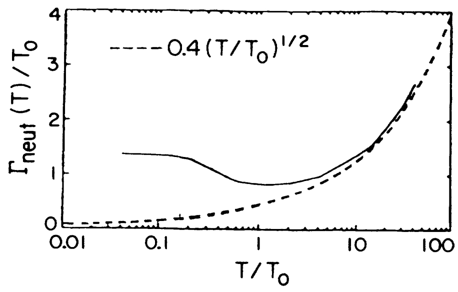

FIG. 45. Neutron scattering linewidth $\Gamma_{\mathrm{neut}}(T)$ in the Kondo regime. The linewidth is defined operationally as the position of the peak in the f moment spectrum $\sigma_f(\omega)=\pi^{-1}\mathrm{Im}\chi(\omega)$ (see Fig. 8). The linewidth is temperature independent for $T<T_0$; at higher temperature, the linewidth increases with a $T^{1/2}$ power law.

VII. CONCLUSIONS

The self-consistent large-degeneracy expansion provides a unified picture of both the static and dynamic properties of magnetic alloys over essentially the full range of temperature. Only in the extreme low-temperature regime ($T \ll T_0$) is the method inadequate (see Secs. V A, V F, and Appendix C). Comparisons of the calculated susceptibility and specific heat with exact Bethe-*ansatz* results indicate that the self-consistent approach is quantitatively accurate for degeneracies as low as four.[70] Direct comparison with experiment (see Sec. VI) provides a stringent test of the method's success: the susceptibility, specific heat, resistivity, and thermopower of $(La,\mathrm{Ce})\mathrm{B}_6$, an exceptionally well-studied Ce alloy, may be consistently described using a single parameter, the Kondo scale T_0.

The self-consistent approach has been extended to describe the properties of systems with spin-orbit splitting (see Sec. V B). (It is conceptually trivial to describe in addition systems with crystalline electric field, or magnetic field, splitting.) The incorporation of such effects is a step in the development of a "first-principles" description of transition-metal and lanthanide alloy properties.

Interesting problems in dilute alloy physics which remain for future study include the following: (a) development of a comparable theory for systems with more complex multiplet structure (e.g., alloys of Sm, Tm, and U);[71] (b) investigation of higher-order extensions of the self-consistent approach described above;[72] and (c) calculation of additional properties, such as the spin and charge polarization in the vicinity of an impurity, and the Knight shift. Of potentially greater interest are possible extensions of the dilute alloy approach to concentrated systems; while success in the dilute limit in no way guarantees the applicability of the large degeneracy concept in the concentrated limit, it is tempting to believe that some aspects of the approach may be of greater generality.

In conclusion, the self-consistent large-degeneracy expansion is a new theoretical tool for analyzing magnetic alloys, which emphasizes the simplifying features of the Kondo effect, while allowing quantitatively accurate calculations. While the method does not constitute a "solution" of the Kondo problem, it furnishes one of the most complete pictures of magnetic alloy physics now available.

ACKNOWLEDGMENTS

We have benefited from conversations or correspondence with J. W. Allen, P. Coleman, R. M. Galera, O. Gunnarsson, H. R. Krishna-murthy, T. K. Lee, M. Loewenhaupt, D. E. MacLaughlin, S. Maekawa, M. B. Maple, E. Müller-Hartmann, A. P. Murani, N. Read, D. Wieliczka, and F. C. Zhang. This work was supported at Cornell University by the U.S. Department of Energy (Basic Energy Sciences, Division of Materials Research). One of us (N.E.B.) was partially supported by the National Science Foundation (NSF). One of us (D.L.C.) acknowledges the support of NSF Grant No. DMR-85-14195 under the supervision of L. J. Sham at the University of California, San Diego, and the support of NSF Grant No. PHY82-17853 and funds from U.S. National Aeronautics and Space Administration (NASA) during a stay at the Institute for Theoretical Physics. Finally, we are grateful for the hospitality of the IBM Thomas J. Watson Research Center (Yorktown Heights, NY) and the Institute for Theoretical Physics (Santa Barbara, CA), where portions of this work were completed.

APPENDIX A: NUMERICAL DETAILS

In this appendix we provide technical details on the numerical solution of the self-consistent integral equations, the calculation of the f density of states and moment spectrum, and the evaluation of the specific heat.

1. Negative-frequency distribution functions

While, in principle, all quantities are computed in terms of the empty- and occupied-state distribution functions $\rho_0(\omega,T)$ and $\rho_m(\omega,T)$, it is convenient to define "negative-frequency distribution functions" $\rho_0^{(-)}$ and $\rho_m^{(-)}$ by

$$\begin{aligned}\rho_0^{(-)}(\omega,T)&=e^{-\beta[\omega-E_T(T)]}\rho_0(\omega,T)\ ,\\ \rho_m^{(-)}(\omega,T)&=e^{-\beta[\omega-E_T(T)]}\rho_m(\omega,T)\ .\end{aligned} \tag{A1}$$

$E_T(T)$ is an offset energy set at the programmer's convenience: to obtain accurate results, $E_T(T)$ should be close to the NCA ground state energy E_0.

It is necessary to define such functions since the "positive-frequency" distribution functions ρ_0 and ρ_m vanish exponentially fast below the energy E_0; in expressions for the partition function and correlation functions, ρ_0 and ρ_m must be multiplied by an exponentially growing Boltzmann factor. Such a procedure is subject to gross numerical error when the Boltzmann factor and distribution function are separately computed.

The positive-frequency distribution functions are determined by the self-energies Σ_0 and Σ_m. The only new quantities which must be calculated to find the negative-frequency functions are

$$\begin{aligned}\mathrm{Im}\Sigma_0^{(-)}(\omega,T)&=e^{-\beta[\omega-E_T(T)]}\mathrm{Im}\Sigma_0(\omega,T)\ ,\\ \mathrm{Im}\Sigma_m^{(-)}(\omega,T)&=e^{-\beta[\omega-E_T(T)]}\mathrm{Im}\Sigma_m(\omega,T)\ .\end{aligned} \tag{A2}$$

2. Conduction-band kernel

While the integral equations for Σ_0 and Σ_m may be evaluated directly as formulated in the text, we actually found it more convenient to use the spectral representation for the f-state propagators: integrals may then be expressed in terms of the positive-definite quantities ρ_0 and ρ_m. For example, the equation for $\Sigma_0(\omega,T)$ is

$$\Sigma_0(\omega+i0^+,T)=\frac{N\Gamma}{\pi}\int_{-\infty}^{\infty}d\xi\,\rho_m(\xi,T)K(\omega-\xi+i0^+,T) \tag{A3}$$

where the kernel $K(z,T)$ is given by

$$K(z,T)=\int_{-\infty}^{\infty}d\varepsilon\,\nu(\varepsilon)\frac{f(\varepsilon)}{z+\varepsilon}\ , \tag{A4}$$

and $\nu(\varepsilon)=N(\varepsilon)/N(0)$ is the normalized density of states. The kernel may be readily evaluated in terms of digamma functions for either a flat or Lorentzian density of states. The digamma functions may in turn be evaluated numerically by applying a recursion formula[78] and asymptotic expansion:

$$\psi(z)=\psi(z+10)-\sum_{n=1}^{10}\frac{1}{z+n-1}\ , \tag{A5}$$

with

$$\psi(z+10)\approx\ln(z+10)-\frac{1}{2(z+10)}-\frac{1}{12(z+10)^2}+\frac{1}{120(z+10)^4}+\cdots\ . \tag{A6}$$

3. Iteration procedure

The individual numerical spectra were evaluated on separate logarithmic meshes running from $\pm\delta_{\min}$ about the sharpest spectral feature to $\pm D_C$, where D_C is some large energy scale of many times the bandwidth. The small increment $\delta_{\min}$ was taken to be an order of magnitude smaller than the sharpest spectral variation. In the runs reported here, D_C was 10^4D. More recent calculations have made it clear that $D_C=30D$ is sufficient for reliable results. The advantage of logarithmic meshes is that spectral features with exponentially varying energy scales may be faithfully represented by relatively few points (compared with the requirements for a linear mesh or a sequence of coarse-grained linear meshes). The results reported here were obtained on 603-point meshes. More recent studies have shown that 83-point meshes are adequate for calculating the static susceptibility, magnetization, and occupancy, while meshes with a few hundred points appear to give reliable spectra.[74] Since the computation time for evaluating the self-energies varies as the number of mesh points squared, these latter numbers represent substantial time savings over the original calculations. Integrals were computed using the trapezoidal rule, and at each stage the normalization of the positive and negative frequency distribution functions was checked. Typically, the positive frequency norms deviated from unity by no more than a part in 10^4. The values of the negative frequency norms were used to monitor the convergence of the iterative solution.

The results reported in this paper were all obtained on an IBM 3081 computer. A single iteration of the coupled integral equations for a 603-point mesh takes approximately 80 CPU seconds [assuming the use of the kernel K in Eq. (A4)]. A fourfold time savings results if the integrals are evaluated without introducing spectral representations; however, this approach leads to a considerable loss of accuracy on coarser meshes. This is presumably due to sign changes in the real parts of the empty- and occupied-state propagators. More recent evaluations on the Cray X-MP/48 computer at the San Diego Computer Center provide a factor of 10 improvement in CPU (central processing unit) time over the IBM results, and a factor of 100 over comparable calculations on a Digital Equipment Corporation VAX-11/780 computer.[74]

Operationally, the iterations are started by a seed at high temperatures: the first order iterates for Σ_0 and $\mathrm{Im}\Sigma_0^{(-)}$ are input to an evaluation of the occupied-state self-energy, with the initial $E_T(T)$ a reasonable approximation to the NCA ground state energy. The converged output ρ_0 and $\rho_0^{(-)}$ spectra are then input as seeds when beginning a lower temperature iteration. We have always found this procedure to be stable. The energy E_T at the lower temperature is not known *a priori*: however, this value may be readily determined from the ratio of negative and positive frequency spectra at a single frequency.

When multiplet structure is to be included (as in spin-orbit calculations), the most convenient approach is to evaluate the contributions of each multiplet to the empty-state self-energy using the single multiplet code, then to add these contributions before computing ρ_0 and $\rho_0^{(-)}$.

4. Convolution integrals for ρ_f and σ_f

Because we have employed logarithmic meshes, standard numerical convolution procedures (such as that based on fast Fourier transforms) are not useful. Hence, we have devised an alternate code for performing convolutions. As an example, consider the following integral to determine the f density of states:

$$\rho_f(\omega)=\frac{1}{Z_f}(1+e^{-\beta\omega})\int_{-\infty}^{\infty}d\varepsilon\,\rho_0^{(-)}(\varepsilon)\rho_m(\varepsilon+\omega)\ . \tag{A7}$$

Denote the mesh centers E_{c0} (empty state) and E_{cm} (occupied state), with $\omega_c\equiv E_{cm}-E_{c0}\sim T_0$. For $0.75\omega_c<\omega<1.25\omega_c$, ρ_m is interpolated onto the empty-state mesh. When ω is larger than $1.25\omega_c$, the integration is broken up into three parts: (a) for $\varepsilon<E_{cm}-\omega$, $\rho_0^{(-)}$ is interpolated onto the occupied-state mesh; (b) for $\varepsilon>E_{c0}$, ρ_m is interpolated onto the empty-state mesh; (c) for $E_{cm}-\omega<\varepsilon<E_{c0}$, all spectra are interpolated onto an intermediate mesh specified by the variable z, where

$$z=\ln\left[\frac{\varepsilon+\omega-E_{cm}}{E_{c0}-\varepsilon}\right]\ , \tag{A8}$$

which varies rapidly near the sharp features of the distribution functions and slowly elsewhere. The interpolation schemes for all frequency regimes are summarized in Table IX.

The results of each convolution are examined visually (sometimes rapidly varying spectra exhibit spurious jumps at the breaks in the mesh), and the sum rules in Eqs. (B9)–(B11) are checked. The sum rules are typically satisfied at the order of a part in 10^3–10^4. The jump problem can be cured by altering the mesh breaks to $0.95T_0$ and $1.05T_0$.

5. Specific-heat evaluation

Evaluation of the specific heat using Eq. (5.18) was straightforward apart from one detail: since the partition function is evaluated in terms of the negative frequency distribution functions, it is necessary to tabulate $E_T(T)$, then shift all partition function data to a common reference value of E_T. Five-point derivative formulas give the best results, and it is best to use a constant set of mesh parameters for all iterations.

APPENDIX B: SUM RULES FOR THE INFINITE-U ANDERSON MODEL

In this appendix we derive several exact sum rules for the infinite-U Anderson model and demonstrate that these rules are satisfied within the self-consistent approximation (the noncrossing approximation).

1. Sum rules from analyticity

Recall from Eqs. (4.9) and (4.10) that the Anderson model partition function may be written

$$\begin{aligned}Z/Z_{\mathrm{band}}&=\int_\Gamma\frac{dz}{2\pi i}e^{-\beta z}\mathrm{Tr}_f\frac{1}{z-H_f-\hat{\Sigma}_f(z)}\\&=\int_\Gamma\frac{dz}{2\pi i}\frac{e^{-\beta z}}{z-\Sigma_0(z)}+N\int_\Gamma\frac{dz}{2\pi i}\frac{e^{-\beta z}}{z-\varepsilon_f-\Sigma_m(z)}\ ,\end{aligned} \tag{B1}$$

where the contour Γ encircles the real axis in a counterclockwise fashion. The "propagators" $(z-\Sigma_0)^{-1}$ and $(z-\varepsilon_f-\Sigma_m)^{-1}$ are analytic in the upper and lower half-planes and decay at infinity as $1/z$, independent of the detailed form of Σ_0 and Σ_m. Distorting the contour Γ into a circle at infinity gives immediately

$$\int_\Gamma\frac{dz}{2\pi i}\frac{1}{z-\Sigma_0(z)}=\int_{-\infty}^{\infty}d\varepsilon\,\rho_0(\varepsilon)=1\ ,$$

with

$$\rho_0(\varepsilon)=-\frac{1}{\pi}\mathrm{Im}\frac{1}{\varepsilon+i0^+-\Sigma_0(\varepsilon+i0^+)}\ ; \tag{B2}$$

TABLE IX. Details of the meshes for numerical convolutions. The empty- and occupied-state distribution functions are centered at E_{c0} and E_{cm}; $\omega_c = E_{cm} - E_{c0}$ is the separation of the mesh centers.

(i) $0.75\omega_c \le \omega \le 1.25\omega_c$

→$\rho_0^{(-)}(\varepsilon,T)$ is interpolated onto the $\rho_m(\varepsilon+\omega,T)$ mesh.

(ii) $1.25\omega_c < \omega$

→ for $\varepsilon < E_{cm} - \omega$, $\rho_0^{(-)}(\varepsilon,T)$ is interpolated onto the $\rho_m(\varepsilon+\omega,T)$ mesh.
→ for $\varepsilon > E_{c0}$, $\rho_m(\varepsilon+\omega,T)$ is interpolated onto the $\rho_0^{(-)}(\varepsilon,T)$ mesh.
→ for $E_{cm} - \omega < \varepsilon < E_{c0}$, both spectra are interpolated onto the mesh specified by (A8).

(iii) $0 < \omega < 0.75\omega_c$

→ for $\varepsilon > E_{cm} - \omega$, $\rho_0^{(-)}(\varepsilon,T)$ is interpolated onto the $\rho_m(\varepsilon+\omega,T)$ mesh.
→ for $\varepsilon < E_{c0}$, $\rho_m(\varepsilon+\omega,T)$ is interpolated onto the $\rho_0^{(-)}(\varepsilon,T)$ mesh.
→ for $E_{c0} < \varepsilon < E_{cm} - \omega$, both spectra are interpolated onto an intermediate mesh specified by the variable z with

$$z = \ln\left[\frac{\varepsilon - E_{c0}}{E_{cm} - \omega - \varepsilon}\right] .$$

(iv) $\omega < 0$

→ for $\varepsilon < E_{c0} - |\omega|$, $\rho_m^{(-)}(\varepsilon,T)$ is interpolated onto the $\rho_0(\varepsilon+|\omega|,T)$ mesh.
→ for $\varepsilon > E_{cm}$, $\rho_0(\varepsilon+|\omega|,T)$ is interpolated onto the $\rho_m^{(-)}(\varepsilon,T)$ mesh.
→ for $E_{c0} - |\omega| < \varepsilon < E_{cm}$, both spectra are interpolated onto an intermediate mesh specified by the variable z with

$$z = \ln\left[\frac{\varepsilon + |\omega| - E_{c0}}{E_{cm} - \varepsilon}\right] .$$

and

$$\int_\Gamma \frac{dz}{2\pi i}\frac{1}{z - \varepsilon_f - \Sigma_m(z)} = \int_{-\infty}^{\infty} d\varepsilon\, \rho_m(\varepsilon) = 1 ,$$

with

$$\rho_m(\varepsilon) = -\frac{1}{\pi}\mathrm{Im}\frac{1}{\varepsilon + i0^+ - \varepsilon_f - \Sigma_m(\varepsilon + i0^+)} . \tag{B3}$$

2. Sum rules from equal-time correlation functions

First we look at $G_f(\tau)$. Recall that the correlation function

$$G_f(\tau) \equiv -\langle \mathcal{T}_\tau F_m(\tau) F_m^\dagger(0)\rangle ,$$
$$F_m = |0\rangle\langle m| , \tag{B4}$$

has the frequency decomposition

$$G_f(\tau) = \frac{1}{\beta}\sum_n e^{-i\omega_n\tau}\int_\Gamma \frac{dz}{2\pi i}\frac{G_f(z)}{i\omega_n - z}$$
$$= \int_{-\infty}^{\infty} d\varepsilon\, \rho_f(\varepsilon)\frac{1}{\beta}\sum_n \frac{e^{-i\omega_n\tau}}{i\omega_n - \varepsilon} , \tag{B5}$$
$$\rho_f(\varepsilon) = -\frac{1}{\pi}G_f(\varepsilon + i0^+) .$$

From the definition,

$$G_f(\tau\to 0^+) = -\langle F_m F_m^\dagger\rangle = -\langle \{ |0\rangle\langle m||m\rangle\langle 0| \}\rangle$$
$$= -[1 - n_f(T)] ; \tag{B6}$$

likewise,

$$G_f(\tau\to 0^-) = \langle F_m^\dagger F_m\rangle = \frac{1}{N}n_f(T) . \tag{B7}$$

Since

$$\sum_n \frac{e^{-i\omega_n 0^\pm}}{i\omega_n - \varepsilon} = \frac{\mp 1}{e^{\mp\beta\varepsilon} + 1} , \tag{B8}$$

it follows that

$$\int_{-\infty}^{\infty} d\varepsilon\, \rho_f(\varepsilon)[1 - f(\varepsilon)] = 1 - n_f(T) , \tag{B9}$$

$$\int_{-\infty}^{\infty} d\varepsilon\, \rho_f(\varepsilon) f(\varepsilon) = \frac{1}{N}n_f(T) , \tag{B10}$$

and

$$\int_{-\infty}^{\infty} d\varepsilon\, \rho_f(\varepsilon) = 1 - \left[1 - \frac{1}{N}\right]n_f(T) . \tag{B11}$$

Next we look at $M_f(\tau)$. The correlation function

$$M_f(\tau) \equiv -\langle \mathcal{T}_\tau \hat{M}(\tau)\hat{M}(0)\rangle ,$$
$$\hat{M} = g\mu_B\sum_m m\hat{N}_m \tag{B12}$$

has the frequency decomposition

$$M_f(\tau) = \int_{-\infty}^{\infty} d\varepsilon\, \sigma_f(\varepsilon)\frac{1}{\beta}\sum_m \frac{e^{-i\nu_m\tau}}{i\nu_m - \varepsilon} ,$$
$$\sigma_f(\varepsilon) = -\frac{1}{\pi}\,\mathrm{Im}M_f(\varepsilon + i0^+) , \tag{B13}$$

with $\nu_m = 2m\pi T$ a Bose frequency. Note σ_f is an odd function of frequency. By definition,

$$M_f(\tau \to 0^+) = -(g\mu_B)^2 \sum_{m,m'} mm' \langle \hat{N}_m \hat{N}_{m'} \rangle$$
$$= -(g\mu_B)^2 \sum_m m^2 \langle \hat{N}_m \rangle = -\frac{\mu_j^2}{3} n_f(T) \tag{B14}$$

with

$$\mu_j^2 = j(j+1)(g\mu_B)^2 \ .$$

Since

$$\frac{1}{\beta} \sum_m \frac{e^{-i\nu_m 0^\pm}}{i\nu_m - \varepsilon} = \frac{\pm 1}{e^{\mp\beta\varepsilon - 1}} \equiv \pm b(\mp\varepsilon) \ , \tag{B15}$$

it follows that

$$\int_{-\infty}^{\infty} d\varepsilon\, \sigma_f(\varepsilon) b(\varepsilon) = -\int_{-\infty}^{\infty} d\varepsilon\, \sigma_f(\varepsilon) b(-\varepsilon) = \frac{\mu_j^2}{3} n_f(T) \ . \tag{B16}$$

3. Sum rules within the self-consistent approximation

The sum rules (B2) and (B3) are trivially satisfied within the self-consistent large-degeneracy expansion. The sum rules (B9)–(B11) and (B16) are also satisfied.

Proof: The self-consistent approximation for the f density of states is

$$\rho_f(\omega) = \frac{1}{Z_f}(1 + e^{-\beta\omega}) \int_{-\infty}^{\infty} d\varepsilon\, e^{-\beta\varepsilon} \rho_0(\varepsilon) \rho_m(\omega + \varepsilon) \ ,$$
$$Z_f = \int_{-\infty}^{\infty} d\varepsilon [\rho_0(\varepsilon) + N\rho_m(\varepsilon)] \ . \tag{B17}$$

Thus,

$$\int_{-\infty}^{\infty} d\omega\, \rho_f(\omega)[1 - f(\omega)]$$
$$= \frac{1}{Z_f} \int_{-\infty}^{\infty} d\varepsilon\, e^{-\beta\varepsilon} \rho_0(\varepsilon) \rho_m(\omega + \varepsilon)$$
$$= \frac{1}{Z_f} \int_{-\infty}^{\infty} d\varepsilon\, e^{-\beta\varepsilon} \rho_0(\varepsilon) = 1 - n_f(T) \ , \tag{B18}$$

by Eq. (B2). Sum rules (B10) and (B11) follow in similar fashion.

The self-consistent approximation for the f moment spectrum is

$$\sigma_f(\omega) = \frac{N\mu_j^2}{3} \frac{1}{Z_f} (e^{\beta\omega} - 1) \int_{-\infty}^{\infty} d\varepsilon\, e^{-\beta\varepsilon} \rho_m(\varepsilon) \rho_m(\varepsilon - \omega) \ . \tag{B19}$$

Thus,

$$\int_{-\infty}^{\infty} d\omega\, b(\omega) \sigma_f(\omega)$$
$$= \frac{N\mu_j^2}{3} \frac{1}{Z_f} \int_{-\infty}^{\infty} d\varepsilon\, e^{-\beta\varepsilon} \rho_m(\varepsilon) \rho_m(\varepsilon - \omega)$$
$$= \frac{N\mu_j^2}{3} \frac{1}{Z_f} \int_{-\infty}^{\infty} d\varepsilon\, e^{-\beta\varepsilon} \rho_m(\varepsilon) = \frac{\mu_j^2}{3} n_f(T) \ . \tag{B20}$$

APPENDIX C: FERMI LIQUID RELATIONS WITHIN THE SELF-CONSISTENT APPROXIMATION

A number of exact sum rules and Fermi-liquid relations for the degenerate-orbital Anderson model may be established to all orders in perturbation theory. We reserve the name "sum rule" for global (i.e., integrated) frequency relations based on the properties of equal-time correlation functions (see Appendix B); and the name "Fermi liquid relation" for identities connecting thermodynamic derivatives, or zero-frequency correlation functions and thermodynamic derivatives. A number of Fermi liquid relations for the Hamiltonian of Eq. (2.10) are listed in Table V. These relations may be established by all-orders perturbation theory in the Coulomb energy U; the relations remain valid in the limit $U \to \infty$.

Arbitrary approximations in diagrammatic perturbation theory need not preserve such results. In general, the self-consistent large-degeneracy expansion discussed in the text (a) obeys sum rules (see Appendix B) and (b) violates Fermi liquid relations. The second point limits the utility of the expansion in the extreme low-temperature or low-frequency limit ($T \ll T_0$, $\omega \ll T_0$). Müller-Hartmann[53] and Kuramoto[50] have quantified the violation of Fermi liquid relations through analytical studies of the self-consistent approximation. At zero temperature, the integral equations discussed in Sec. IV may be converted to differential equations following a technique introduced by Inagaki.[75] The following results have been established for the asymptotic low-frequency forms of the spectra ρ_f and σ_f within the self-consistent approximation (a flat density of states with half-width D is assumed):

$$\rho_f^{\mathrm{NCA}}(\omega) \sim \frac{\pi}{(N+1)^2\Gamma} - \frac{1}{(N+1)^2\Gamma} 4 \sin\left[\frac{\pi}{N+1}\right]$$
$$\times \left[\frac{1}{N+2} B\left[\frac{2}{N+1}, \frac{N}{N+1}\right] \left\{ \begin{matrix} 1 \\ \cos\pi/(N+1) \end{matrix} \right\} \times \frac{T_{\mathrm{NCA}}}{\Gamma/\pi} \left[\frac{(N+1)|\omega|}{T_{\mathrm{NCA}}}\right]^{1/(N+1)} \right.$$
$$\left. + \frac{1}{2N+1} B\left[\frac{1}{N+1}, \frac{2N}{N+1}\right] \left\{ \begin{matrix} 1 \\ \cos\pi N/(N+1) \end{matrix} \right\} \times \left[\frac{(N+1)|\omega|}{T_{\mathrm{NCA}}}\right]^{N/(N+1)} \right], \quad \left\{ \begin{matrix} \omega > 0 \\ \omega < 0 \end{matrix} \right\} , \tag{C1}$$

$$T_{\mathrm{NCA}} \equiv D(\Gamma/\pi D)^{1/N}\exp(\pi\varepsilon_f/N\Gamma) \sim T_0 ,$$

with B the beta function;

$$\sigma_f^{\mathrm{NCA}}(\omega) \sim \frac{\mu_j^2}{3}\,\frac{N}{N+1}\,\frac{\omega}{\pi T_{\mathrm{NCA}}^2}\left[\frac{(N+1)\,|\,\omega\,|}{T_{\mathrm{NCA}}}\right]^{-2/(N+1)} \sin\left[\frac{\pi}{N+1}\right] B\left[\frac{N}{N+1},\frac{N}{N+1}\right] . \tag{C2}$$

(The subscript "NCA" is a mnemonic for the noncrossing approximation.) The complete f Green's function at the Fermi surface takes the form

$$G_f^{\mathrm{NCA}}(i0^+) = \frac{\pi}{(N+1)\Gamma}\left[1-\frac{N+1}{N}n_f-\frac{\pi}{N+1}\cot\left[\frac{\pi}{N+1}\right] \mp \frac{i\pi}{N+1}\right] , \tag{C3}$$

so that the imaginary part of the self-energy becomes

$$\mathrm{Im}\Sigma_f^{\mathrm{NCA}}(i0^+) = -\Gamma\left[\left[1-\frac{N+1}{N}n_f-\frac{\pi}{N+1}\cot\frac{\pi}{N+1}\right]^2+\frac{\pi^2}{(N+1)^2}\right]^{-1} . \tag{C4}$$

The first two Fermi liquid relations in Table V state that the character of the f electron self-energy at zero frequency is unchanged by the presence of Coulomb correlations. It is clear from Eq. (C4) that the first relation is violated by the self-consistent large-degeneracy expansion; for $N \rightarrow \infty$,

$$\mathrm{Im}\Sigma_f^{\mathrm{NCA}}(i0^+) \sim -\Gamma/n_f^2 . \tag{C5}$$

This result approaches the exact result only in the integral valent, or Kondo, limit $n_f \rightarrow 1$. The second Fermi liquid relation is also violated since the self-consistent Green's function is nonanalytic at $\omega = 0$: the density of states exhibits a slightly asymmetric and very sharp cusp $(\sim |\,\omega\,|^{1/N+1})$ at $\omega = 0$.

The third and fourth Fermi liquid relations connect thermodynamic derivatives with low-frequency dynamic properties. The third relation is clearly violated since

$$\rho_f^{\mathrm{NCA}}(0) = \frac{\pi}{(N+1)^2\Gamma} , \tag{C6}$$

a value independent of the valence; once again, the correct value is approached in the integral valent limit for large N. The self-consistent approximation fails most severely for the fourth relation: the quantity $\sigma_f^{\mathrm{NCA}}(\omega)/\omega$ actually diverges for $\omega \rightarrow 0$.

The appearance of nonanalytic features in ρ_f and σ_f indicates the failure of the self-consistent large-degeneracy expansion at zero temperature and frequency. In general, however, a violation of Fermi-liquid relations does not imply the inadequacy of an approximation scheme at finite temperature and frequency. In the present case, spurious nonanalytic features are restricted to an unphysically small energy scale (i.e., a scale much smaller than T_0 or T_0/N, the smallest physically relevant energies).

The anomaly scale for the f density of states may be estimated quantitatively. Note that the sharp cusp which dominates $\rho_f(\omega)$ for $\omega \rightarrow 0$ falls off rapidly; for larger ω (still in the asymptotic regime), the dominant contribution to the density of states varies as $|\,\omega\,|^{N/(N+1)}$. For large N, this term becomes indistinguishable from a linear contribution. Thus, on a coarse-grained frequency scale, the density of states appears smooth down to an energy of the order of T_{NCA}^*, a characteristic crossover energy for the two asymptotic contributions in Eq. (C1). We define T_{NCA}^* as the energy $\omega > 0$ at which these contributions to ρ_f are equal. By a short computation,

$$\begin{aligned} T_{\mathrm{NCA}}^* &= \frac{T_{\mathrm{NCA}}}{N+1}\left[\frac{2N+1}{N+2}\,\frac{B_1}{B_2}\,\frac{T_{\mathrm{NCA}}}{\Gamma/\pi} \times \sec\left[\frac{\pi}{N+1}\right]\right]^{(N+1)/(N-1)} \\ &\rightarrow \frac{T_{\mathrm{NCA}}}{N+1}\left[\frac{T_{\mathrm{NCA}}}{\Gamma/\pi}+O(1/N)\right]^{(N+1)/(N-1)} , \end{aligned}$$

with

$$\begin{aligned} B_1 &= B\left[\frac{2}{N+1},\frac{N}{N+1}\right] , \\ B_2 &= B\left[\frac{1}{N+1},\frac{2N}{N+1}\right] . \end{aligned} \tag{C7}$$

The height of the cusp above its value at the crossover energy is

$$\frac{\rho_f(0)-\rho_f(T_{\mathrm{NCA}}^*)}{\rho_f(T_{\mathrm{NCA}}^*)} = O\left[\left[\frac{T_{\mathrm{NCA}}}{\Gamma/\pi}\right]^{N/(N-1)}\right] . \tag{C8}$$

The cusp anomaly may have a sizable effect over a large energy range in the mixed valent regime, where $T_{\mathrm{NCA}} \sim \Gamma$; however, in the Kondo regime, where $T_{\mathrm{NCA}} \ll \Gamma$, the crossover scale T_{NCA}^* is tiny $[O(T_{\mathrm{NCA}}/\Gamma)]$ in comparison with T_{NCA}, and the relative height of the cusp above background at $\omega = T_{\mathrm{NCA}}^*$ is equally small. At finite temperatures, thermal smearing prevents the observation of zero-temperature spectral features with energy scales smaller than T; the temperature acts as a natural coarse-graining scale. This means that, in the Kondo regime, self-consistent calculations should not produce an anomalous zero-frequency feature for $T > T_{\mathrm{NCA}}^*$. In particular, if the onset of a Fermi-liquid regime (in which properties vary with simple power-law temperature dependences) occurs at $T > T_{\mathrm{NCA}}^*$, one expects extrapolations of self-consistent calculations to zero temperature, or frequency, to be reliable.

Numerical results indicate that the anomaly scale for the f moment spectrum is somewhat larger than that for the f density of states (see Fig. 26). An analytical estimate of this scale is in principle possible, but has not been attempted. It is clear from Fig. 26 that the new anomaly scale is, like T^{*}_{NCA}, much smaller than the relevant physical scale T_0.

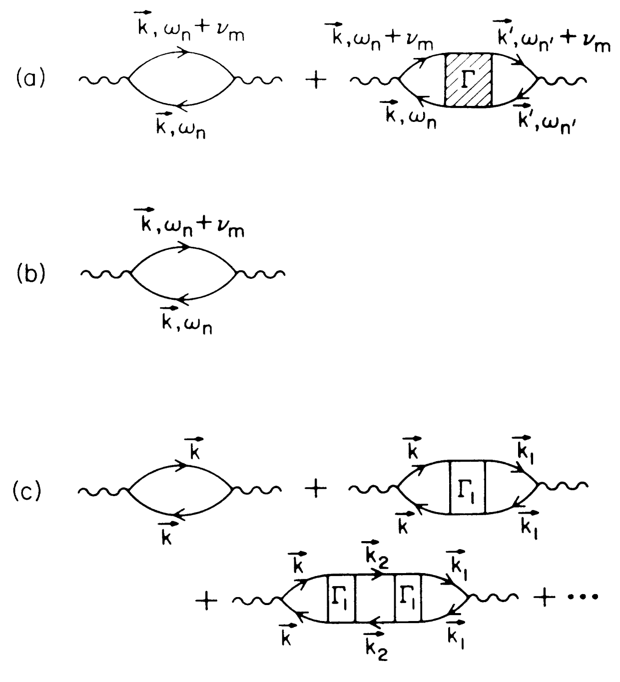

FIG. 46. Diagrammatic representation of the current-current correlation function. Solid lines represent conduction electron propagators dressed by interaction with impurities; rectangles represent two-particle scattering vertices Γ. (a) General representation of the correlation function. The first diagram includes all scattering events which occur independently on the upper and lower lines; the shaded vertex Γ in the second diagram includes, by definition, all *joint* scattering events from one or more impurities. (b) Simplest contribution to (a). Vertex corrections [the second diagram in (a)] drop out when scattering occurs in a single angular momentum channel. (c) Simplest ladder diagrams contained in (a).

APPENDIX D: DERIVATION OF TRANSPORT INTEGRALS FOR RARE-EARTH IMPURITY SYSTEMS

In this appendix, we derive expressions for the transport coefficients of a system containing rare-earth impurities. The Hamiltonian and notational conventions have been presented in Sec. IV. In the linear response regime, transport properties may be expressed in terms of particle- and energy-current correlation functions.[76] Specifically, the dc conductivity tensor takes the form

$$\sigma_{\alpha\beta}(T) = -\lim_{\omega\to 0}\left[\frac{1}{\omega}\mathrm{Im}\int_{-\infty}^{\infty} dt\, e^{i(\omega+i0^{+})t}\Pi_{\alpha\beta}(t)\right] \tag{D1}$$

where $\Pi_{\alpha\beta}$ is the current-current correlation function

$$\begin{aligned}\Pi_{\alpha\beta}(t) &= -i\Theta(t)\langle [j_\alpha(t), j_\beta(0)]\rangle\ ,\\ \mathbf{j}(t) &= \frac{1}{\mathcal{V}}\int d\mathbf{r}\,\mathbf{j}(r)\ ,\end{aligned} \tag{D2}$$

with $\mathcal{V}$ the system volume. For convenience, we set $\mathcal{V}=1$ hereafter. For plane-wave conduction states, the current operator

$$\mathbf{j} = -\frac{e}{m}\sum_{\mathbf{k},\sigma}\mathbf{k}c^{\dagger}_{\mathbf{k}\sigma}c_{\mathbf{k}\sigma}\ . \tag{D3}$$

Note the sign convention $e = |e|$.

The conductivity tensor in a system with randomly distributed impurities is diagonal. It suffices to calculate the Matsubara correlation function

$$\begin{aligned}\Pi(i\nu_m) &\equiv \tfrac{1}{3}\int_0^{\beta} d\tau\, e^{i\nu_m\tau}[-\langle \mathcal{T}_\tau \mathbf{j}(\tau)\cdot\mathbf{j}(0)\rangle]\\ &= \frac{1}{3}\frac{e^2}{m^2}\sum_{\mathbf{k},\mathbf{k}',\sigma}(\mathbf{k}\cdot\mathbf{k}')\int_0^{\beta} d\tau\, e^{i\nu_m\tau}[-\langle \mathcal{T}_\tau c^{\dagger}_{\mathbf{k}\sigma}(\tau)c_{\mathbf{k}\sigma}(\tau)c^{\dagger}_{\mathbf{k}'\sigma}(0)c_{\mathbf{k}'\sigma}(0)\rangle]\ ;\end{aligned} \tag{D4}$$

the retarded function follows by analytic continuation. The last integral has the diagrammatic representation in Fig. 46(a). Solid lines represent dressed conduction electron propagators; the shaded vertex represents the full two-particle interaction with impurities. It is shown below that the diagram containing Γ does not contribute to Π; only the simple polarization bubble in Fig. 46(b) need be considered. This result is well known for s-wave impurity scattering; it continues to hold as long as the scattering process takes place in a single angular momentum channel.

Consider first the conduction-band propagator

$$G_{\mathbf{k}\sigma\mathbf{k}'\sigma'}(i\omega_n) = \int_0^{\beta} d\tau\, e^{i\omega_n\tau}[-\langle \mathcal{T}_\tau c_{\mathbf{k}\sigma}(\tau)c^{\dagger}_{\mathbf{k}'\sigma'}(0)\rangle] \tag{D5}$$

in the presence of a single impurity at $\mathbf{R}_i$. By an equation-of-motion treatment (or direct diagrammatic summation), the propagator may be expressed exactly in terms of the fully dressed impurity propagator G_f. Thus,

$$G_{\mathbf{k}\sigma\mathbf{k}'\sigma'}(i\omega_n) = G^{0}_{\mathbf{k}\sigma}(i\omega_n)\delta_{\mathbf{k}\mathbf{k}'}\delta_{\sigma\sigma'} + G^{0}_{\mathbf{k}\sigma}(i\omega_n)T_{\mathbf{k}\sigma\mathbf{k}'\sigma'}(i\omega_n)G_{\mathbf{k}'\sigma'}(i\omega_n)\ ,$$

where

$$T_{\mathbf{k}\sigma\mathbf{k}'\sigma'} = V^2 G_f(i\omega_n)\times 4\pi\sum_{m}\langle\sigma\,|\,m\rangle\langle\sigma'\,|\,m\rangle Y_{l,m-\sigma}(\hat{\mathbf{k}})Y^{*}_{l,m-\sigma'}(\hat{\mathbf{k}}')e^{i(\mathbf{k}-\mathbf{k}')\cdot\mathbf{R}_i}$$

and

$$\langle \sigma \mid m \rangle \equiv \langle s=\tfrac{1}{2}\, l\, \sigma\, m-\sigma \mid s=\tfrac{1}{2}\, l\, j\, m \rangle \ . \tag{D6}$$

The spherical harmonics and Clebsch-Gordon coefficients follow from expressing $c^{\dagger}_{\mathbf{k}\sigma}$ and $c_{\mathbf{k}'\sigma'}$ in terms of the spherical-wave operators in the interaction Hamiltonian [Eq. (4.1)].[48]

The angular sum in (D6) may be reduced to a simple form for $\hat{\mathbf{k}}=\hat{\mathbf{k}}'$:

$$4\pi \sum_{m} \langle \sigma \mid m \rangle \langle \sigma' \mid m \rangle Y_{l,m-\sigma}(\hat{\mathbf{k}}) Y^{*}_{l,m-\sigma'}(\hat{\mathbf{k}}) = \frac{2j+1}{2}\delta_{\sigma\sigma'} \ . \tag{D7}$$

The factor $(2j+1)/2$ just counts the number of angular momentum channels available for scattering with spin conservation. In the absence of spin-orbit coupling, this factor would be $2l+1$.

In the presence of many impurities, the scattering matrix $T_{\mathbf{k}\sigma\mathbf{k}'\sigma'}$ must be generalized. In the extremely dilute limit, impurity-impurity interactions and correlated scattering involving two or more impurities may be ignored. The scattering matrix in (D6) is replaced by the obvious generalization describing uncorrelated scattering by one or more impurities:

$$\begin{aligned} G_{\mathbf{k}\mathbf{k}';\sigma}(i\omega_n) &= G^{0}_{\mathbf{k}\sigma}(i\omega_n)\delta_{\mathbf{k}\mathbf{k}'} + \sum_{i} G^{0}_{\mathbf{k}\sigma}(i\omega_n) T^{(i)}_{\mathbf{k}\mathbf{k}'}(i\omega_n) G^{0}_{\mathbf{k}'\sigma}(i\omega_n) \\ &\quad + \sum_{\mathbf{k}'',i\neq j} G^{0}_{\mathbf{k}\sigma}(i\omega_n) T^{(i)}_{\mathbf{k}\mathbf{k}''}(i\omega_n) G^{0}_{\mathbf{k}''\sigma}(i\omega_n) T^{(j)}_{\mathbf{k}''\mathbf{k}'}(i\omega_n) G^{0}_{\mathbf{k}'\sigma}(i\omega_n) + \cdots \ , \\ T^{(i)}_{\mathbf{k}\mathbf{k}'}(i\omega_n) &= T_{\mathbf{k}\mathbf{k}'}(i\omega_n) e^{i(\mathbf{k}-\mathbf{k}')\cdot\mathbf{R}_i} \ . \end{aligned} \tag{D8}$$

Averaging over a randomly distributed impurity ensemble to restore momentum conservation and summing the resulting series gives

$$G^{-1}_{\mathbf{k}\sigma}(i\omega_n) = (G^{0}_{\mathbf{k}\sigma})^{-1}(i\omega_n) - \Sigma_{\text{band}}(i\omega_n) \ , \tag{D9}$$

where

$$\Sigma_{\text{band}}(i\omega_n) = \frac{2j+1}{2} C V^2 G_f(i\omega_n) \ ; \tag{D10}$$

here, $C=N_i/N$ is the dimensionless impurity concentration and V has a unit-cell normalization. Note that Σ_{band} is momentum independent. This follows from assuming a momentum-independent coupling to the impurities V. The imaginary part of the retarded self-energy $\Sigma_{\text{band}}(\omega+i0^{+})$ gives the energy broadening of conduction states. The corresponding decay rate is

$$\tau^{-1}(\omega) = -2\frac{2j+1}{2} C V^2 \, \mathrm{Im} G_f(\omega+i0^{+}) = NC\pi V^2 \rho_f(\omega) \ . \tag{D11}$$

This rate is strongly energy dependent; the rate peaks at small positive energies due to the Kondo resonance in the f density of states. It is intuitively clear that the band scattering rate and the impurity density of states are closely related: band electrons scatter by hopping into f orbitals. The scattering rate reflects the weight in these processes.

It may now be demonstrated that only Fig. 46(b) contributes to the conductivity in the dilute limit. Neglecting correlated multiple scattering corrections to $G_{\mathbf{k}\sigma}$, the simplest diagrams to be considered are those shown in Fig. 46(c). Here, Γ_1 is the single-site two-particle scattering vertex, whose form need not concern us here. Omitting explicit frequency dependences, the sum of these diagrams is

$$\begin{aligned} \Pi_1(i\nu_m) = \frac{2e^2}{3m^2}\frac{1}{\beta} \sum_{\text{frequency}} \sum_{\mathbf{k}} G_{\mathbf{k}} G_{\mathbf{k}} \Bigg[& \mathbf{k}^2 + \sum_{\mathbf{k}_1} (\mathbf{k}\cdot\mathbf{k}_1)\Gamma_1(\mathbf{k},\mathbf{k}_1) G_{\mathbf{k}_1} G_{\mathbf{k}_1} \\ & + \sum_{\mathbf{k}_1,\mathbf{k}_2} (\mathbf{k}\cdot\mathbf{k}_1)\Gamma_1(\mathbf{k},\mathbf{k}_2) G_{\mathbf{k}_2} G_{\mathbf{k}_2} \Gamma_1(\mathbf{k}_2,\mathbf{k}_1) G_{\mathbf{k}_1} G_{\mathbf{k}_1} + \cdots \Bigg] \ . \end{aligned} \tag{D12}$$

The factor of 2 arises from the spin sum. Each term in $\Gamma_1(\mathbf{k},\mathbf{k}_1)$ contains a $\hat{\mathbf{k}}$-dependent factor of the form

$$Y_{l,m_1-\sigma}(\hat{\mathbf{k}}) Y^{*}_{l,m_2-\sigma}(\hat{\mathbf{k}}) \ ;$$

hence, each diagram in $\Pi_1(i\nu_m)$ after the first is a linear combination of terms with $\hat{\mathbf{k}}$ dependence

$$\hat{\mathbf{k}} Y_{l,m_1-\sigma}(\hat{\mathbf{k}}) Y^{*}_{l,m_2-\sigma}(\hat{\mathbf{k}}) \ .$$

When $\hat{\mathbf{k}} \rightarrow -\hat{\mathbf{k}}$, this factor is converted to

$$(-1)^{2l+1} \hat{\mathbf{k}} Y_{l,m_1-\sigma}(\hat{\mathbf{k}}) Y^{*}_{l,m_2-\sigma}(\hat{\mathbf{k}}) \ ;$$

hence, these contributions to Π_1 $(i\nu_m)$ are odd in $\hat{\mathbf{k}}$ and sum (integrate) to zero.

Thus, in the extremely dilute limit,

$$\Pi_1(i\nu_m)=\frac{2e^2}{3m^2}\sum_{\mathbf{k}}\mathbf{k}^2\frac{1}{\beta}\sum_n G_{\mathbf{k}}(i(\omega_n+\nu_m))G_{\mathbf{k}}(i\omega_n) \; . \tag{D13}$$

This is a standard expression in transport theory.[77] Upon analytic continuation, one finds

$$\sigma(T)=-\lim_{\omega\to 0}\frac{\mathrm{Im}\Pi_1(\omega+i0^+)}{\omega}$$

$$=\frac{2e^2}{3m^2}\int\frac{d\mathbf{k}}{(2\pi)^3}\left[-\frac{\partial f}{\partial \varepsilon_k}\right]\mathbf{k}^2\tau(\varepsilon_k) \tag{D14}$$

with τ^{-1} the scattering rate in Eq. (D11).

Note that the lifetime appearing in the conductivity equation, i.e., the transport lifetime τ_{tr}, is just the single-particle lifetime τ. The transport and single-particle lifetimes differ in isotropic impurity scattering: in the isotropic limit, $\tau_{\mathrm{tr}}>\tau$, since small-angle scattering processes do not significantly reduce the conductivity. The lifetimes are the same in the present case since scattering occurs entirely in one orbital angular momentum channel. More generally, the lifetimes are identical if scattering occurs only in orbital channels $\{l_i\}$ with $|l_i-l_j|\geq 2$ for all i and j.

In the numerical evaluation of the resistivity, the following approximate form of Eq. (D14) has been applied:

$$\sigma(T)\simeq\frac{2e^2}{3m^2}k_F^2\int\frac{d\mathbf{k}}{(2\pi)^3}\left[-\frac{\partial f}{\partial \varepsilon_k}\right]\tau(\varepsilon_k)$$

$$=\frac{2e^2N(0)k_F^2}{3m^2}[(2j+1)C\pi V^2]^{-1}$$

$$\times\int_{-\infty}^{\infty}d\varepsilon\left[-\frac{\partial f}{\partial\varepsilon}\right][\rho_f(\varepsilon)]^{-1} \; ,$$

$$\rho(T)=\sigma^{-1}(T) \; . \tag{D15}$$

Additional transport properties such as the thermopower and thermal conductivity may be evaluated in similar fashion. The appropriate correlation functions in this case involve both the particle and energy currents. In an isotropic system, resistivity, thermopower and thermal conductivity may be jointly defined[78] in terms of

$$L_{m+n}=-\lim_{\omega\to 0}\left[\frac{1}{\omega}\mathrm{Im}\int_{-\infty}^{\infty}dt\,e^{i(\omega+i0^+)t}\Pi^{mn}(t)\right] \; ,$$

$$\Pi^{mn}(t)=-i\Theta(t)\langle[j_z^{(m)}(t),j_z^{(n)}(0)]\rangle \; , \tag{D16}$$

where

$$\mathbf{j}^{(n)}=\frac{1}{m}\sum_{\mathbf{k},\sigma}(\varepsilon_k-\mu)^n\mathbf{k}c_{\mathbf{k}\sigma}^{\dagger}c_{\mathbf{k}\sigma} \; . \tag{D17}$$

The defining relations for transport coefficients are

$$\rho(T)=\frac{1}{e^2L_0} \; ,$$

$$S(T)=-\frac{1}{eT}\frac{L_1}{L_0} \; , \tag{D18}$$

$$\kappa(T)=\frac{1}{T}\left[L_2-\frac{L_1^2}{L_0}\right] \; .$$

Again note the sign convention $e=|e|$.

The new correlation functions may be evaluated by the same method applied previously. The only difference is the presence of additional factors of the excitation energy $\varepsilon_k-\mu$ in momentum sums: thus,

$$L_n(T)=\frac{2}{3m^2}\int\frac{d\mathbf{k}}{(2\pi)^3}\left[-\frac{\partial f}{\partial \varepsilon_k}\right]\mathbf{k}^2(\varepsilon_k-\mu)^n\tau(\varepsilon_k)$$

$$\simeq\frac{2N(0)k_F^2}{3m^2}[(2j+1)C\pi V^2]^{-1}$$

$$\times\int_{-\infty}^{\infty}d\varepsilon\left[-\frac{\partial f}{\partial\varepsilon}\right]\varepsilon^n[\rho_f(\varepsilon)]^{-1} \; . \tag{D19}$$

In the preceding equation, a constant conduction band density of states near the Fermi surface is assumed.

APPENDIX E: ESTIMATES OF HIGHER-ORDER DIAGRAMS IN $\chi(T)$

In this appendix, we provide explicit estimates for contributions to the magnetic susceptibility beyond the leading term considered in Sec. V G. In general, $\chi(i\nu_m)$ may be divided into three parts:

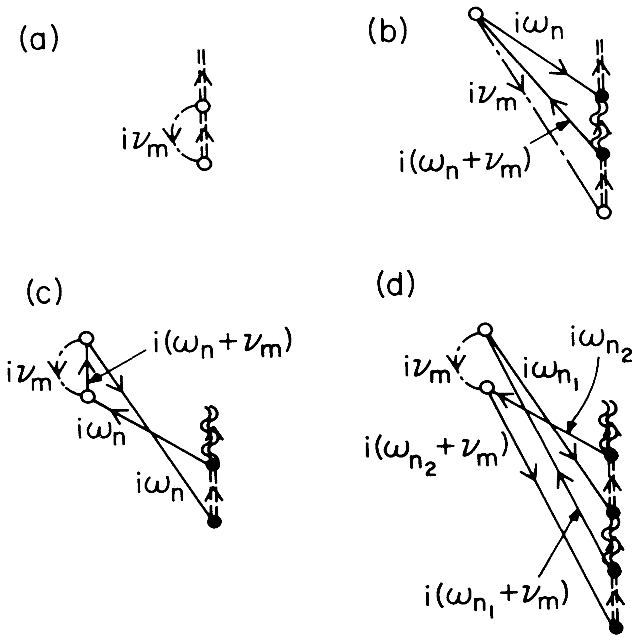

FIG. 47. Diagrammatic contributions to the magnetic susceptibility within the self-consistent approximation. (a) $\chi_{ff}(i\nu_m)$, the contribution from f moment correlations. This term, which is considered in detail in the text, dominates in the large-bandwidth limit. (b) $\chi_{cf}(i\nu_m)$, the contribution from conduction-moment–f-moment correlations. (c) One of the two diagrams in $\chi_{cc}^{(1)}(i\nu_m)$, the contribution from conduction-moment correlations involving a one-electron scattering vertex. (d) $\chi_{cc}^{(2)}(i\nu_m)$, the contribution from conduction moment correlations involving a two-electron scattering vertex.

$$\chi(i\nu_m)=\chi_{ff}(i\nu_m)+2\chi_{cf}(i\nu_m)+\chi_{cc}(i\nu_m)\ , \tag{E1}$$

where

$$\begin{aligned}\chi_{ff}(i\nu_m)&=\int_0^\beta d\tau\, e^{i\nu_m\tau}\langle\hat{M}(\tau)\hat{M}(0)\rangle\ ,\\ \chi_{cf}(i\nu_m)&=\int_0^\beta d\tau\, e^{i\nu_m\tau}\langle\hat{M}_c(\tau)\hat{M}(0)\rangle\ ,\\ \chi_{cc}(i\nu_m)&=\int_0^\beta d\tau\, e^{i\nu_m\tau}\langle\hat{M}_c(\tau)\hat{M}_c(0)\rangle\ ,\end{aligned} \tag{E2}$$

with

$$\begin{aligned}\hat{M}&=g\mu_B\sum_m mF_m^\dagger F_m \quad (f\ \text{moment})\ ,\\ \hat{M}_c&=g_c\mu_B\sum_{k,m} mc_{km}^\dagger c_{km} \quad (\text{conduction moment})\ .\end{aligned} \tag{E3}$$

For simplicity, we assume $g=g_c$.

Rules for evaluating $M_f(i\nu_m)=-\chi_{ff}(i\nu_m)$ have been summarized in Table VI. Rules for evaluating χ_{cf} are summarized in Table X. χ_{cc} may be further simplified: in general,

$$\chi_{cc}(i\nu_m)=\chi_{\text{Pauli}}\delta_{m0}+\chi_{cc}^{(1)}(i\nu_m)+\chi_{cc}^{(2)}(i\nu_m)\ , \tag{E4}$$

with

$$\chi_{\text{Pauli}}=(N\mu_j^2/3)N(0) \tag{E5}$$

the static susceptibility of the pure system; $\chi_{cc}^{(1)}$ a sum of contributions involving the vertex for scattering of a single conduction electron; and $\chi_{cc}^{(2)}$ a sum of terms involving the vertex for correlated scattering of two conduction electrons. Since the one-electron scattering vertex is just $T_1=V^2G_f$, with G_f the f-electron propagator, $\chi_{cc}^{(1)}$ takes a simple form. It may be demonstrated that

$$\chi_{cc}^{(1)}(i\nu_m)=-\frac{1}{\beta}\sum_{k,n}\frac{1}{i\omega_n-\varepsilon_k}\,\frac{1}{i(\omega_n+\nu_m)-\varepsilon_k}\left[\frac{1}{i\omega_n-\varepsilon_k}T_1(i\omega_n)+\frac{1}{i(\omega_n+\nu_m)-\varepsilon_k}T_1(i(\omega_n+\nu_m))\right]\ . \tag{E6}$$

Rules for evaluating $G_f(i\omega_n)$ have been summarized in Table IV. Rules for evaluating $\chi_{cc}^{(2)}$ are summarized in Table XI.

TABLE X. Diagrammatic rules for evaluating χ_{cf}. We list below rules for evaluating the conduction-moment–f-moment correlation function $\chi_{cf}(i\nu_m)$.

(a) Set down $2n+1$ vertices (solid dots) in a vertical line. Beginning at the bottom with a dashed line, connect the vertices with alternating dashed and wavy lines (all ascending), leaving the top vertex on a dashed line. (A total of $2n+1$ lines now appear.)

(b) To the left of the diagram and above all local lines, draw an isolated open circle (to represent the operator $mc_{km}^\dagger c_{km}$). Convert the bottom vertex to an open circle (to represent the operator $m'F_{m'}^\dagger F_{m'}$). Connect the two open circles with a dash-dotted "external line," carrying frequency $i\nu_m$ from top to bottom.

(c) Working to the left of the diagram, draw in two solid (conduction) lines connecting the isolated circle with vertices at odd and even positions. Assign to these lines Fermi frequencies, satisfying frequency conservation at the isolated circle.

(d) Working to the right of the diagram, connect the remaining $2n-2$ vertices with solid lines in all possible ways which maintain the direction of the dashed line at each vertex.

(e) Assign quantum numbers km (m) to solid lines (dashed lines), conserving angular momentum at each vertex.

(f) To lines on the right of the diagram, assign a factor $1-f_{km}$ (ascending) or f_{km} (descending), with f the Fermi function. To lines on the left of the diagram, assign conduction propagators $1/(i\omega_n-\varepsilon_k)$.

(g) Draw a perpendicular to each local configuration line, and assign to it an energy denominator $(z-E_\alpha)^{-1}$, where E_α is found by adding the energies (frequencies) of the ascending lines intersected by the perpendicular and subtracting the energies (frequencies) of descending lines intersected.

(h) Multiply the product of Fermi factors, propagators and energy denominators by $V^{2n}(g\mu_B)^2mm'$, where m and m' are the angular momenta attached to the open circles. Sum on conduction momenta and angular momenta. Sum on the free internal frequency with an associated factor of $1/\beta$. Multiply by $(-)^{c+d}$: c is the total number of conduction line crossings; d is the number (0 or 1) of descending lines which appear on the left of the diagram when the isolated open circle is rubbed out (merging two lines into one).

(i) Compute the contour integral

$$\frac{1}{Z_f}\int_\Gamma\frac{dz}{2\pi i}e^{-\beta z}R(z)\ ,$$

where R is the result of the preceding operations, Z_f is the system partition function, and Γ encircles all singularities of R in a counterclockwise fashion.

TABLE XI. Diagrammatic rules for evaluating $\chi_{cc}^{(2)}$. We list below rules for evaluating $\chi_{cc}^{(2)}(i\nu_m)$, the sum of contributions to the conduction-moment correlation function involving the vertex for two-electron scattering.

(a) Set down $2n$ vertices (solid dots) in a vertical line. Beginning at the bottom with a dashed line, connect the vertices with alternating dashed and wavy lines (all ascending), finally leaving the top vertex on a wavy line. (A total of $2n$ lines appear.)

(b) To the left of the diagram and above all local lines, draw two isolated open circles, one above the other. (These circles represent the operators $mc_{km}^{\dagger}c_{km}$ and $m'c_{km'}^{\dagger}c_{km'}$.) Connect the circles with a dash-dotted "external line," carrying frequency $i\nu_m$ from top to bottom.

(c) Working to the left of the diagram, draw in a solid line connecting the lower open circle with the bottom vertex. Draw in a second solid line connecting the lower circle with an arbitrary vertex at an even position (counting from the bottom). Draw in solid lines connecting the upper circle with two of the remaining vertices at odd and even positions. Assign to the four solid lines Fermi frequencies, satisfying frequency conservation at each open circle.

(d) Working to the right of the diagram, connect the remaining $2n-4$ vertices with solid lines in all possible ways which maintain the direction of the dashed line at each vertex.

(e) Assign quantum numbers km (m) to solid lines (dashed lines), conserving angular momentum at each vertex.

(f) To the lines on the right of the diagram, assign a factor $1-f_{km}$ (ascending) or f_{km} (descending), with f the Fermi function. To the lines on the left of the diagram, assign conduction propagators $1/(i\omega_n-\epsilon_k)$.

(g) Draw a perpendicular to each local configuration line, and assign to it an energy denominator $(z-E_\alpha)^{-1}$, where E_α is found by adding the energies (frequencies) of ascending lines intersected by the perpendicular and subtracting the energies of descending lines intersected.

(h) Multiply the product of Fermi factors, propagators and energy denominators by $V^{2n}(g\mu_B)^2mm'$, where m and m' are the angular momenta attached to the open circle. Sum on conduction momenta and angular momenta. Sum on the two internal frequencies with associated factors of $1/\beta$. Multiply by $(-1)^{c+d+1}$: c is the total number of conduction line crossings on left and right; d is the number (0, 1, or 2) of descending lines which appear on the left when the open circles are rubbed out (merging four lines into two).

(i) Compute the contour integral

$$\frac{1}{Z_f}\int_\Gamma \frac{dz}{2\pi i}e^{-\beta z}R(z),$$

where R is the result of the preceding operations, Z_f is the system partition function, and Γ encircles all singularities of R in a counterclockwise fashion.

Diagrammatic representations of χ_{ff}, χ_{cf}, $\chi_{cc}^{(1)}$, and $\chi_{cc}^{(2)}$ within the self-consistent approximation are shown in Fig. 47. The first contribution has been considered in the text. In the infinite bandwidth limit, the other contributions vanish. More generally, $\chi_{cc}^{(1)}$ is a modification of the normal Pauli susceptibility proportional to the impurity concentration; this term reflects the finite lifetime of conduction electrons near the Fermi surface. χ_{cf}, which measures the mutual correlation of conduction and f-electron moments, is of greater interest. We show below that it is of order $(\Gamma/D)\chi_{ff}$. Since $\chi_{cc}^{(2)}$ contains two of the f-electron insertions which appear in χ_{cf}, we conjecture, but do not prove, that it is of order $(\Gamma/D)^2\chi_{ff}$.

The expression for χ_{cf} which results from the diagrammatic rules in Table X is

$$\chi_{cf}=\frac{N\mu_j^2}{3}\frac{\Gamma}{\pi}\int_{-\infty}^{\infty}d\varepsilon\,\nu(\varepsilon)\frac{\partial}{\partial\varepsilon}\left[\frac{1}{\beta}\sum_n\frac{1}{i\omega_n-\varepsilon}\frac{1}{Z_f}\int_\Gamma\frac{dz}{2\pi i}e^{-\beta z}G_m^2(z)G_0(z-i\omega_n)\right]. \tag{E7}$$

Here, $\nu(\varepsilon)$ is the normalized density of conduction states, $N(\varepsilon)/N(0)$. After (a) integrating by parts on ε and (b) performing the contour integral, one finds

$$\chi_{cf}=\frac{N\mu_j^2}{3}\frac{\Gamma}{\pi}\int_{-\infty}^{\infty}d\varepsilon\left[-\frac{d\nu(\varepsilon)}{d\varepsilon}\right]F(\varepsilon), \tag{E8}$$

with

$$F(\varepsilon)=\frac{1}{Z_f}\int_{-\infty}^{\infty} d\omega\, e^{-\beta\omega}[2\,\mathrm{Re}G_m(\omega)\rho_m(\omega)S_1(\omega,\varepsilon)-\rho_0(\omega)S_2(\omega,\varepsilon)]\ ,$$
$$S_1(\omega,\varepsilon)=\frac{1}{\beta}\sum_n \frac{1}{i\omega_n-\varepsilon}G_0(\omega-i\omega_n)\ , \tag{E9}$$
$$S_2(\omega,\varepsilon)=\frac{1}{\beta}\sum_n \frac{1}{i\omega_n-\varepsilon}G_m^2(\omega+i\omega_n)\ .$$

Carrying out the Matsubara sums and cancelling terms where possible in $F(\varepsilon)$ gives

$$\chi_{cf}=\delta\chi_1+\delta\chi_2 \tag{E10}$$

with

$$\delta\chi_1=\frac{N\mu_j^2}{3}\frac{\Gamma}{\pi}\frac{1}{Z_f}\int_{-\infty}^{\infty} d\omega\, e^{-\beta\omega}\times 2\,\mathrm{Re}G_m(\omega)\rho_m(\omega)\int_{-\infty}^{\infty} d\varepsilon\, \nu'(\varepsilon)f(-\varepsilon)\mathrm{Re}G_0(\omega-\varepsilon) \tag{E11}$$

and

$$\delta\chi_2=\frac{N\mu_j^2}{3}\frac{\Gamma}{\pi}\frac{1}{Z_f}\int_{-\infty}^{\infty} d\omega\, e^{-\beta\omega}\rho_0(\omega)\int_{-\infty}^{\infty} d\varepsilon\, \nu'(\varepsilon)f(\varepsilon)\mathrm{Re}G_m^2(\omega+\varepsilon)\ . \tag{E12}$$

In order to proceed, approximate forms for the distribution functions are required. In the zero-temperature limit, we may write

$$\frac{1}{Z_f}e^{-\beta\omega}\times 2\,\mathrm{Re}G_m(\omega)\rho_m(\omega)\approx -\frac{2}{N}n_f\frac{1}{T_0}\delta(\omega-E_0)\ , \tag{E13}$$

$$\frac{1}{Z_f}e^{-\beta\omega}\rho_0(\omega)\approx(1-n_f)\delta(\omega-E_0)\ , \tag{E14}$$

$$\mathrm{Re}G_0(\omega)\approx(1-n_f)\mathrm{P}\left[\frac{1}{\omega-E_0}\right]+\frac{\omega-\delta\omega}{(\omega-\delta\omega)^2+(N\Gamma)^2}\ , \tag{E15}$$

and

$$\mathrm{Re}G_m^2(\omega)\approx\mathrm{Re}\frac{1}{(\omega-E_0-T_0+i\pi T_0/N)^2}\ . \tag{E16}$$

Here, P denotes a principal value, E_0 is the ground-state energy, and $\delta\omega$ is the hybridization-induced shift of the zero-frequency pole in G_0.

We assume a Lorentzian band profile with half-width D:

$$\nu(\varepsilon)=[1+(\varepsilon/D)]^{-2}\ . \tag{E17}$$

Inserting (E14) and (E16) into (E12) gives

$$\delta\chi_2\approx\frac{N\mu_j^2}{3}\frac{\Gamma}{\pi D^2}(1-n_f)\int_{-\infty}^{0} dy\frac{-2y}{(1+y^2)^2}\frac{1}{(y-T_0/D)^2}\approx\chi_{\mathrm{Pauli}}\frac{\Gamma}{D}(1-n_f)[2\ln(D/T_0)+O(1)]\ , \tag{E18}$$

where $\chi_{\mathrm{Pauli}}=(N\mu_j^2/3)(1/\pi D)$ is the susceptibility per electron in the pure system. This term is smaller than χ_{ff} by order $(T_0/D)^2\ln(D/T_0)$.

Inserting (E13) and (E15) into (E11) yields two terms, due to the two peak character of (E15). The term arising from the Kondo anomaly may be written as

$$\frac{N\mu_j^2}{3}\frac{\Gamma}{\pi D}\frac{2}{N}n_f\frac{1}{T_0}(1-n_f)\int_0^{\infty} dy\frac{-2y}{(1+y^2)^2}\frac{1}{y}=-\left[\frac{\pi}{N}\right]^2\chi_{\mathrm{Pauli}}\ . \tag{E19}$$

This term is smaller than χ_{ff} by order T_0/D.

The contribution to $\delta\chi_1$ from the broad resonance in G_0 near zero frequency may be estimated as

$$-\frac{N\mu_j^2}{3}\frac{1}{Z_f}\int_{-\infty}^{\infty} d\omega\, e^{-\beta\omega}\times 2\,\mathrm{Re}G_m(\omega)\rho_m(\omega)\left[-\frac{\Gamma}{\pi}\right]\int_0^{\infty} d\varepsilon\, \nu'(\varepsilon)\mathrm{Re}G_0(E_0-\varepsilon)$$
$$=\chi_{ff}\left[-\frac{\Gamma}{\pi}\right]\int_0^{\infty} d\varepsilon\, \nu'(\varepsilon)\mathrm{Re}G_0(E_0-\varepsilon)\approx\chi_{ff}\frac{\Gamma}{\pi D}\int_0^{\infty} dy\frac{-2y}{(1+y^2)^2}\frac{y-\bar{y}}{(y-\bar{y})^2+(N\Gamma/D)^2}\ , \tag{E20}$$

with $\bar{y}\equiv(E_0-\delta\omega)/D<0$. The dimensionless integral is of order unity: hence, $\delta\chi_1$ is smaller than χ_{ff} by order Γ/D.

[*] Present address: Institute for Theoretical Physics, University of California at Santa Barbara, Santa Barbara, CA 93106.

[†] Present address: Department of Physics, Ohio State University, 174 West 18th Avenue, Columbus, OH 43210-1106.

[1] For an overview of experiments on magnetic alloys, see the following review articles: M. D. Daybell, in *Magnetism*, edited by H. Suhl (Academic, New York, 1973), Vol. V, p. 121; A. Narath, *ibid.*, p. 149; C. Rizzuto, Rep. Prog. Phys. **37**, 147 (1974); G. Grüner, Adv. Phys. **23**, 941 (1974); M. B. Maple, L. E. Delong, and B. C. Sales, in *Handbook on the Physics and Chemistry of Rare Earths*, edited by K. A. Gschneider, Jr. and L. Eyring (North-Holland, Amsterdam, 1978), Vol. I, p. 797; F. Steglich, Z. Phys. B **23**, 331 (1976); A. M. Tsvelick and P. B. Wiegmann, Adv. Phys. **32**, 453 (1983).

[2] J. Kondo, Prog. Theor. Phys. **32**, 37 (1964).

[3] G. R. Stewart, Rev. Mod. Phys. **56**, 755 (1984).

[4] K. G. Wilson, Rev. Mod. Phys. **47**, 773 (1975).

[5] H. R. Krishna-murthy, J. W. Wilkins, and K. G. Wilson, Phys. Rev. Lett. **35**, 1101 (1975); Phys. Rev. B **21**, 1003 (1980); **21**, 1044 (1980).

[6] N. Andrei, K. Furuya, and J. H. Lowenstein, Rev. Mod. Phys. **55**, 331 (1983).

[7] A. M. Tsvelick and P. B. Wiegmann, Adv. Phys. **32**, 453 (1983).

[8] H. Keiter and J. C. Kimball, Int. J. Magn. **1**, 233 (1971); N. Grewe, Z. Phys. B **52**, 193 (1982); H. Keiter and G. Czycholl, J. Magn. Magn. Mater. **31**, 477 (1983); Y. Kuramoto, Z. Phys. B **53**, 37 (1983); P. Coleman, Phys. Rev. B **29**, 3035 (1984); F. C. Zhang and T. K. Lee, Phys. Rev. B **30**, 1556 (1984); N. E. Bickers, D. L. Cox, and J. W. Wilkins, Phys. Rev. Lett. **54**, 230 (1985).

[9] A number of alternative approaches to the large-degeneracy expansion have been investigated. A variational approach [see, e.g., O. Gunnarsson and K. Schönhammer, Phys. Rev. B **28**, 4315 (1983)] has been used to study static and dynamic properties at zero temperature. Functional integral techniques [N. Read and D. M. Newns, J. Phys. C **16**, 3273 (1982); A. Houghton, N. Read, and H. Won, Phys. Rev. B **35**, 5123 (1987); P. Coleman, *ibid.* **35**, 5072 (1987)] and direct diagrammatic perturbation theory [J. W. Rasul and A. C. Hewson, J. Phys. C **17**, 2555 (1984); **17**, 3332 (1984); N. E. Bickers (unpublished)] furnish information on low-temperature properties complementary to that obtained within the self-consistent expansion. For a more complete discussion of these approaches, see N. E. Bickers, Rev. Mod. Phys. (to be published).

[10] W. J. de Haas, J. de Boer, and G. J. van den Berg, Physica **1**, 609 (1933/34). See G. J. van den Berg, Prog. Low Temp. Phys. **4**, 194 (1967), for an extensive review of early experiments.

[11] P. W. Anderson, Phys. Rev. **124**, 41 (1961).

[12] J. R. Schrieffer and P. A. Wolff, Phys. Rev. **149**, 491 (1966).

[13] Several review articles document progress in magnetic alloy physics through the 1960s and early 1970s. See, e.g., G. Grüner and A. Zawadowski, Rep. Prog. Phys. **37**, 1497 (1974).

[14] H. Suhl, Phys. Rev. **138**, A515 (1965); H. Suhl and D. Wong, Physics **3**, 17 (1967).

[15] Y. Nagaoka, Phys. Rev. **138**, A1112 (1965).

[16] D. R. Hamann, Phys. Rev. **158**, 570 (1967); P. E. Bloomfield and D. R. Hamann, *ibid.* **164**, 856 (1967). See also the work of J. Zittartz and E. Müller-Hartmann, Z. Phys. **212**, 380 (1968).

[17] J. Zittartz and E. Müller-Hartmann, Z. Phys. **212**, 380 (1968).

[18] D. C. Mattis, Phys. Rev. Lett. **19**, 1478 (1967).

[19] W. Brenig and J. Zittartz, in *Magnetism*, Ref. 1, p. 185.

[20] K. Yosida and A. Yoshimori, in *Magnetism*, Ref. 1, p. 253.

[21] F. Takano and T. Ogawa, Prog. Theor. Phys. **35**, 343 (1966).

[22] G. Yuval and P. W. Anderson, Phys. Rev. B **1**, 1522 (1970); P. W. Anderson, G. Yuval and D. R. Hamann, *ibid.* **1**, 4464 (1970).

[23] J. W. Rasul and A. C. Hewson, J. Phys. C **17**, 2555 (1984).

[24] L. N. Oliveira and J. W. Wilkins, Phys. Rev. Lett. **47**, 1553 (1981).

[25] N. Andrei, Phys. Rev. Lett. **45**, 379 (1980).

[26] P. B. Wiegmann, Pis'ma Zh. Eksp. Teor. Fiz. **31**, 392 (1980) [JETP Lett. **31**, 364 (1980)].

[27] P. B. Wiegmann, Phys. Lett. **80A**, 163 (1980); P. B. Wiegmann, V. M. Filyov, and A. M. Tsvelick, Pis'ma Zh. Eksp. Teor. Fiz. **35**, 77 (1982) [JETP Lett. **35**, 92 (1982)]; P. B. Wiegmann and A. M. Tsvelick, *ibid.* **35**, 100 (1982) [*ibid.* **35**, 120 (1982)]; P. B. Wiegmann and A. M. Tsvelick, J. Phys. C **16**, 2281 (1983); A. M. Tsvelick and P. B. Wiegmann, *ibid.* **16**, 2321 (1983).

[28] E. Ogievetskii, A. M. Tsvelick, and P. B. Wiegmann, J. Phys. C **16**, L797 (1983).

[29] P. Schlottmann, Z. Phys. B **49**, 109 (1982); *ibid.* **51**, 49 (1983).

[30] V. T. Rajan, Phys. Rev. Lett. **51**, 308 (1983).

[31] P. Schlottmann, Z. Phys. B **54**, 207 (1984); **56**, 127 (1984); **57**, 23 (1984).

[32] A. Okiji and N. Kawakami, J. App. Phys. **55**, 1931 (1984).

[33] N. Kawakami and A. Okiji, Phys. Lett. **103A**, 205 (1984).

[34] N. Andrei, Phys. Lett. **87A**, 299 (1982).

[35] P. W. Anderson, in *Valence Fluctuations in Solids*, edited by L. M. Falicov, W. Hanke, and M. B. Maple (North-Holland, Amsterdam, 1981), p. 451.

[36] T. V. Ramakrishnan, in *Valence Fluctuations in Solids*, Ref. 35, p. 13; T. V. Ramakrishnan and K. Sur, Phys. Rev. B **26**, 1798 (1982).

[37] S. Ma, Phys. Rev. A **7**, 2172 (1973); R. Oppermann and F. J. Wegner, Z. Phys. B **34**, 327 (1979); M. Ma and E. Fradkin, Phys. Rev. B **28**, 2990 (1983).

[38] P. Coleman, Phys. Rev. B **29**, 3035 (1984).

[39] Y. Kuramoto, Z. Phys. B **53**, 37 (1983).

[40] G. Baym, Phys. Rev. **127**, 1391 (1962).

[41] One of the earliest papers to emphasize the importance of the Kondo resonance is N. Rivier, V. Zlatic, and G. Grüner, Solid State Commun. **14**, 639 (1974).

[42] See, e.g., P. Nozières, *Theory of Interacting Fermi Systems* (Benjamin, New York, 1964).

[43] See, e.g., the discussion in G. D. Mahan, *Many-Particle Physics* (Plenum, New York, 1981), Chap. 4.

[44] F. C. Zhang and T. K. Lee, Phys. Rev. B **30**, 1556 (1984).

[45] H. Keiter and G. Morandi, Phys. Rep. **109**, 227 (1984).

[46] A. A. Abrikosov, Physics **2**, 5 (1965).

[47] S. E. Barnes, J. Phys. F **6**, 1375 (1976).

[48] The convention for spherical harmonics and Clebsch-Gordon coefficients is that of A. Messiah, *Quantum Mechanics* (North-Holland, Amsterdam, 1961).

[49] H. Kojima, Y. Kuramoto, and M. Tachiki, Z. Phys. B **54**, 293 (1984).

[50] Y. Kuramoto and H. Kojima, Z. Phys. B **57**, 95 (1984).

[51] D. C. Langreth, Phys. Rev. **150**, 516 (1966).

[52] K. Yamada, Prog. Theor. Phys. **53**, 970 (1975); K. Yosida and K. Yamada, *ibid.* **53**, 1286 (1975); A. Yoshimori, *ibid.* **55**, 67 (1976).

[53] E. Müller-Hartmann, Z. Phys. B **57**, 281 (1984).

[54] D. M. Wieliczka, C. G. Olsen, and D. W. Lynch, Phys. Rev.

B **29**, 3028 (1984).

[55] N. E. Bickers, D. L. Cox, and J. W. Wilkins, Phys. Rev. Lett. **54**, 230 (1985); D. L. Cox, N. E. Bickers, and J. W. Wilkins, J. App. Phys. **57**, 3166 (1985); J. Magn. Magn. Mater. **54-57**, 333 (1986).

[56] N. W. Ashcroft and N. D. Mermin, *Solid State Physics* (Saunders College, Philadelphia, 1976).

[57] H. Shiba, Prog. Theor. Phys. **54**, 967 (1975).

[58] K. Winzer, Solid State Commun. **16**, 521 (1975).

[59] W. Felsch, Z. Phys. B **29**, 211 (1978).

[60] H. J. Ernst, H. Grühl, T. Krug, and K. Winzer, in *Proceedings of the 17th International Conference on Low Temperature Physics*, edited by U. Eckern *et al.* (North-Holland, Amsterdam, 1984), p. 137.

[61] H. Smith and J. W. Wilkins, Phys. Rev. Lett. **24**, 489 (1970).

[62] E. Zirngiebl, B. Hillebrands, S. Blümenroder, G. Güntherodt, K. Winzer, and Z. Fisk, Phys. Rev. B **30**, 4052 (1984).

[63] D. K. C. McDonald, *Thermoelectricity* (Wiley, New York, 1962).

[64] N. Sato, S. Kunii, I. Oguro, T. Komatsubara, and T. Kasuya, J. Magn. Magn. Mater. **47-48**, 86 (1985). See also Ref. 62.

[65] H.-U. Desgranges and J. W. Rasul (private communication).

[66] O. Gunnarsson and K. Schönhammer, Phys. Rev. Lett. **50**, 604 (1983); Phys. Rev. B **28**, 4315 (1983).

[67] R. M. Galera, D. Givord, J. Pierre, A. P. Murani, C. Vettier, and K. R. A. Ziebeck, J. Magn. Magn. Mater. **47-48**, 139 (1985).

[68] E. Holland-Moritz, D. Wohlleben, and M. Loewenhaupt, Phys. Rev. B **25**, 7482 (1982).

[69] A. Qachaou, E. Beaurepaire, M. Benakki, B. Lemius, J. P. Kappler, A. J. P. Meyer, and P. Panissod, J. Magn. Magn. Mater. **63-64**, 635 (1987).

[70] The self-consistent approach remains surprisingly accurate for $N=2$: see, e.g., F. C. Zhang and T. K. Lee, Phys. Rev. B **30**, 1556 (1984). Recent studies [D. L. Cox (unpublished)] indicate the technique's reliability extends to temperatures as low as $0.1T_0$ in this case.

[71] In this regard, note the recent work of N. Read, K. Dharamvir, J. W. Rasul, and D. M. Newns, J. Phys. C **19**, 1597 (1986) (thulium), and A. C. Nunes, J. W. Rasul and G. A. Gehring, *ibid.* **19**, 1017 (1986) (uranium).

[72] H. Keiter, Z. Phys. B **60**, 337 (1985).

[73] *Handbook of Mathematical Functions,* edited by A. M. Abramowitz and I. A. Stegun (Dover, New York, 1972), pp. 258 and 259.

[74] D. L. Cox (unpublished).

[75] S. Inagaki, Prog. Theor. Phys. **62**, 1441 (1979).

[76] See, e.g., G. D. Mahan, *Many-Particle Physics* (Plenum, New York, 1981).

[77] G. D. Mahan, *Many-Particle Physics,* Ref. 76, p. 600.

[78] G. D. Mahan, *Many-Particle Physics,* Ref. 76, p. 218.